Study on Electron-rich Polycyclic Systems Containing a Quinodimethane Skeleton with Two Oxygen Bridges

(二つの酸素架橋構造を有する電子豊富
含キノジメタン縮合多環系に関する研究)

理学研究科
物質分子系専攻

平成 28 年度

佐　藤　千　尋
（Chihiro Sato）

Contents

Chapter 4: Synthesis and properties of functionalized 5,8-dioxapentaphene systems

Chapter 1
General introduction

1-1. Introduction

Nowadays, synthesis of new π-conjugated systems with unique physical and chemical properties closely relates to the development of next-generation materials in the fields of organic electronics,[1] photonics,[2] spintronics,[3] secondary batteries,[4] and molecular devices.[5] In particular, organic semiconducting materials for field-effect transistors, light-emitting diodes, and solar cells have received much attention and progressed rapidly over the last decade because of their many advantages, such as diversity of molecular designs, various synthetic approaches, structural flexibility, and good processability for device fabrication.[6] Quinoidal compounds can be taken as an example of the attractive building blocks in materials science.[7] Benzoquinone, one of simple quinoidal compounds with two exocyclic carbonyl groups, has a low LUMO energy level and a high electron affinity due to the presence of electronegative oxygen atoms. In fact, ubiquinone, a benzoquinone derivative, is an important electron carrier in metabolic processes in biological systems (Scheme 1-1).[8] Moreover, benzoquinone derivatives, e.g., 2,3-dichloro-5,6-dicyano-1,4-benzoquinone (DDQ) and chloranil (Figure 1-1), have been widely used as organic oxidants in organic chemistry.[9] In the field of materials science, electronegative quinoidal compounds, such as 7,7,8,8-tetracyano-*p*-quinodimethane (TCNQ), *N*,*N*'-dicyano-*p*-benzoquinone diimine (DCNQI), DDQ, and chloranil, have been extensively studied as superior electron acceptors, which form organic charge-transfer (CT) complexes with electron donors such as tetrathiafulvalene (TTF). Some CT complexes have good electrical conductivity;[10] moreover, Kobayashi et al. reported that the CT complex of chloranil with TTF exhibits ferroelectric behavior.[11]

Scheme 1-1. Redox process of ubiquinone.

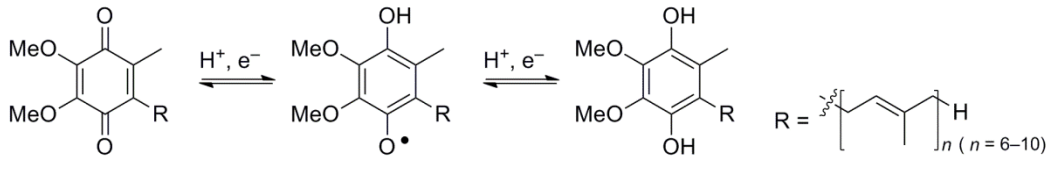

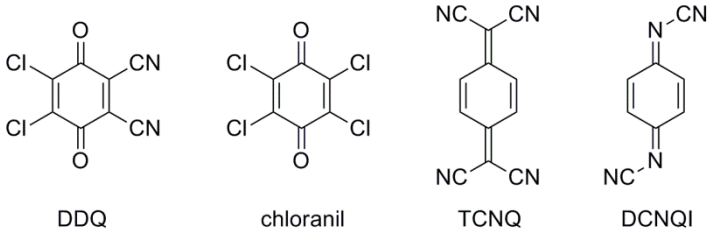

Figure 1-1. Typical organic oxidants and electron acceptors.

Here, we think back the unique characteristics of quinoidal molecules.[12] Drawing a quinoidal structure as a typical closed-shell form (**Kekulé form** shown in Figure 1-2a, c), in which the framework can be regarded as a simple cross-conjugation system with two exocyclic double bonds, the electronic structure possesses a closed-shell "non-aromatic" nature. On the other hand, considering the resonance structure containing an "aromatic" ring, the central cyclic π-system can benefit from the aromatic stabilization energy, whereas two "unpaired" electrons are generated at the two exocyclic atoms X (X = O, NR, or CR_2); that is an open-shell singlet **biradical form** (Figure 1-2b, d). Actually, according to both experimental[13] and theoretical[14] studies, the electronic structure of quinoidal compounds has been understood as a resonance hybrid of Kekulé and biradical forms. This resonance in quinoidal compounds leads to a smaller HOMO–LUMO gap compared to that of similar benzenoid compounds, resulting in visible and/or near-infrared (NIR) absorption.[15] In addition, quinoidal compounds can form the corresponding aromatically stabilized mono- or di-cationic/anionic species by one- or two-electron oxidation or reduction processes (Scheme 1-2). Thus, they have intrinsic reversible redox abilities.[16]

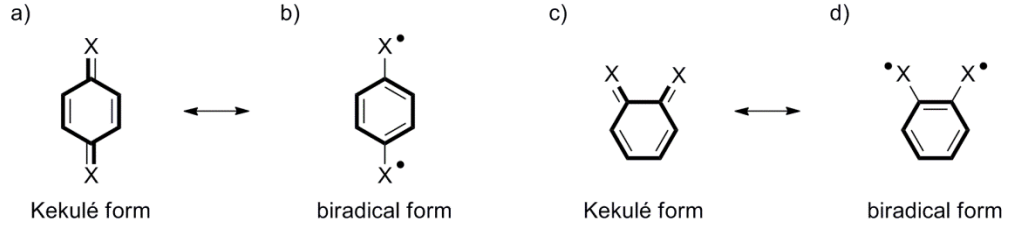

Figure 1-2. Resonance hybrid of Kekulé and biradical forms for (a) (b) *p*-quinoidal and (c) (d) *o*-quinoidal systems (X = O, NR, CR_2).

Scheme 1-2. Redox processes of (a) *p*-quinoidal and (b) *o*-quinoidal systems (X = O, NR, CR_2).

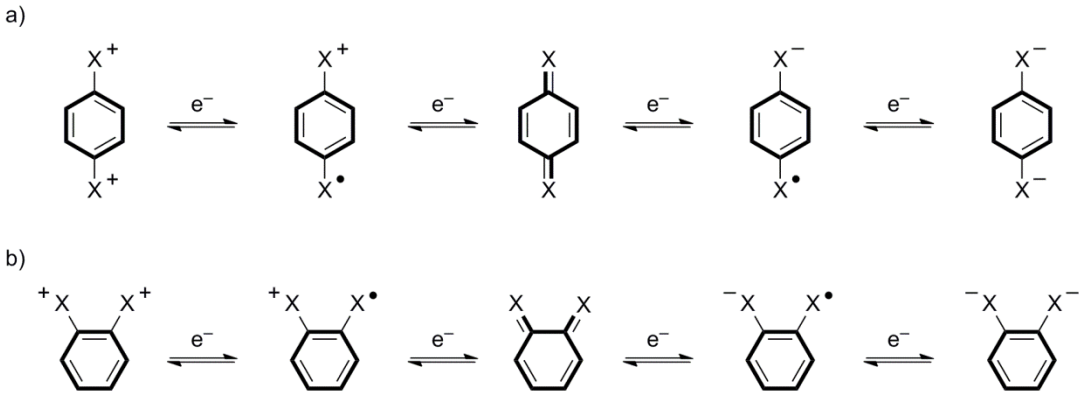

p-Quinodimethane (*p*QDM) is one of simple quinoidal hydrocarbons. Because of the lack of oxygen atoms, *p*QDM derivatives have a higher HOMO energy than benzoquinones, and a high reactivity derived from the biradical character.[17] The generation of unsubstituted *p*QDM (**1**) was first described by Szwarc in 1947 as a product of the pyrolysis of *p*-xylene.[18] However, in the condensed phase, **1** reacted with itself to give poly(phenylene ethylene) (**I**) and [2,2]para-cyclophane (**II**) (Scheme 1-3).[19] The π-extended *p*QDM derivatives Thiele's hydrocarbon (**2**)[20] and Chichibabin's hydrocarbon (**3**)[21] (Figure 1-3) were synthesized in 1904 and 1907, respectively, and their detailed structures were investigated by the X-ray structural analysis by Montgomery et al. in 1968.[22] The crystal structure of **2** clearly shows bond-length alternations around the *p*QDM skeleton, indicating the closed-shell electronic structure. However, the length of the exocyclic double bond (1.381(3) Å) is slightly longer than that typical of olefins (1.33–1.34 Å). On the other hand, the crystal structure of **3** exhibits drastically decreased bond-length alternations, with lengths of 1.448(4) and 1.415(3) Å for the exocyclic bonds, and 1.420(3), 1.372(3), and 1.429(3) Å for the rings. These values are close to that of aromatic C–C bonds (1.397 Å of benzene), indicating a significant contribution of the biradical structure in **3**. In fact, in the solid state, **3** shows green color whereas **2** is orange-yellow. At the same time, the cyclic voltammograms of both compounds exhibit two reversible oxidation and two reversible reduction waves (**2**: E^{ox2} = +1.05 V, E^{ox1} = +0.85 V, E^{red1} = –1.45 V, E^{red2} = –1.75 V, and **3**: E^{ox2} = +0.69 V, E^{ox1} = +0.47 V, E^{red1} = –1.05 V, E^{red2} = –1.39 V vs Ag/AgCl in benzonitrile).[23] In recent years, the biradical character has been reported to influence on nonlinear optics[24] and singlet fission.[25] Thus, quinoidal π-conjugated systems with high biradical character have been intensively investigated.[26]

Scheme 1-3. Generation of *p*QDM (**1**) and its following reactions.

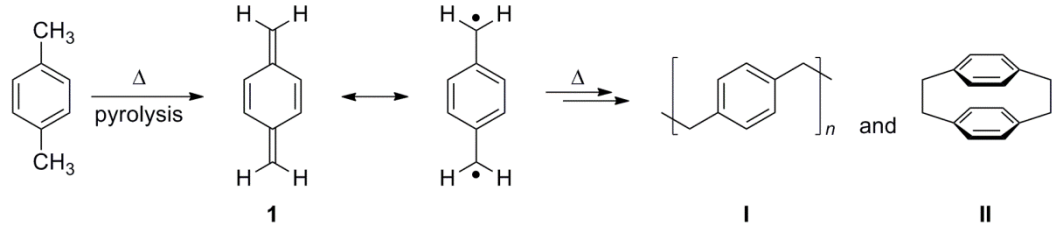

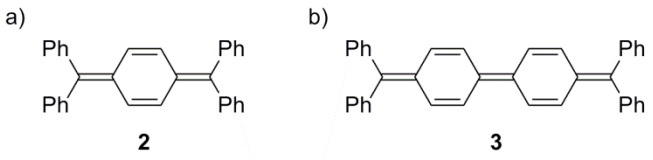

Figure 1-3. Structures of (a) Thiele's hydrocarbon (**2**) and (b) Chichibabin's hydrocarbon (**3**).

In contrast to *p*QDMs, *o*-quinodimethane (*o*QDM) derivatives are well-known versatile reagents in synthetic chemistry due to their high reactivity.[27] In 1957, Cava et al. first suggested the formation of 7,8-dibromo-*o*QDM (**4**) as an intermediate of the dehalogenation reaction of 7,7,8,8-tetrabromo-*o*-xylene with NaI to produce *trans*-1,2-dibromobenzocyclobutene (**III**) (Scheme 1-4).[28] In 1968, Quinkert et al. reported the preparation of 7,7,8,8-tetraphenyl-*o*QDM (**5**) by the UV-irradiation of 1,1,2,2-tetraphenylbenzocyclobutene (**IV**) (Scheme 1-5).[29] According to this report, **5** shows a wide absorption band in the visible region (λ_{max} = 520 nm, $\lambda_{edge} \approx$ 620 nm in isopentane–methylcyclohexane (4:1 v/v) at –185 °C) but spontaneously isomerized into its precursor (**IV**) and 4a,10-dihydro-9,10,10-triphenylanthracene (**V**) by intramolecular cyclization. In 1988, Roth et al. prepared unsubstituted *o*QDM (**6**) in gas phase by thermal ring-opening of benzocyclobutene (**VI**) (Scheme 1-6), and estimated the thermal activation parameters (ΔH = –11.1 kcal mol^{-1} for the reaction **6**→**VI**).[30]

These results indicate that the synthesis of stable *o*QDM derivatives is still challenging. Only four highly stable *o*QDM derivatives (**7**–**10**)[31–34] (Figure 1-4) had been reported prior to this study. As suggested by the chemical structure of these compounds, there are two approaches to suppress the inter- and intramolecular isomerization of *o*QDM: "annulation" (as in **8**[32] and **9**[33]) and "anchoring" (as in **7**[31] and **10**[34]). In the former case, according to Clar's sextet rule,[35] the phenanthrene- or benzodithiophene-type frameworks generate a local aromaticity in the outer rings. This method, however, reduced not only the aromatic stabilization derived from the formation of the corresponding biradical or benzocyclobutene but also their quinoidal characteristics. In the second approach, the exocyclic carbon atoms are anchored to the six-membered ring of the *o*QDM unit through peripheral benzene rings or quinoidal thiophene frameworks to inhibit the corresponding isomerization. These *o*QDM derivatives show a wide absorption band up to ~800 nm, indicating that the quinoidal characteristic was preserved. In addition, **7** and **8** are able to form conductive CT complexes, suggesting that *o*QDM derivatives are promising functional organic materials.

Scheme 1-4. Generation of 7,8-dibromo-*o*QDM (**4**) and its following reaction.

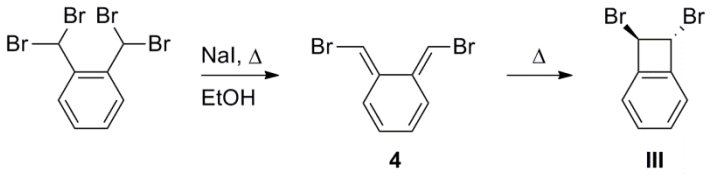

Scheme 1-5. Synthesis of 7,7,8,8-tetraphenyl-*o*QDM (**5**) and its following reactions.

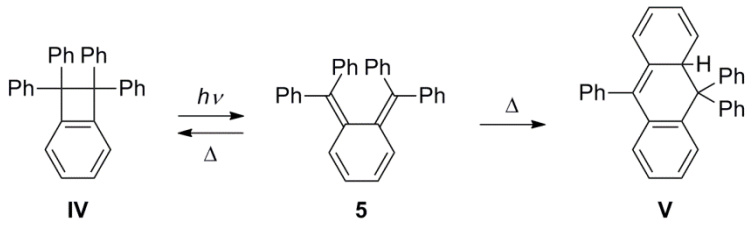

Scheme 1-6. Thermal ring-opening and -closing reactions between *o*QDM (**6**) and benzocyclobutene (**VI**).

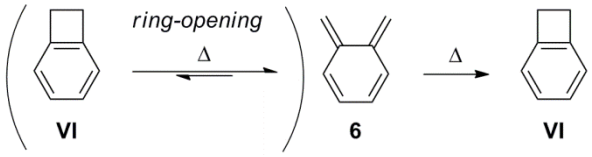

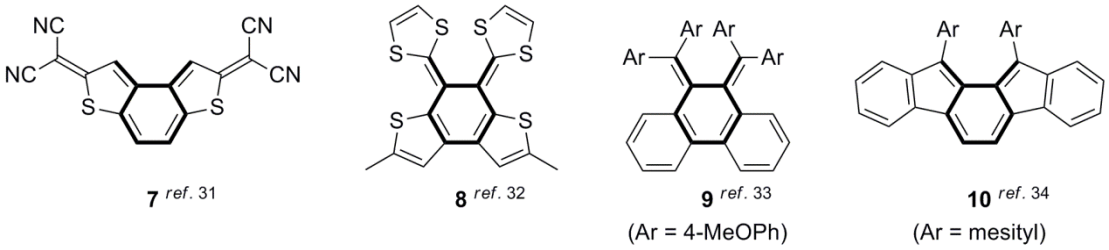

7 *ref*. 31 **8** *ref*. 32 **9** *ref*. 33 (Ar = 4-MeOPh) **10** *ref*. 34 (Ar = mesityl)

Figure 1-4. Stable *o*QDM derivatives.

The purpose of this thesis is to develop new electron-rich quinoidal compounds with obvious *o*QDM character and investigate their detailed properties to develop a novel platform for organic materials design. The author has designed 5,8-dioxapentaphene (DOP) as a key framework containing the *o*QDM skeleton and synthesized various DOP derivatives (**11**, **13**–**18**) (Figure 1-5). All compounds showed broad absorption bands up to the NIR region and excellent electron-donating abilities.

This thesis contains the following three chapters: (i) **Chapter 2**: "Synthesis and properties of 2,11-dibromo-13,14-dimesityl-5,8-dioxapentaphene and its radical cation", which describes the synthesis and fundamental properties of **11** and the isolation of the *o*QDM-based radical cation salt $\mathbf{11}^{\bullet+}\bullet SbF_6^-$; (ii) **Chapter 3**: "Experimental investigation of the properties arising from the *o*- and *p*-quinodimethane skeletons", in which the structural and electronic properties of **11** and **12** were compared to elucidate the properties deriving from the *o*QDM and *p*QDM skeletons; and (iii) **Chapter 4**: "Synthesis and properties of functionalized 5,8-dioxapentaphene systems", which describes the synthesis and properties of DOP derivatives (**13**–**18**) for application in the development of new materials with electronic and chiroptical properties deriving from the *o*QDM character.

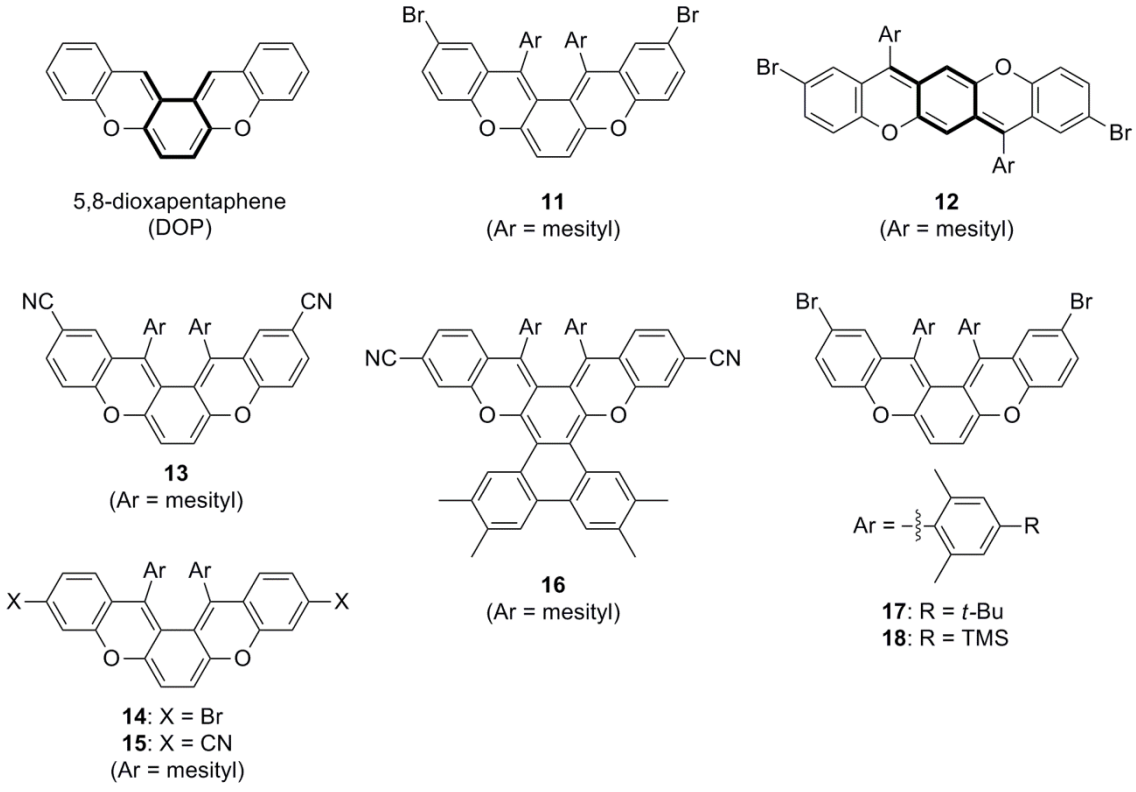

Figure 1-5. Chemical structures described in this thesis.

1-2. References

(1) (a) Brütting, W.; Adachi, C. *Physics of Organic Semiconductors*, 2nd ed.; Wiley−VCH: Weinheim, 2012.

(b) Köhler, A.; Bässler, H. *Electronic Processes in Organic Semiconductors: An Introduction*; Wiley−VCH: Weinheim, 2015.

(c) Zhan, C.; Yao. J. *Chem. Mater.* **2016**, *27*, 1948−1964.

(2) (a) Samuel, I. D. W.; Turnbull G. A. *Chem. Rev.* **2007**, *107*, 1272−1295.

(b) Jansen-van Vuuren, R. D. ; Armin, A.; Pandey, A. K.; Burn, P. L.; Meredith, P. *Adv. Mater.* **2016**, *28*, 4766−4802.

(3) (a) Itoh, K.; Kinoshita, M. *Molecular Magnetism*; Kodansha & Gordon and Breach: Tokyo, 2000.

(b) Devkota, J.; Geng, R.; Subedi, R. C.; Nguyen, T. D. *Adv. Funct. Mater.* **2016**, *26*, 3881−3898.

(4) (a) Morita, Y.; Nishida, S.; Murata, T.; Moriguchi, M.; Ueda, A.; Satoh, M.; Arifuku, K.; Sato, K.; Takui, T. *Nat. Mater.* **2011**, *10*, 947−951.

(b) Schon, T. B.; McAllister, B. T.; Lia, P. -F.; Seferos, D. S. *Chem. Soc. Rev.* **2016**, *45*, 6345−6404.

(c) Muench, S.; Wild, A.; Friebe, C.; Häupler, B.; Janoschka, T.; Schubert, U. S. *Chem. Rev.* **2016**, *116*, 9438−9484.

(d) Winsberg, J.; Hagemann, T.; Janoschka, T.; Hager, M. D.; Schubert, U. S. *Angew. Chem., Int. Ed.* **2016**, *55*, in press (DOI: 10.1002/anie.201604925).

(5) (a) Balzani, V.; Credi, A.; Venturi, M. *Molecular Devices and Machines: Concepts and Perspectives for the Nanoworld*, 2nd ed.; Wile−VCH: Weinheim, 2008.

(b) Feringa, B. L.; Browne, W. R. *Molecular Switches*, 2nd ed.; Wile−VCH: Weinheim, 2011.

(6) (a) Parker, T. C.; Maerder, S. R. *Synthetic Methods in Organic Electronic and Photonic Materials: A Practical Guide*; The Royal Society of Chemistry: Cambridge, 2015.

(b) Qian, Y.; Zhang, W.; Xie, L.; Qi, D.; Chandran, B. K.; Chen. X.; Huang, W. *Adv. Mater.* **2016**, *28*, 9243−9265.

(c) Baeg, K. -J.; Caironi, M.; Noh, Y. -Y. *Adv. Mater.* **2013**, *25*, 4210−4244.

(d) Kang, H.; Kim, G.; Kim, J.; Kwon, S.; Kim, H.; Lee, K. *Adv. Mater.* **2016**, *28*, 7821−7861.

(7) (a) Kikuchi, A.; Iwahori, F.; Abe, J. *J. Am. Chem. Soc.* **2004**, *126*, 6526−6527.

(b) Tonzola, C. J.; Hancock, J. M.; Babel, A.; Jenekhe, S. A. *Chem. Commun.* **2005**, 5214−5216.

(c) Zhu, X.; Tsuji, H.; Nakabayashi, K.; Ohkoshi, S.; Nakamura, E. *J. Am. Chem. Soc.* **2011**, *133*, 16342−16345.

(d) Chase, D. T.; Fix, A. G.; Kang, S. J.; Rose, B. D.; Weber, C. D.; Zhong, Y.; Zakharov, L. N.; Lonergan, M. C.; Nuckolls, C.; Haley, M. M. *J. Am. Chem. Soc.* **2012**, *134*, 10349−10352.

(e) Nishida, J.; Tsukaguchi, S.; Yamashita, Y. *Chem. - Eur. J.* **2012**, *18*, 8964−8970.

(f) Mori, T.; Yanai, N.; Osaka, I.; Takimiya, K. *Org. Lett.* **2014**, *16*, 1334−1337.

(8) Turrens, J. F.; Alexandre, A.; Lehninger, A. L. *Arch. Biochem. Biophys.* **1987**, *237*, 408−414.

(9) Connelly, N. G.; Geiger, W. E. *Chem. Rev.* **1996**, *96*, 877−910.

(10) (a) Martin, N.; Segura, J. L.; Seoane, C. *J. Mater. Chem.* **1997**, *7*, 1661−1676.

(b) Hünig, S.; Herberth, E. *Chem. Rev.* **2004**, *104*, 5535−5563.

(c) Saito, G.; Yoshida, Y. *Bull. Chem. Soc. Jpn.* **2007**, *80*, 1−137.

(11) Kobayashi, K.; Horiuchi, S.; Kumai, R; Kagawa, F.; Murakami, Y.; Tokura, Y. *Phys. Rev. Lett*. **2012**, *108*, 237601.

(12) (a) Patai, S. *The Chemistry of the Quinonoid Compounds*; Wiley: Chichester, 1974.

(b) Patai, S.; Rappoport, Z. *The Chemistry of the Quinonoid Compounds*; Wiley: Chichester, 1988; Vol. 2.

(13) (a) Kamada, K.; Ohta, K.; Kubo, T.; Shimizu, A.; Morita, Y.; Nakasuji, K.; Kishi, R.; Ohta, S.; Furukawa, S.; Takahashi, H.; Nakano, M. *Angew. Chem., Int. Ed.* **2007**, *46*, 3544−3546.

(b) Kamada, K.; Ohta, K.; Shimizu, A.; Kubo, T.; Kishi, R.; Takahashi, T.; Botek, E.; Champagne, B.; Nakano, M. *J. Phys. Chem. Lett.* **2010**, *1*, 937−940.

(14) (a) Doehnert, D.; Koutecky, J. *J. Am. Chem. Soc.* **1980**, *102*, 1789−1796.

(b) Karafiloglou, P. *J. Chem. Educ.* **1989**, *66*, 816−818.

(15) (a) Cava, M. P.; Schlessinger, R. H. *J. Am. Chem. Soc.* **1963**, *85*, 835−836.

(b) Nishida, J.; Fujiwara, Y.; Yamashita, Y. *Org. Lett.* **2009**, *11*, 1813−1816.

(c) Sun, Z.; Ye, Q.; Chi, C.; Wu, J. *Chem. Soc. Rev.* **2012**, *41*, 7857−7889.

(d) Simizu, A.; Kishi, R.; Nakano, M.; Shimoi, D.; Sato, K.; Takui, T.; Hisaki, I.; Miyata, M.; Tobe, Y. *Angew. Chem., Int. Ed.* **2013**, *52*, 6076−6079.

(16) (a) Simizu, A.; Uruichi, M.; Yakushi, K.; Matsuzaki, H.; Okamoto, H.; Nakano, M.; Hirano, Y.; Matsumoto, K.; Kurata, H.; Kubo, T. *Angew. Chem., Int. Ed.* **2009**, *48*, 5482−5486.

(b) Fix, A. G.; Deal, P. K.; Vonnegut, C. L.; Rose, V. D.; Zakharov, L. N.; Haley, M. M. *Org. Lett.* **2013**, *15*, 1362−1365.

(c) Rudebusc, G. E.; Espejo, G. L.; Zafra, J. L.; Peña-Alvarez, N.; Spisak, S. N.; Fukuda, K.; Wei, Z.; Nakano, M.; Petrukhina, M. A.; Casado, J.; Haley, M. M. *J. Am. Chem. Soc.* **2016**, *138*, 12648−12654.

(17) (a) Szwarc, M. *Discuss. Faraday Soc.* **1947**, *2*, 46−49.

(b) Coulson, C. A.; Craig, D. P.; Maccoll, A.; Pullman, M. A. *Discuss. Faraday Soc.* **1947**, *2*, 36−38.

(c) Szunerits, S.; Utley, J. H. P.; Nielsen, M. F. *J. Chem. Soc., Perkin Trans. 2* **2000**, 669−675.

(18) Szwarc, M. *Nature* **1947**, *160*, 403.

(19) Brown, C. J.; Farthing, A. C. *Nature* **1949**, *164*, 915−916.

(20) Thiele, J.; Balhorn, H. *Ber. Dtsch. Chem. Ges.* **1904**, *37*, 1463−1470.

(21) Tschitschibabin, A. E. *Ber. Dtsch. Chem. Ges.* **1907**, *40*, 1810−1819.

(22) Montgomery, L. K.; Huffman, J. C.; Jurczak, E. A.; Grendze, M. P. *J. Am. Chem. Soc.* **1986**, *108*, 6004−6011.

(23) Kothe, G.; Sümmermann, W.; Baumgärtel, H.; Zimmermann, H. *Tetrahedron* **1972**, *28*, 5949−5955.

(24) (a) Kishi, R.;Nakano, M.; Ohta, S.; Takebe, A.; Nate, M.; Takahashi, H.; Kubo, T.; Kamada, K.; Ohta, K.; Champagne, B.; Botek, E. *J. Chem. Theory Comput.* **2007**, *3*, 1699−1707.

(b) Nakano, M.; Kishi, R.; Nitta, T.; Kubo, T.; Nakasuji, K.; Kamad, K.; Ohta, K.; Champagne, B.; Botek, E.; Yamaguchi, K. *J. Phys. Chem. A* **2005**, *109*, 885−891.

(c) Takauji, K.; Suizu, R.; Awaga, K.; Kishida, H.; Nakamura, A. *J. Phys. Chem. C* **2014**, *118*, 4303−4308.

(25) (a) Smith, M. B.; Michl, J. *Chem. Rev.* **2010**, *110*, 6891−6936.

(b) Ito, S.; Minami, T.; Nakano, M. *J. Phys. Chem. C* **2012**, *116*, 19729−19736.

(c) Minami, T.; Nakano, M. *J. Phys. Chem. Lett.* **2012**, *3*, 145−150.

(d) Minami, T.; Ito, S.; Nakano, M. *J. Phys. Chem. Lett.* **2013**, *4*, 2133−2137.

(26) (a) Abe, M. *Chem. Rev*. **2013**, *113*, 7011−7088.

(b) Zeng, Z.; Shi, X.; Chi, C.; Navarrete, J. T. L.; Casado, J.; Wu, J. *Chem. Soc. Rev.* **2015**, *44*, 6578–6596.

(c) Kubo, T. *Chem. Lett.* **2015**, *44*, 111−122.

(d) Rudebusch, G. E.; Zafra, J. L.; Jorner, K.; Fukuda, K.; Marshall, J. L.; Arrechea-Marcos, I.; Espejo, G. L.; Ortiz, R. P.; Gómez-García, C. J.; Zakharov, L. N.; Nakano, M.; Ottosson, H.; Casado, J.; Haley, M. M. *Nat. Chem.* **2016**, *8*, 753−759.

(27) (a) Charlton, J. L.; Alauddin, M. M. *Tetrahedron* **1987**, *43*, 2873−2889.

(b) Segura, J. L.; Martin, N. *Chem. Rev.* **1999**, *99*, 3199−3246.

(c) Yoshida, H.; Ohshita, J.; Kunai, A. *Bull. Chem. Soc. Jpn*. **2010**, *83*, 199−219.

(28) Cava, M.; Napier, D. R. *J. Am. Chem. Soc*. **1957**, *79*, 1701−1705.

(29) Quinkert, G.; Wiersdorff, W. W.; Finke, M.; Opitz, K.; von der Haar, F. G. *Chem. Ber.* **1968**, *101*, 2302−2325.

(30) Roth, W. R.; Ebbrecht, T.; Beitat, A. *Chem. Ber.* **1988**, *121*, 1357−1358.

(31) Yoshida, S.; Fujii, M.; Aso, Y.; Otsubo, T.; Ogura, F. *J. Org. Chem.* **1994**, *59*, 3077−3081.

(32) Ohta, A.; Yamashita, Y. *J. Chem. Soc., Chem. Commun.* **1995**, 1761−1762.

(33) (a) Iwashita, S.; Ohta, E.; Higuchi, H.; Kawai, H.; Fujiwara, K.; Ono, K.; Takenaka, M.; Suzuki, T. *Chem. Commun.* **2004**, 2076−2077.

(b) Suzuki, T.; Sakano, Y.; Iwai, T.; Iwashita, S.; Miura, Y.; Katoono, R.; Kawai, H.; Fujiwara, K.; Tsuji, Y.; Fukushima, T. *Chem. - Eur. J.* **2013**, *19*, 117−123.

(34) Shimizu, A.; Tobe, Y. *Angew. Chem., Int. Ed.* **2011**, *50*, 6906−6910.

(35) (a) Gleicher, G. J.; Newkirk, D. D.; Arnold, J. C. *J. Am. Chem. Soc.* **1973**, *95*, 2526−2531.

(b) Portella, G.; Poater, J.; Solà , M. *J. Phys. Org. Chem.* **2005**, *18*, 785−791.

Chapter 2
Synthesis and properties of 2,11-dibromo-13,14-dimesityl-5,8-dioxapentaphene and its radical cation

2-1. Introduction

In order to achieve the purpose of this study, i.e., the development of stable *o*-quinodimethane (*o*QDM) systems with superior electrochemical and photophysical properties, the main issue to be addressed was the stabilization of the *o*QDM structure. As described in **Chapter 1**, between the two methods used for *o*QDM stabilization, i.e., "annulation" and "anchoring", the latter is advantageous for preserving the intrinsic *o*QDM character. Moreover, the anchoring method allows the construction of fused cyclic frameworks in which the biradical form of *o*QDM is stabilized (Figure 2-1). In particular, I focused on the xanthyl scaffold, which was reported to form stable radical and cationic species,[1] and designed 5,8-dioxapentaphene (DOP) as a new *o*QDM system. The DOP skeleton, in which two peripheral benzene rings were anchored to the central *o*QDM moiety through oxygen bridges, can be considered as two xanthyl units condensed together. Thus, DOP is expected to form a stable *o*QDM system and stable cationic species. In this chapter, the synthesis and properties of DOP derivative 2,11-dibromo-13,14-dimesityl-5,8-dioxapentaphene (**11**) and its radical cation salt **11**$^{\bullet+}$•SbF_6^- are described. To the best of my knowledge, this is the first investigation of the electronic structure of an *o*QDM-based radical cation.

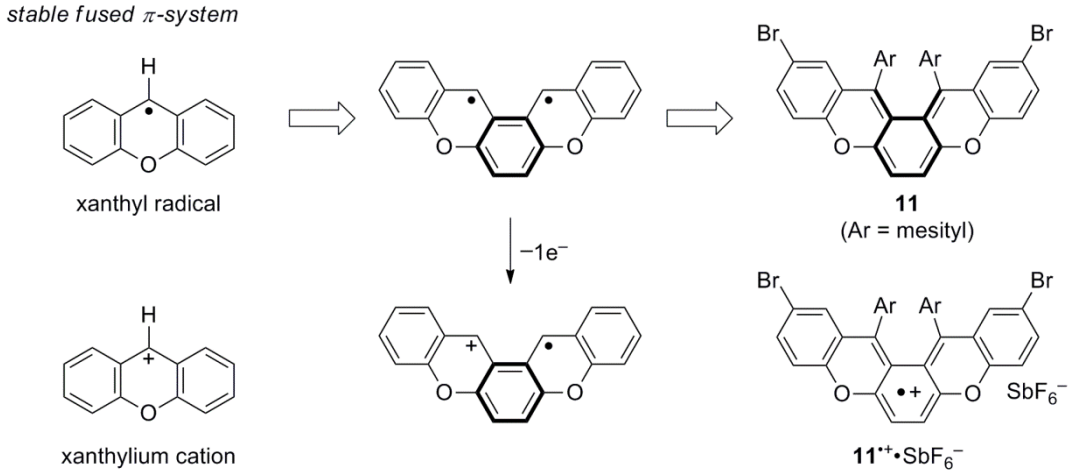

Figure 2-1. Strategy for the design of a stable *o*QDM system.

2-2. Synthesis of 2,11-dibromo-13,14-dimesityl-5,8-dioxapentaphene (11)

The synthesis of **11** is outlined in Scheme 2-1. Dinitrile **19** was prepared in 97% yield by the nucleophilic aromatic substitution of commercially available 5-bromo-2-fluorobenzonitrile with hydroquinone in the presence of K_2CO_3. The hydrolysis of dinitrile **19** under basic condition gave the corresponding dicarboxylic acid **20** in 82% yield. The polycyclic framework was regioselectively constructed by the Friedel–Crafts-like intramolecular cyclization of **20** using concentrated H_2SO_4,[2] to form the angularly fused-ring system **21** as the only product in 85% yield. The selective formation of **21** can be explained in terms of the shape of the HOMO in the singly cyclized (9-xanthone)oxidanium cation intermediate,[3] which has a large coefficient at the α-position rather than the β-position as shown by DFT calculations (Figure 2-2). Finally, the nucleophilic addition of mesityl Grignard reagent to dione **21** followed by the treatment with $SnCl_2$ afforded the desired product **11** in 75% yield over two steps. This simple and easy procedure allows the preparation of DOP **11** in multigram scale.

Scheme 2-1. Synthetic route of **11**.

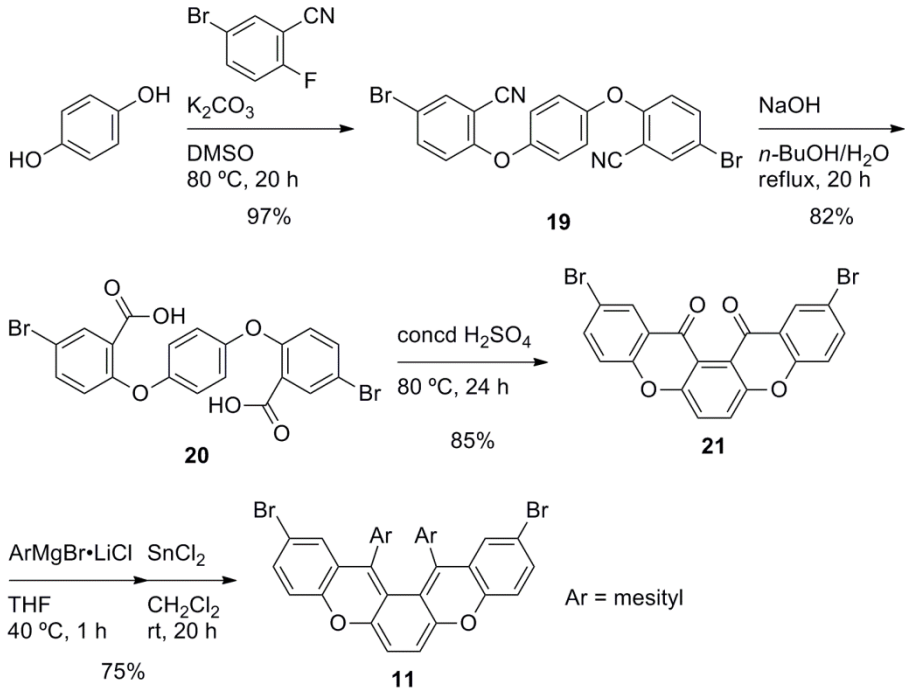

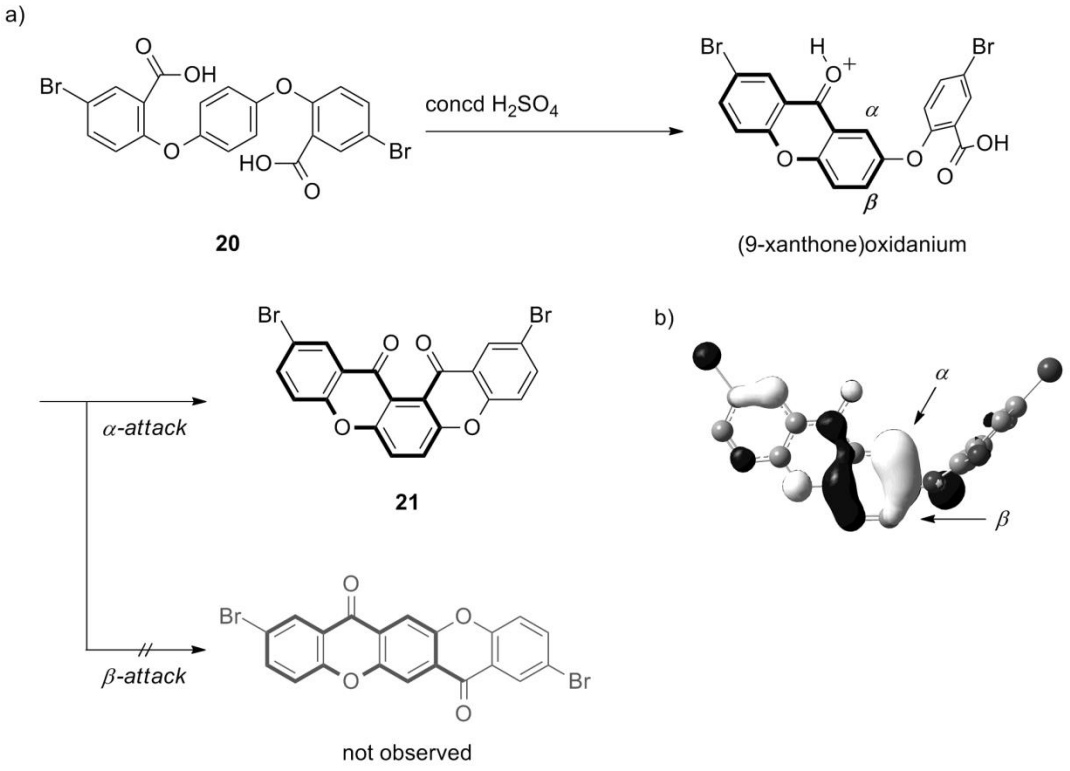

Figure 2-2. (a) Proposed reaction route of the regioselective cyclization of **21**. (b) HOMO of the reaction intermediate species (isovalue = 0.035) optimized by DFT at the RB3LYP/6-31G** level.

2-3. Molecular structure of 11 in the crystal state

In order to determine the detailed structure of **11**, X-ray structural analysis was carried out. Suitable single crystals were obtained by slow diffusion of *n*-hexane into the CH_2Cl_2 solution of **11**, and the crystal structure and crystallographic data are shown in Figure 2-3 and Table 2-1. In the crystal state, **11** exhibited a significantly twisted π-framework due to the steric repulsion around the two mesityl groups, in which the distance of the shortest contact was 3.146(3) Å between C26 and C31. The twisting angle was estimated to be 64.40° from the dihedral angle between the terminal rings *A* and *E*. This twisting induced the helicity in **11**, and the unit cell was composed of the two enantiomers (the *P*- and *M*-isomers, Figure2-3d) in a ratio of 1:1. The crystal structure of **11** showed distinct bond-length alternations around the central ring *C*; namely, C–C bonds *a* (1.359(3) Å), *c* (1.333(3) Å), *e* (1.333(3) Å), and *g* (1.359(3) Å) had double-bond nature, whereas *b* (1.458(3) Å), *d* (1.436(3) Å), *f* (1.461(3) Å), and *h* (1.485(3) Å) had single-bond nature. This result is consistent with the theoretical data reported for *o*QDM[4] and the experimental data of **10**,[5] clearly indicating that **11** is a homologue of *o*QDM.

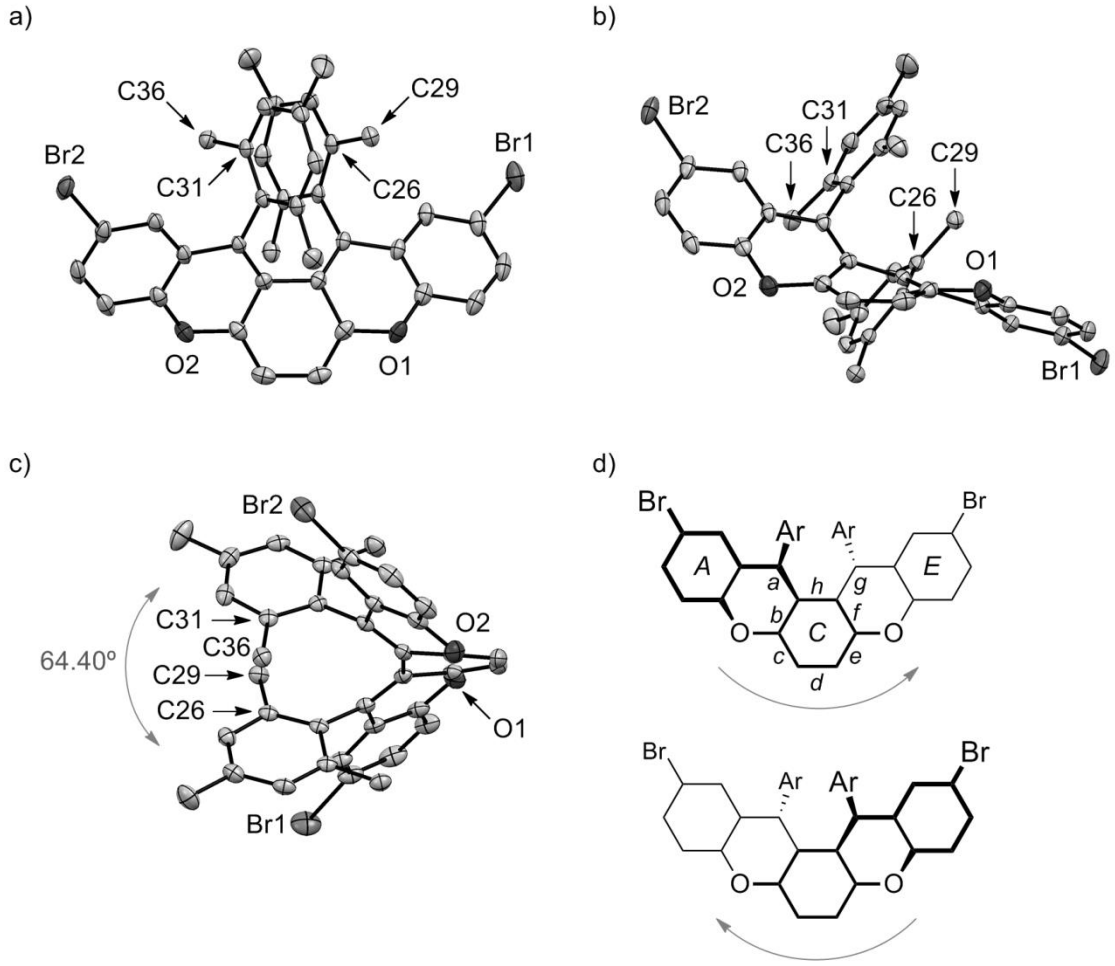

Figure 2-3. Crystal structure of **11**: (a) Top view and side views along (b) short axis and (c) long axis of its DOP unit. Hydrogen atoms are omitted for clarity. Thermal ellipsoids set at 50%. All crystal structures were displayed as the conformer with *M*-helicity. Gray double-headed arrow and value indicate the dihedral angle between the rings *A* and *E*. (d) Frameworks of the two enantiomers with *M*-helicity (top) and *P*-helicity (bottom). Gray arrows indicate the helical directions. Italic symbols denote assigned names of the selected bond and ring positions.

Table 2-1. Crystallographic data of **11**.

Formula	$C_{38}H_{30}Br_2O_2$	D_{calc} / g cm^{-3}	1.516
Formula weight	678.45	F(000)	688
Crystal color,	blue,	μ / cm^{-1}	27.69
morphology	block	No. of reflections	15130
Size / mm	0.10 × 0.05 × 0.03	measured	
Crystal system	triclinic	No. of unique	6667
Space group	P–1 (No. 2)	reflections	
a / Å	9.037(4)	No. of observed	5336
b / Å	12.111(5)	reflections	
c / Å	13.963(6)	No. of variables	409
α / degree	84.843(15)	Reflection	13.05
β / degree	77.598(10)	/ Parameter Ratio	
γ / degree	88.338(11)	R_1 [$I > 2.00\sigma(I)$]	0.0291
V / Å^3	1486.4(11)	R_w	0.0437
Z value	2	Goodness-of-fit	0.945
T / K	150		

2-4. Molecular structure and dynamics of 11 in the solution state

The ^{1}H NMR spectrum of **11** in $CDCl_3$ at room temperature displayed three singlet peaks in the aliphatic region, which are attributed to the methyl protons of the mesityl groups (Figure 2-4b). Surprisingly, one of the singlet peaks is shifted to a higher magnetic field at 0.86 ppm unlike the other singlet peaks (2.28 and 2.25 ppm), which were found in the region typical of benzylic protons. Judging from the crystal structure (Figure 2-3), the two sets of *o*-methyl protons on C29 and C36 are closely positioned on the facing mesityl rings, and are therefore affected by the ring-current effect. These results suggest that, in the solution state, **11** has a twisted structure similar to that observed in the crystal state. The aromatic region of the spectrum (Figure 2-4a) is consistent with this interpretation; namely, the two slightly broadened singlets at 6.83 and 6.64 ppm can be attributed to the aromatic protons of the mesityl groups, and the remaining four peaks (one double−doublet, two doublets, and one singlet) are assigned to the C_2-symmetric DOP protons. The singlet signal at 5.61 ppm, assigned to the central ring protons, shifted to a higher magnetic field compared to the chemical shifts reported for the corresponding protons of unsubstituted *o*QDM **6** (6.00 ppm),[6] 2,2-dimethyl-2*H*-indene (**22**; 6.08 ppm),[7] and 1,3-diphenyl-2,2-dimethyl-2*H*-indene (**23**; 6.34 ppm)[8] (Figure 2-5). This upfield shift can be partly attributed to the presence of the oxygen atoms at the 5- and 8-positions.

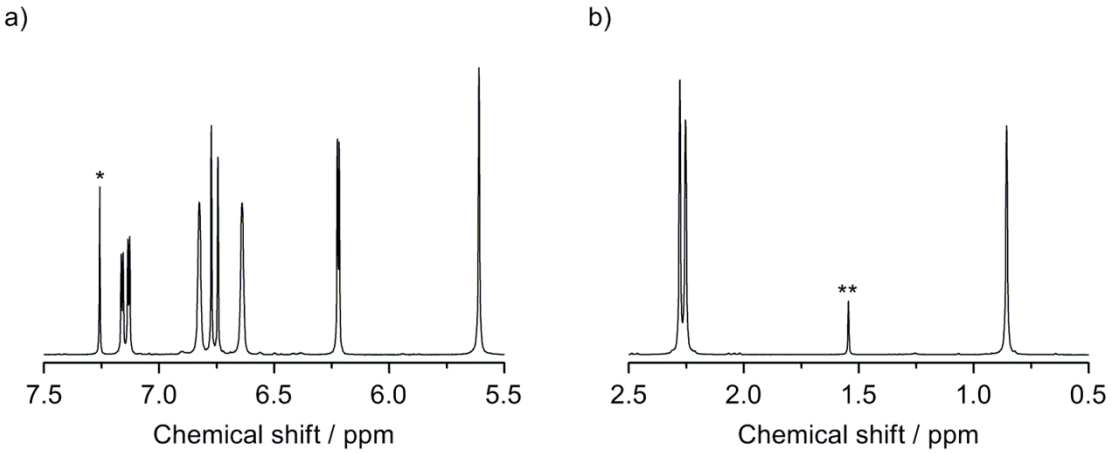

Figure 2-4. ^{1}H NMR spectrum of **11** in $CDCl_3$ at selected regions: (a) 7.50−5.50 (int × 3) and (b) 2.50−0.50 ppm; *chloroform, **water.

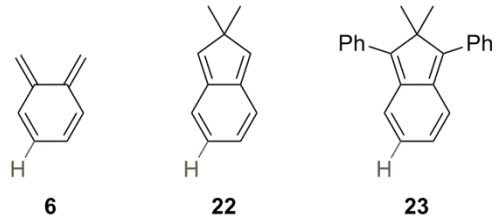

Figure 2-5. Chemical structures of cited *o*QDMs. Described gray ^{1}H nuclei indicate each compared proton.

In the ^{1}H NOESY spectrum of **11** in $CDCl_3$ at 298 K (Figure 2-6), intense cross-peaks were observed for the methyl (2.25 ppm of *D* and 0.86 ppm of *E*) and aromatic protons (6.83 ppm of *A* and 6.64 ppm of *B*) of the mesityl groups. This result indicates the site exchange between the correlated protons due to the flipping of the twisted DOP framework in the time scale of the measurement. Thus, **11** can be assumed to isomerize between the two helical enantiomers at around room temperature. To obtain further information on the racemization, the variable-temperature ^{1}H NMR studies were performed in *o*-dichlorobenzene-d_4 (Figure 2-7). As the measurement temperature increased, each pair of correlated peaks, i.e., *A*–*B* and *D*–*E*, shifted to the corresponding mean values with line-width broadening. Finally, the coalescence of *A*–*B* and *D*–*E* was observed at around 403 and 363 K, respectively. As a result, the racemization barrier $\Delta G^{\ddagger}$ was estimated to be ~75 kJ mol^{-1} by the coalescence method[9] (see Table 2-2). Because a racemization barrier of at least about 100 kJ mol^{-1} is required to perform optical resolution at room temperature,[10] the estimated $\Delta G^{\ddagger}$ value is not sufficient for enantiomeric resolution of **11**.

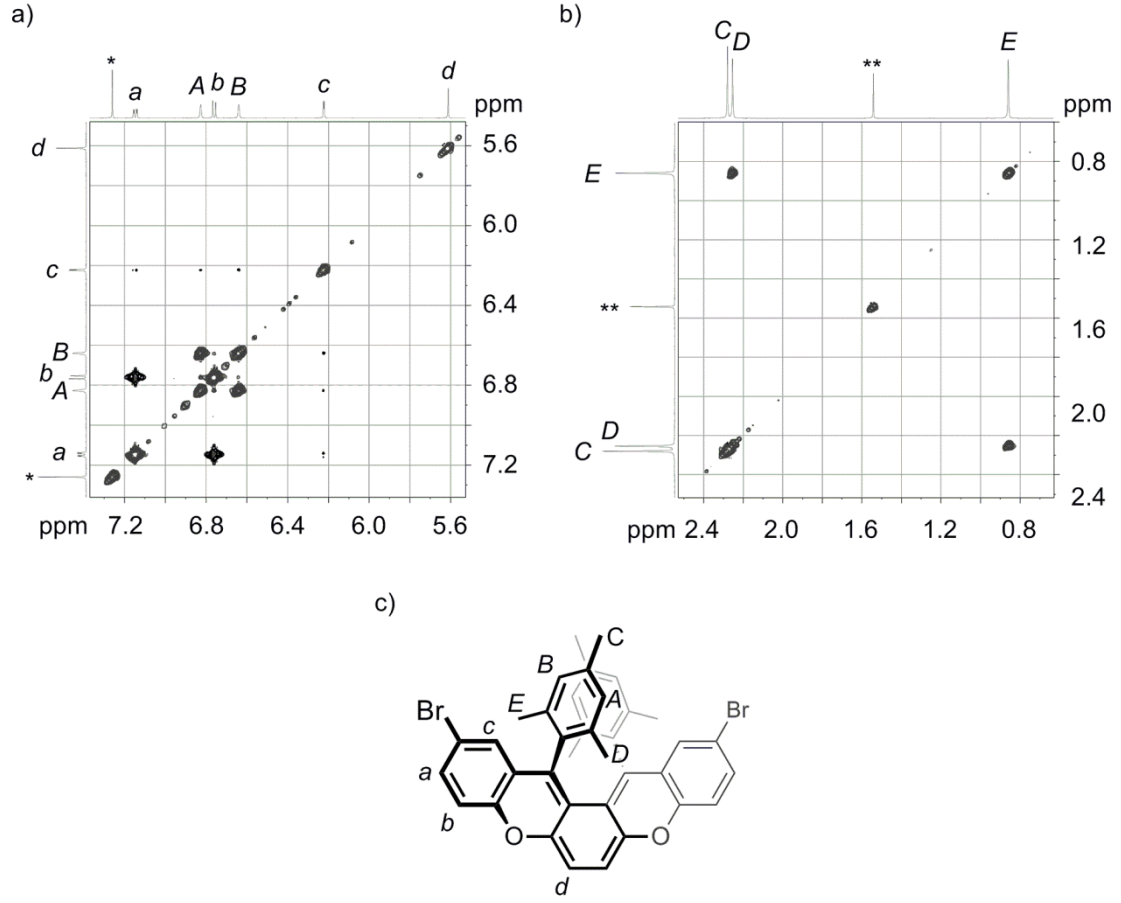

Figure 2-6. ^{1}H NOESY spectrum (600 MHz, 298 K) for **11** in $CDCl_3$ at selected regions: (a) 7.35–5.50 vs 7.35–5.50 ppm and (b) 2.50–0.60 vs 2.50–0.60 ppm; *chloroform, **water. (c) ^{1}H NMR assignments.

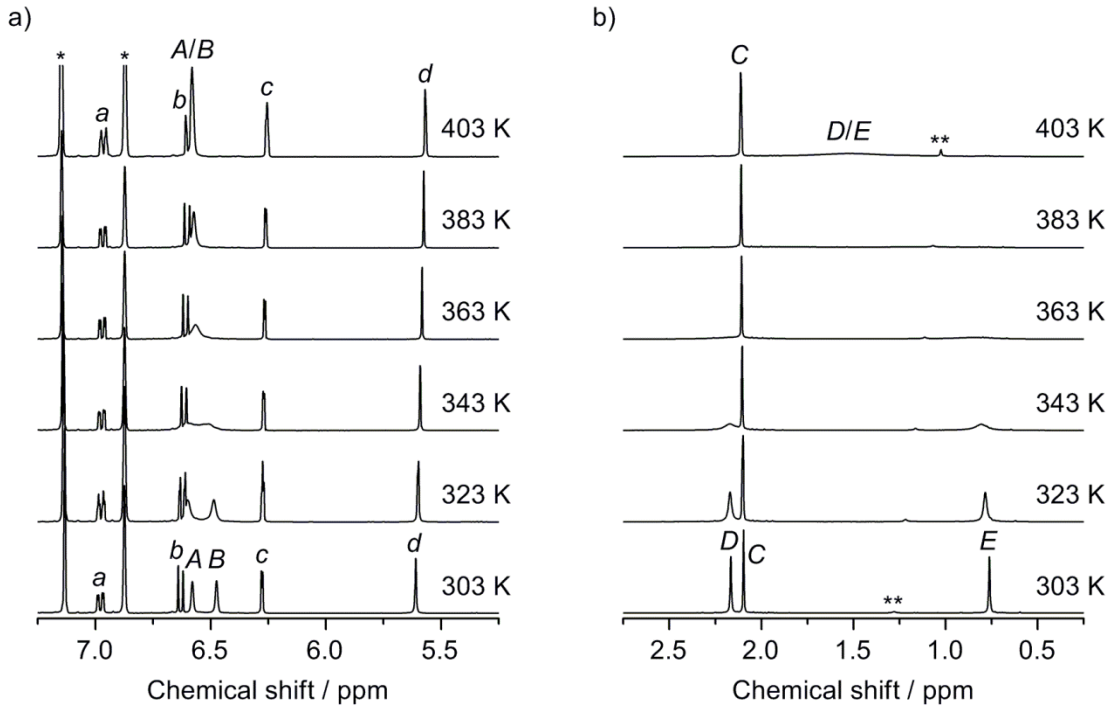

Figure 2-7. Temperature-dependent ^{1}H NMR spectra (from 303 K to 403 K, 400 MHz) of **11** in *o*-dichlorobenzene-d_4 at selected regions: (a) 7.25–5.25 (int × 2) and (b) 2.75–0.25 ppm; **o*-dichlorobenzene, **water. Assignments of signals are shown in Figure 2-6.

Table 2-2. Experimental values of chemical shifts (ν_1, ν_2), coalescence temperatures (T_c), and estimated energy barriers ($\Delta G^{\ddagger}$) for the racemization of **11** in *o*-dichlorobenzene-d_4.

Exchanging sites[a]	ν_1[b] / Hz	ν_2[b] / Hz	T_c / K	$\Delta G^{\ddagger}$[c] / kJ mol^{-1}
A–B	2630.6	2588.5	363	75.6
D–E	865.9	304.7	403	75.3

[a] Assignments of signals are shown in Figure 2-6. [b] Observed values at 303 K.

[c] The energy barrier ($\Delta G^{\ddagger}$) was estimated by the coalescence method[9] using the following equation:

$$\Delta G^{\ddagger} = RT_c \cdot \ln \frac{RT_c\sqrt{2}}{\pi N_A h \left|\nu_1 - \nu_2\right|}$$

where R is the gas constant, T_c is the observed coalescence temperature, N_A is Avogadro's number, h is Planck's constant, and ν_1 and ν_2 are the chemical shifts (in Hz) of the exchanging nuclei when the relative populations on these sites, n_1 and n_2, are the same (i.e., $n_1 = n_2$) and the effect of the temperature on these chemical shifts can be ignored.

2-5. Electronic structure and properties of 11

The UV–vis absorption spectrum of **11** in CH_2Cl_2 showed a broad absorption band in 450–700 nm region with maximum at 560 nm (ε = 1.04 × 10^4 M^{-1} cm^{-1}) despite the significantly decreased planarity of the π-system (Figure 2-8). The absorption band of **11** was similar in shape to that of 7,7,8,8-tetraphenyl-*o*QDM (**5**) but significantly red-shifted (**5**: λ_{max} = 520 nm, λ_{edge} ≈ 620 nm),[11] indicating that the π-conjugation of the *o*QDM moiety in **11** extended through the two oxygen bridges. Moreover, **11** showed a negligible spectral change for over a week under daylight and aerated conditions at room temperature. These results are clear evidence that **11** is a highly stable *o*QDM derivative.

To gain insight into the electronic structure of the DOP skeleton, the theoretical calculation for **11** and **24** (Ar = H) were performed (Figure 2-9 and Table 2-3). Structural optimization for **11** using DFT calculations at the RB3LYP/6-31** level resulted in a structure similar to the crystal structure, whereas the optimized structure of **24** was completely flat because of the lack of steric congestion. The calculated HOMO and LUMO energies were –4.63 and –2.27 eV for **11** and –4.47 and –2.61 eV for **24,** respectively, indicating that twisting of the DOP skeleton has a large effect on the LUMO and little effect on the HOMO energy levels. In addition, I estimated the biradical character of **11** and **24**. The amount of singlet biradical character depends on the coupling strength between two electrons.[12] Here, we consider two sites, described as "**A**–**B**", each having one electron. In case of fully covalent coupling between the two electrons, these two sites can be described as "**A**=**B**", representing a perfectly closed-shell system. On the other hand, in the absence of coupling, these two sites can be described as "**A**$^{\bullet}$–**B**$^{\bullet}$", which corresponds to a perfectly open-shell singlet biradical system with two nonbonding orbitals. The degree of electron splitting can be explained by the degree of HOMO (bonding)–LUMO (anti-bonding) mixing. Thus, the biradical character can be estimated from the occupation number of LUMO (n) at the ground state using theoretical calculations, where $0 \leq n \leq 1$ and n = 0 and 1 correspond to perfectly closed- and open-shell systems, respectively. The n values estimated by the CASSCF(2,2)/6-31G method[13] were 0.091 for **11** and 0.090 for **24**. This result indicates that the biradical characters were nearly independent of the degree of twisting, and that **11** has an almost closed-shell configuration, which is consistent with the distinct bond-length alternations observed in its crystal structure.

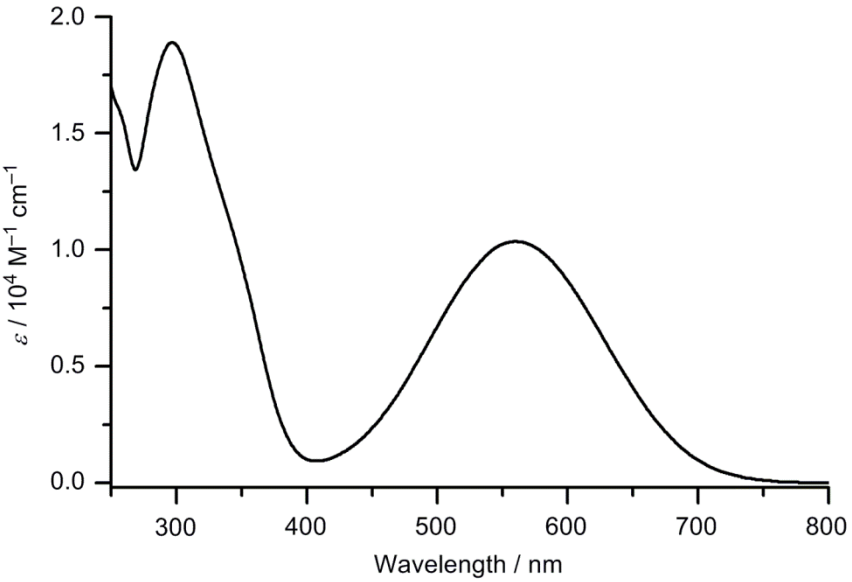

Figure 2-8. UV−vis absorption spectrum of **11** in CH_2Cl_2.

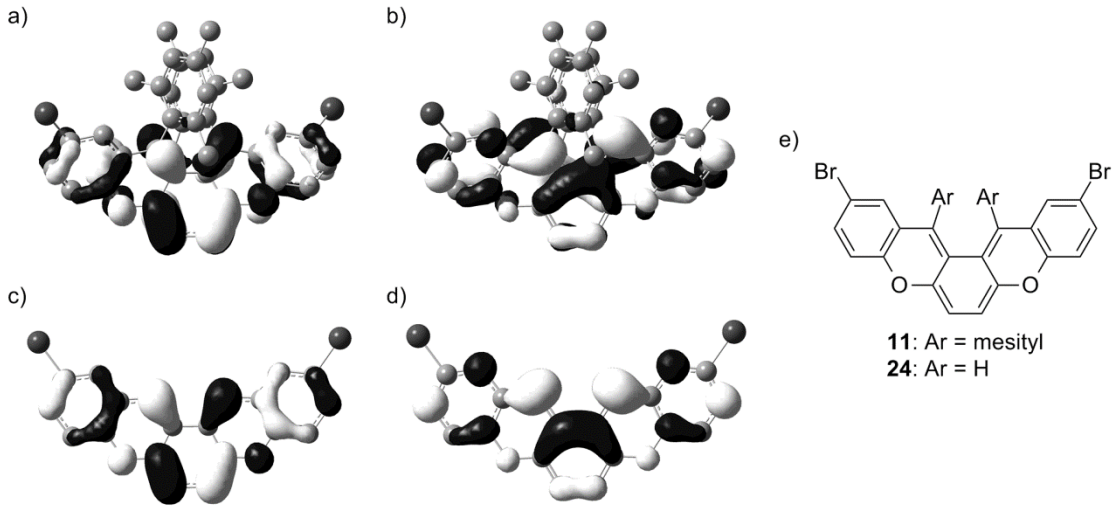

Figure 2-9. Calculated structures and orbitals; (a) HOMO and (b) LUMO of **11**, and (c) HOMO and (d) LUMO of **24** (isovalue = 0.030) optimized by DFT at the RB3LYP/6-31G** level. (e) Chemical structures of **11** and **24**.

Table 2-3. Theoretical calculation values of **11** and **24**.

Compounds[a]	Twisting angle[b] / deg	HOMO energy / eV	LUMO energy / eV	Occupation number of LUMO (*n*)[c]
11	69.82	–4.630	–2.270	0.0913711
24	0.00	–4.471	–2.610	0.0901861

[a] All geometries were optimized at the DFT RB3LYP/6-31G** level. [b] Estimated from dihedral angle between the terminal rings *A* and *E* as shown in Figure 2-3. [c] Calculated at the CASSCF(2,2)/6-31G level.

The cyclic voltammogram of **11** in CH_2Cl_2 (Figure 2-10) exhibited two reversible oxidation waves and one reversible reduction wave (E^{ox2} = +0.42 V, E^{ox1} = +0.07 V, E^{red1} = –2.00 V vs Fc/Fc^+), suggesting the reversible amphoteric redox behavior of **11**, which results in the formation of the electrochemically stable cationic and anionic species. In particular, the first oxidation potential was significantly lower than that of previously reported stable *o*QDM derivatives (**9**[14]: +0.42 V vs Ag/AgCl, **10**[5]: +0.59 V vs Fc/Fc^+), indicating the superior electron-donating ability of **11**. To clarify the first oxidation process, the spectral change of **11** during electrochemical oxidation were investigated by applying an external potential of +0.20 V (vs Fc/Fc^+). During the oxidation, absorption peaks at λ_{max} = 252, 329, and 608 nm and a broad NIR absorption band appeared with isosbestic points (Figure 2-11). The TD-DFT calculations suggested that the observed absorption change can be ascribed to the formation of the corresponding radical cationic species $\mathbf{11}^{\bullet+}$ (Table 2-4).

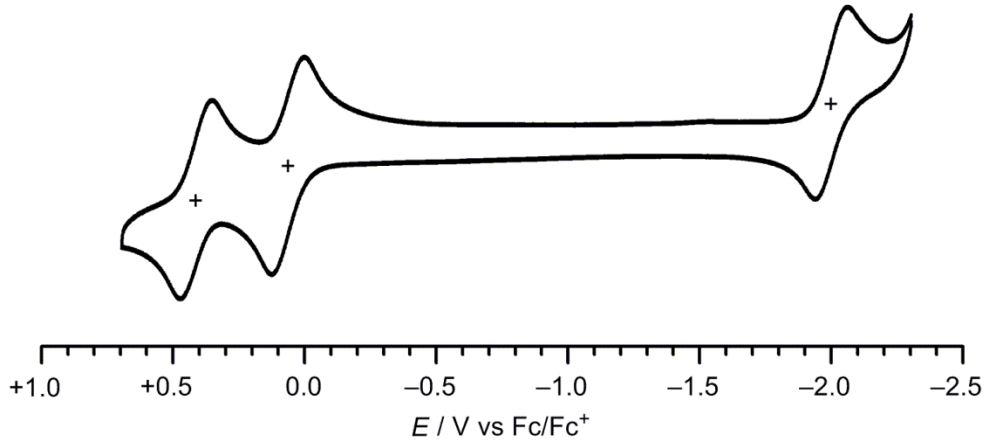

Figure 2-10. Cyclic voltammogram of **11** in CH_2Cl_2 containing 0.1 M *n*-Bu_4NPF_6 as a supporting electrolyte at a scan rate of 100 mV s^{-1}.

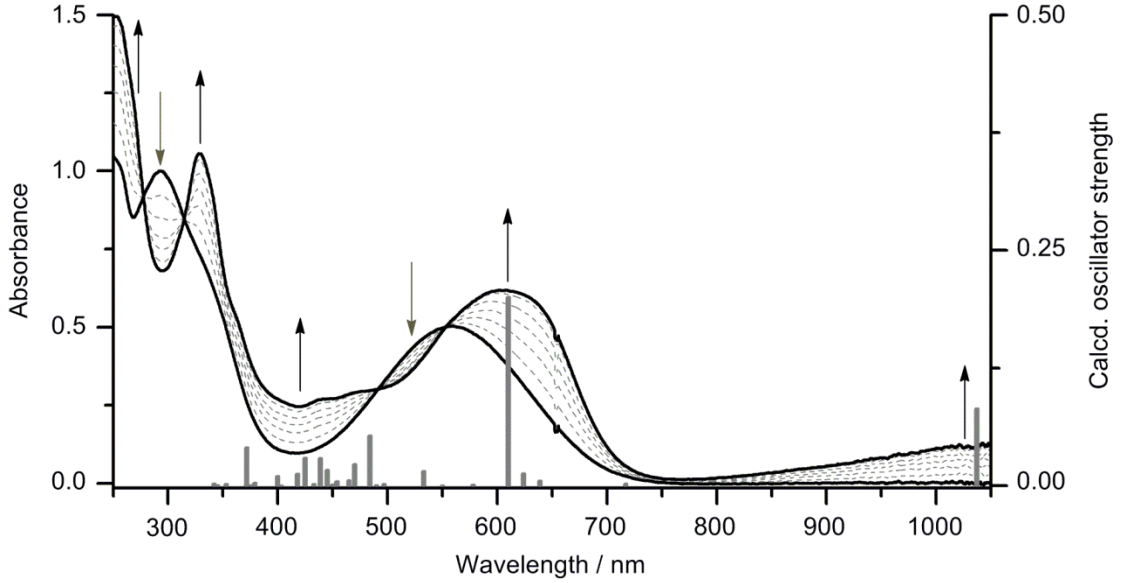

Figure 2-11. UV–vis spectral change of **11** during the electrochemical oxidation (at –0.20 V vs Fc/Fc^{+}) in CH_2Cl_2 containing 0.1 M *n*-Bu_4NPF_6. The dash lines show intermediate states. The gray solid bars show the theoretical values of excitation wavelengths and oscillator strengths for $\mathbf{11}^{\bullet+}$ calculated by TD-DFT at the UB3LYP/6-31G**//UB3LYP/6-31G** level. See also Table2-4.

Table 2-4. Characteristic excitation energies of $\mathbf{11}^{\bullet+}$ calculated by TD-DFT at the UB3LYP/6-31G**//UB3LYP/6-31G** level.

Excited states	Transition energies / eV (Wavelength / nm)	Main CI coefficients	Oscillator strengths
1	1.1959 eV (1036.76 nm)	SOMO(α)–LUMO(α) 0.97461	0.0820
5	2.0332 eV (609.78 nm)	HOMO(β)–SOMO(β) 0.94036	0.2004

2-6. Isolation of radical cation salt $11^{\bullet+}\bullet SbF_6^-$ and investigation of its properties

The chemical oxidation of **11** was achieved using tris(4-bromophenyl)aminium hexafluoroantimonate (TBPA•SbF_6) as an oxidant (Scheme 2-2). The treatment of a CH_2Cl_2 solution of **11** with 1 equiv of TBPA•SbF_6 afforded the desired radical cation salt $\mathbf{11}^{\bullet+}\bullet SbF_6^-$, which was isolated in 75% yield as a dark blue solid by reprecipitation from the CH_2Cl_2 solution using ether. The obtained solid of $\mathbf{11}^{\bullet+}\bullet SbF_6^-$ was stable under aerated conditions at room temperature. The UV−vis−NIR spectrum of $\mathbf{11}^{\bullet+}\bullet SbF_6^-$ in CH_2Cl_2 was consistent with that observed upon the electrochemical oxidation. The significantly broadened absorption in the range 750–1800 nm (Figure 2-12) can be assumed as a charge-resonance band associated with the SOMO−LUMO transition by means of the TD-DFT calculations (Figure 2-13 and Table 2-4).

The electron-spin resonance (ESR) spectrum of $\mathbf{11}^{\bullet+}\bullet SbF_6^-$ in degassed CH_2Cl_2 at room temperature exhibited a clear triplet line resulting from the hyperfine coupling with two equivalent ^{1}H nuclei (I = 1/2) with g = 2.0038 (Figure 2-14). The observed ESR spectrum was reproduced by spectral simulation with an estimated hyperfine coupling constant of $|a^{1H}|$ (×2) = 0.330 mT. These results confirm that the electron spin density was mainly localized in the *o*QDM moiety. The calculated spin density is consistent with the experimental results (Figure 2-15).

Scheme 2-2. Synthesis of $\mathbf{11}^{\bullet+}\bullet SbF_6^-$.

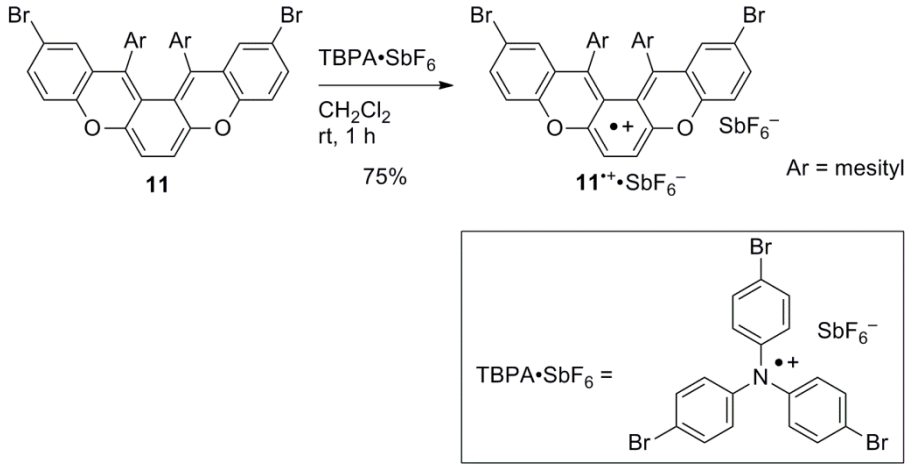

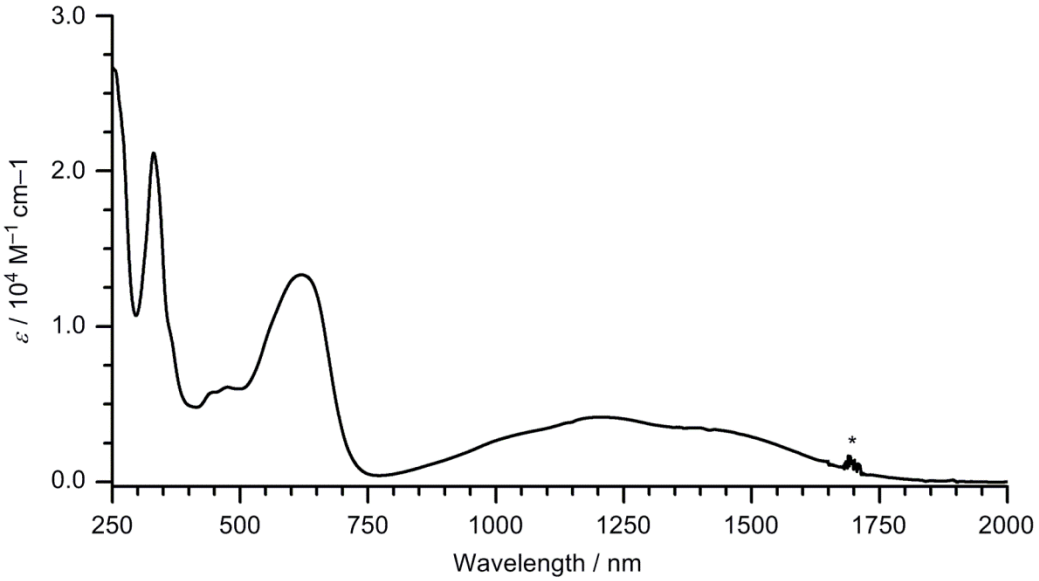

Figure 2-12. UV−vis−NIR absorption spectrum of $\mathbf{11}^{\bullet+}$•SbF_6^- in CH_2Cl_2; * solvent peaks.

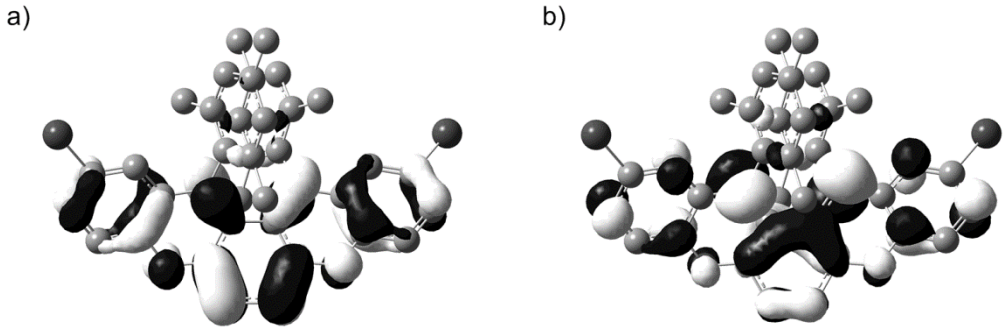

Figure 2-13. (a) SOMO(α) and (b) LUMO(α) of $\mathbf{11}^{\bullet+}$ (isovalue = 0.03) optimized at the DFT UB3LYP/6-31G** level. Hydrogen atoms are omitted for clarity.

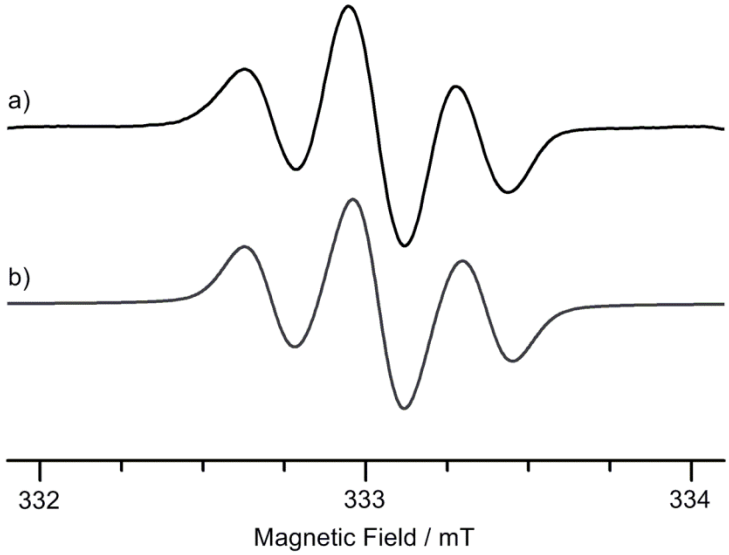

Figure 2-14. (a) Observed and (b) simulated ESR spectra of $\mathbf{11}^{\bullet+}\bullet SbF_6^-$ in CH_2Cl_2 at room temperature. Parameters for simulation: g = 2.0038, $|a^{1H}|$ (×2) = 0.330 mT.

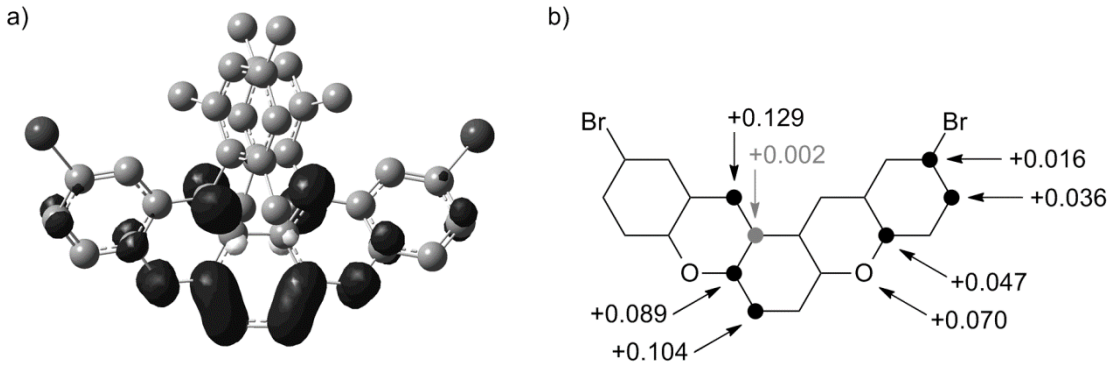

Figure 2-15. (a) Spin density map (isovalue = 0.002, black: positive spin, white: negative spin) and (b) values (mean value) of $\mathbf{11}^{\bullet+}$ optimized at the DFT UB3LYP/6-31G** level.

2-7. Experimental section

General Methods

- Melting points were taken on a Yanaco MP J-3 and were uncorrected.
- ^{1}H and ^{13}C NMR spectra were recorded on a Bruker Avance III 300 spectrometer (300 MHz for ^{1}H and 75 MHz for ^{13}C) and a Bruker Avance III 400 spectrometer (400 MHz for ^{1}H).
- ^{1}H–^{1}H NOESY spectrum of **11** was recorded on a Bruker Avance III 600 spectrometer (600 MHz for ^{1}H).
- Variable temperature ^{1}H NMR spectra of **11** were recorded on a JEOL ECZ-400 spectrometer (400 MHz for ^{1}H).

  # Chemical Shifts were reported in parts per million downfield for tetramethylsilane as an internal standard or relative to solvent signal (chloroform: δ = 7.26 for ^{1}H NMR and δ = 77.0 ppm for ^{13}C NMR; dimethyl sulfoxide: δ = 2.50 for ^{1}H NMR and δ = 39.5 ppm for ^{13}C NMR; trifluoroacetic acid: δ = 11.50 for ^{1}H NMR and δ = 164.2 and 116.6 ppm for ^{13}C NMR; *o*-dichlorobenzene: δ = 7.19 and 6.93 ppm for ^{1}H NMR) as internal standards, and all coupling constants are reported in Hz (Multiplicity: s = singlet; d = doublet; br = broad).
- IR spectra were recorded on a JASCO FT/IR-4600 spectrometer.
- APCI-TOF and ESI-TOF mass spectra were recorded on a Bruker micrOTOF II spectrometer.
- High-resolution mass spectrum (ESI-TOF) was recorded on a JEOL AccuTOF spectrometer.
- Elemental analyses were obtained from the Analytical Center in Osaka City University, using a Fisons EA1108 and a J-Science JM10.
- X-ray data were collected by a Rigaku Saturn 724 CCD system with graphite monochromated Mo-Kα radiation.
- Absorption spectra were recorded on a Shimadzu UV-2550 spectrometer and a JASCO V670 spectrometer.
- Redox potential was measured using an ALS Electrochemical analyzer MODEL 610A in a conventional three-electrode cell equipped with a glassy carbon as a working electrode and a platinum wire as a counter electrode with a SCE reference electrode. The measurement was carried out at a scan rate 100 mV s^{-1} in dichloromethane containing 0.1 M tetra-*n*-butylammonium hexafluorophosphate as a supporting electrolyte. The redox potentials were finally corrected by the ferrocene/ferrocenium (Fc/Fc^{+}) couple.
- Absorption spectra of the oxidation species for **11** were recorded on an Ocean Optics HR4000 spectrometer using a 1 mm width cell equipped with a fine mesh platinum as a working electrode, a platinum wire as a counter electrode, and a SCE reference electrode. The external potential of –0.20 V vs Fc/Fc^{+} (+0.39 V vs SCE) was applied using a Bi-Potentiostat ALS/DY2323 for the electrochemical oxidation of **11** in dichloromethane containing 0.1 M tetra-*n*-butylammonium hexafluorophosphate.
- ESR spectrum of $\mathbf{11}^{\bullet+}\bullet SbF_6^{-}$ was recorded on a Bruker ELEXSYS E500 spectrometer.

Materials

- Merck gel 60 (63–200 mesh) or Kanto Chemical Silica gel 60 (100–200 mesh) were used for column chromatography.
- The progress of reactions was monitored using thin-layer chromatography using Merck TLC silica gel 60 F254.
- All commercially available compounds were reagent grade and used without further purification.
- Dehydrate dimethyl sulfoxide was purchased.
- Tetrahydrofuran was dried and distilled over sodium.
- Dichloromethane was dried and distilled over calcium hydride.

Synthetic procedures and compounds data

1,4-Bis(4-bromo-2-cyanophenoxy)benzene (19)

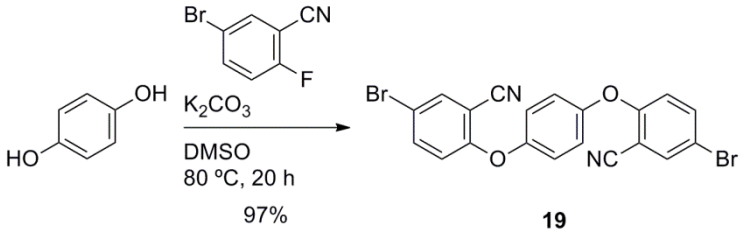

Hydroquinone (3.30 g, 30.0 mmol), 5-bromo-2-fluorobenzonitrile (13.2 g, 66.0 mmol), and K_2CO_3 (9.95 g, 72.0 mmol) were placed in a 200 mL two-necked round bottom flask with DMSO (45 mL). The mixture was degassed by an N_2-bubbling for 10 min and heated at 80 °C under stirring for 20 h. After cooling to rt, the reaction mixture was quenched by an addition of large amount of water. The resulting precipitate was collected by filtration, and the residue was washed with water and ethanol to obtain **19** (13.7 g, 97%) as a white powder.

19: $C_{20}H_{10}Br_2N_2O_2$; MW 470.11; mp 266–267 °C; ^{1}H NMR (300 MHz, $CDCl_3$, δ): 7.78 (d, J = 2.5 Hz, 2H), 7.61 (dd, J = 8.9 and 2.5 Hz, 2H), 7.13 (s, 4H), 6.80 (d, J = 8.9 Hz, 2H); ^{13}C NMR (75 MHz, $CDCl_3$, δ): 158.69, 151.83, 137.43, 136.17, 121.75, 118.49, 115.14, 114.40, 105.52; IR (KBr) ν_{max} (cm^{-1}): 3096, 3074, 2226, 1591, 1498, 1473, 1458, 1389, 1264, 1244, 1192, 1170, 1119, 1095, 1011, 881, 859, 829, 806, 534, 493; MS (APCI-TOF$^+$) m/z (%): 468.9 (59%), 470.9 (100%), and 472.9 (60%) [M + H$^+$]; Anal Calcd for $C_{20}H_{10}Br_2N_2O_2$: C, 51.10; H, 2.14; N, 5.96. Found: C, 50.82; H, 2.21; N, 5.97.

1,4-Bis(4-bromo-2-carboxyphenoxy)benzene (20)

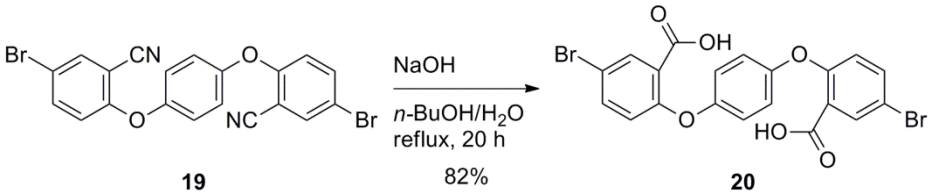

19 **20**

1,4-Bis-(4-bromo-2cyanophenoxy)benzene (**19**) (470 mg, 1.00 mmol) and NaOH (500 mg, 12.5 mmol) were placed in a 50 mL round bottom flask with *n*-butanol (8 mL) and water (2 mL), and the mixture was refluxed under stirring for 20 h. After cooling to rt, the resulting mixture was diluted with 2 M aq NaOH. The aqueous layer was washed with dichloromethane and then acidified by an addition of 12 M aq HCl to pH 1–2 at 0 °C. The resulting suspension was extracted with ethyl acetate. The combined organic layer was dried over anhydrous Na_2SO_4, and the solvent was removed under reduced pressure to obtain **20** (418 mg, 82%) as a white powder.

20: $C_{20}H_{12}Br_2O_6$; MW 505.90; mp 285–286 °C; ^{1}H NMR (400 MHz, DMSO-d_6, δ): 13.25 (br, 2H), 7.91 (d, J = 2.6 Hz, 2H), 7.71 (dd, J = 8.8 and 2.7 Hz, 2H), 7.00 (s, 4H), 6.94 (d, J = 8.8 Hz, 2H); ^{13}C NMR (75 MHz, DMSO-d_6, δ): 165.30, 154.90, 152.47, 136.06, 133.51, 126.00, 122.25, 119.93, 115.11; IR (KBr) ν_{max} (cm^{-1}): 2974 (br), 2626 (br), 1704, 1681, 1592, 1570, 1497, 1474, 1442, 1407, 1304, 1266, 1231, 1188, 1100, 1012, 930, 908, 862, 810, 750, 674, 643, 587, 527; MS (APCI-TOF$^-$) m/z (%): 504.8 (52%), 506.8 (100%), and 508.8 (54%) [M – H$^-$]; Anal Calcd for $C_{20}H_{12}Br_2O_6$: C, 47.28; H, 2.38. Found: C, 47.23; H, 2.49.

2,11-Dibromo-13,14-dihydro-5,8-dioxapentaphene-13,14-dione (21)

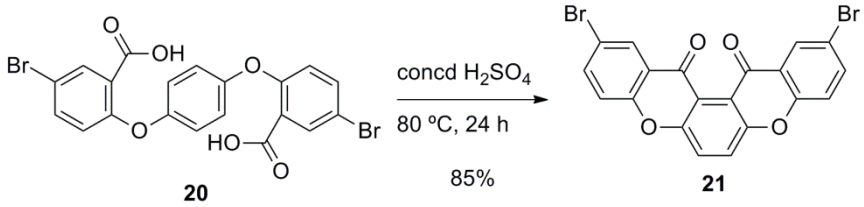

20 **21**

In a 30 mL round bottom flask, 1,4-bis(4-bromo-2-carboxyphenoxy)benzene (**20**) (894 mg, 1.76 mmol) was dissolved with 18 M H_2SO_4 (8 mL), and the mixture was stirred at 80 °C for 24 h. After cooling to rt, the resulting mixture was added dropwise into ice-cooled water to quench the reaction. The generated precipitate was collected by filtration and rinsed with water. The residue was washed with 2 M aq NaOH, water, and ethanol, successively. After drying under reduced pressure, the crude powder was dissolved in *o*-dichlorobenzene under heating at 180 °C, and the resulting solution was immediately passed through cotton-pad to remove insoluble solid. After cooling the filtrate to rt, the generated precipitate was collected by filtration and rinsed with ethanol to obtain **21** (705 mg, 85%) as a pale yellow solid.

21: $C_{20}H_8Br_2O_4$; MW 469.88; mp > 300 °C; ^{1}H NMR (400 MHz, CF_3COOD, δ): 8.90 (d, J = 2.3 Hz, 2H), 8.62 (s, 2H), 8.35 (dd, J = 9.1 and 2.4 Hz, 2H), 7.89 (d, J = 9.1 Hz, 2H); ^{13}C NMR (75 MHz, CF_3COOD, δ): 182.32, 160.11, 156.99, 145.77, 133.92, 131.43, 124.07, 121.72, 121.29, 117.55; IR (KBr) ν_{max} (cm^{-1}): 3098, 1681, 1657, 1607, 1590, 1469, 1453, 1419, 1314, 1273, 1217, 1160, 1126, 1035, 895, 812, 769, 687, 661, 631, 527; MS (APCI-TOF$^+$) m/z (%): 470.9 (51%), 472.9 (100%), and 474.9 (51%) [M + H$^+$]; Anal Calcd for $C_{20}H_8Br_2O_4$: C, 50.88; H, 1.71. Found: C, 50.74; H, 1.90.

2,11-Dibromo-13,14-dimesityl-5,8-dioxapentaphene (11)

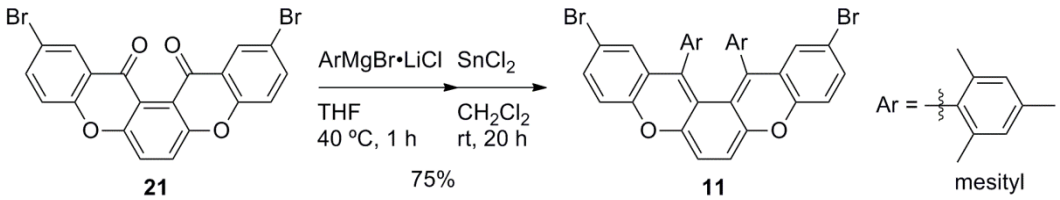

To prepare mesityl Grignard reagent, in a 30 mL two-necked round bottom flask under an N_2 atmosphere, the solution of 2-bromomesitylene (3.19 g, 16.0 mmol) in THF (8 mL) was added slowly to the suspension of anhydrous LiCl (593 mg, 14.0 mmol) and Mg turnings (336 mg, 14.0 mmol) in THF (8 mL) at 40 °C, and the mixture was stirred for 1 h.

In another 50 mL two-necked round bottom flask under an N_2 atmosphere, 2,11-dibromo-13,14-dihydro-5,8-dioxapentaphene-13,14-dione (**21**) (1.89 g, 4.00 mmol) was placed with THF (30 mL) at 40 °C. To the suspension of **21** was added dropwise slowly the prepared mesityl Grignard reagent, and then the mixture was stirred for 1 h. After cooling to rt, 4 M aq HCl was added to quench the reaction. The aqueous layer was extracted with dichloromethane, and the combined organic layer was dried over Na_2SO_4. A removal of the solvent under reduced pressure gave the crude mesitylated diol.

The obtained crude diol was dissolved in dichloromethane (60 mL), and the mixture was degassed by an N_2-bubbling for 5 min. After the degassing, a drop of 4 M aq HCl and anhydrous $SnCl_2$ (4.55 g, 24.0 mmol) were added, and then the mixture was stirred at rt for 20 h. The resulting mixture was passed through Celite® to remove the excess amount of $SnCl_2$, and then the filtrate was concentrated under reduced pressure. The residue was passed through a short column on silica gel using dichloromethane as eluent. After a removal of the solvent, the crude solid was washed with ethanol to obtain **11** (2.03 g, 75 %) as a dark bluish-purple solid. Single crystals of **11** suitable for X-ray analysis were obtained by a liquid diffusion of *n*-hexane with a solution of **11** in CH_2Cl_2.

11: $C_{38}H_{30}Br_2O_2$; MW 678.45; mp 290–295 °C (decomp); ^{1}H NMR (300 MHz, $CDCl_3$, δ): 7.15 (dd, J = 8.5 and 2.4 Hz, 2H), 6.83 (s, 2H), 6.76 (d, J = 8.5 Hz, 2H), 6.64 (s, 2H), 6.22 (d, J = 2.4 Hz, 2H), 5.61 (s, 2H), 2.28 (s, 6H), 2.25 (s, 6H), 0.86 (s, 6H); ^{13}C NMR (75 MHz, $CDCl_3$, δ): 154.44, 145.19, 140.15, 137.85, 135.57, 135.48, 132.04, 130.89, 129.57, 129.00, 128.71, 128.58, 125.59, 116.75, 114.21, 102.33, 21.04, 20.43, 19.83; IR (KBr) ν_{max} (cm^{-1}): 3066, 2961, 2915, 2854, 1643, 1609, 1588, 1468, 1441, 1393, 1339, 1283, 1262, 1233, 1206, 1119, 1077, 1018, 889, 849, 815, 742, 718, 596; MS (APCI-TOF$^+$) *m*/*z* (%): 677.0 (51%), 679.0 (100%), and 681.0 (56%) [M + H$^+$]; HRMS (ESI-TOF$^+$) *m*/*z*: Calcd. For $^{12}C_{38}{}^{1}H_{31}{}^{79}Br^{81}Br^{16}O_2$: 679.0670, Found: 679.0667 [M + H$^+$]; Anal Calcd for $C_{38}H_{30}Br_2O_2$: C, 67.27; H, 4.46. Found: C, 66.84; H, 4.55.

Radical cation hexafluoroantimonate salt $11^{\bullet+}\bullet SbF_6^-$

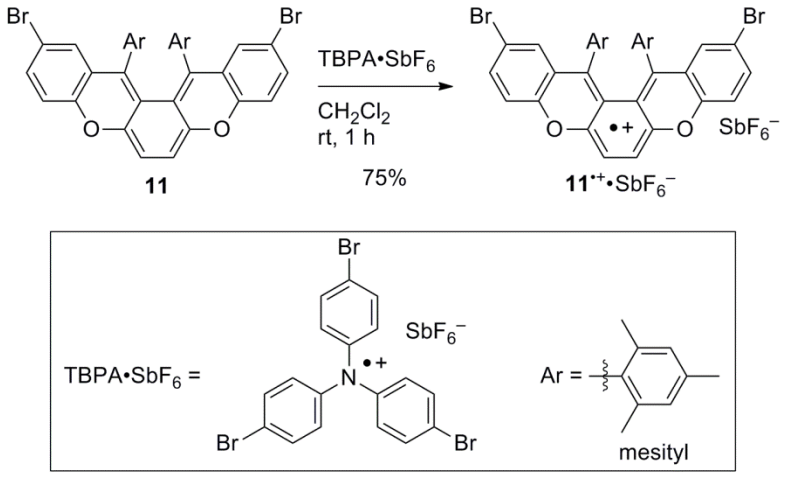

In a glove box filled with argon, 2,11-dibromo-13,14-dimesityl-5,8-dioxapentaphene (**11**) (67.8 mg, 0.100 mmol) was dissolved in dichloromethane (5 mL). To this solution was added a solution of tris(4-bromophenyl)aminium hexafluoroantimonate ($TBPA\bullet SbF_6$, 70.0 mg, 0.975 mmol) in dichloromethane at rt, and the mixture was stirred for 1 h. The resulting mixture was evaporated under reduced pressure. The residue was dissolved in a minimum amount of dichloromethane, and then ether was added slowly. The generated precipitate was collected by filtration to obtain $\mathbf{11}^{\bullet+}\bullet SbF_6^-$ (67.7 mg obtained as $\mathbf{11}^{\bullet+}\bullet SbF_6^-\bullet(CH_2Cl_2)_{0.5}$, 71%) as a dark blue solid.

$\mathbf{11}^{\bullet+}\bullet SbF_6^-$: $C_{38}H_{30}Br_2F_6O_2Sb$; MW 914.20; mp 205–210 °C (decomp); IR (KBr) ν_{max} (cm^{-1}): 3097, 2985, 2951, 2917, 2857, 1607, 1562, 1536, 1469, 1450, 1372, 1303, 1264, 1216, 1188, 1142, 1075, 1045, 820, 742, 719, 657, 598, 545; MS (ESI-TOF$^+$) *m*/*z* (%): 676.1 (52%), 678.1 (100%), and 680.1 (57%) [$C_{38}H_{30}Br_2O_2^+$], (ESI-TOF$^-$) *m*/*z* (%): 234.9 (100%) and 236.9 (75%) [SbF_6^-]; Anal Calcd for $(C_{38}H_{30}Br_2O_2\bullet SbF_6)\bullet(CH_2Cl_2)_{0.5}$: C, 48.34; H, 3.27. Found: C, 47.97; H, 3.45.

2-8. References

(1) (a) Maruyama, K.; Arakawa, S. *Bull. Chem. Soc. Jpn.* **1974**, *58*, 1960−1966.
(b) Clifton, M. F.; Fenick, D. J.; Gasper, S. M.; Falvey, D. E.; Boyd, M. K. *J. Org. Chem.* **1994**, *59*, 8023−8029.
(c) Okada, K.; Imakura, T.; Oda, M.; Kajiwara, A.; Kamachi, M.; Yamaguchi, M. *J. Am. Chem. Soc.* **1997**, *119*, 5740−5741.

(2) (a) Ullmann, F.; Maag, R. *Ber. Dtsch. Chem. Ges.* **1906**, *39*, 1693−1696.
(b) Badger, G. M.; Pettit, P. *J. Chem. Soc.* **1952**, 1874−1877.

(3) (a) Watanabe, M.; Suzuki, H.; Tanaka, Y.; Ishida, T.; Oshikawa, T.; Tori-i, A. *J. Org. Chem.* **2004**, *69*, 7794−7801.
(b) Yamada, S.; Iwama, S.; Kinoshita, K.; Yamazaki, T.; Kubota, T.; Yajima, T. *Tetrahedron* **2014**, *70*, 6749−6756.

(4) (a) Said, M.; Maynau, D.; Malrieu, J. P.; Bach, M. A. G. *J. Am. Chem. Soc.* **1984**, *106*, 571−579.
(b) Sakai, S. *J. Phys. Chem. A* **2000**, *104*, 11615−11621.

(5) Shimizu, A.; Tobe, Y. *Angew. Chem., Int. Ed.* **2011**, *50*, 6906−6910.

(6) Trahanovsky, W. S.; Chou, C. H.; Fischer, D. R.; Gerstein, B. C. *J. Am. Chem. Soc.* **1988**, *110*, 6579−6581.

(7) Dolbier, W. R., Jr.; Matsui, K.; Michl, J.; Horak, D. V. *J. Am. Chem. Soc.* **1977**, *99*, 3876−3877.

(8) Johansson, E.; Skramstad, J. *J. Org. Chem.* **1981**, *46*, 3752−3754.

(9) (a) Gutowsky1, H. S.; Holm, C. H. *J. Chem. Phys.* **1956**, *25*, 1228−1235.
(b) Hesse, M.; Meier, H.; Zeeh, B. *Spectroscopic Methods in Organic Chemistry*, 2nd ed.; Thieme: Stuttgart, 2007.

(10) (a) Gingras, M.; Félix, G.; Peresutti, R. *Chem. Soc. Rev.* **2013**, *42*, 1007−1050.
(b) Rickhaus, M.; Mayor, M.; Juríčeka. M. *Chem. Soc. Rev.* **2016**, *45*, 1542−1556.

(11) Quinkert, G.; Wiersdorff, W. W.; Finke, M.; Opitz, K.; von der Haar, F. G. *Chem. Ber.* **1968**, *101*, 2302−2325.

(12) Minami, T.; Ito, S.; Nakano, M. *J. Phys. Chem. Lett.* **2013**, *4*, 2133−2137.

(13) Simizu, A.; Hirao, Y.; Matsumoto, K.; Kurata, H.; Kubo, T.; Uruichi. M.; Yakushi, K. *Chem. Commun.* **2012**, *48*, 5629−5631.

(14) Suzuki, T.; Sakano, Y.; Iwai, T.; Iwashita, S.; Miura, Y.; Katoono, R.; Kawai, H.; Fujiwara, K.; Tsuji, Y.; Fukushima, T. *Chem. - Eur. J.* **2013**, *19*, 117−123.

Chapter 3
Experimental investigation of the properties arising from the *o*- and *p*-quinodimethane skeletons

3-1. Introduction

This chapter focuses on the fundamental properties of electron-rich *p*-quinodimethane (*p*QDM) systems as well as *o*-quinodimethane (*o*QDM) systems. As introduced in **Chapter 1**, quinoidal, and especially quinodimethane-type, conjugated systems have intrinsic amphoteric redox ability and are therefore useful for the fabrication of electron-donor, electron-acceptor, and amphoteric materials. Interestingly, the most widely used quinoidal systems, such as 7,7,8,8-tetracyano-*p*-quinodimethane, are strong electron acceptors;[1] on the other hand, the number of quinoidal compounds with strong electron-donating ability is limited.

Recently, a number of polycyclic compounds with *p*QDM framework (**25**–**30**) have been reported to act as *p*-type (hole-transporting) semiconducting materials (Figure 3-1a).[2] In addition, a few *p*QDM derivatives (**31**–**33**) with ambipolar (electron and hole) transporting abilities have been described (Figure3-1b).[3] These reports demonstrate that quinodimethane systems are promising materials for organic electronics. On the other hand, whereas radical cationic species are known to play an important role as positive-charge carriers in *p*-type semiconducting layers, the fundamental properties of *p*QDM-based radical cations have not yet been clarified. The generation and preparation of *p*QDM-based radical cations in solution have been previously reported (**34**–**38**) (Figure 3-2);[4] however, to the best of my knowledge, there is no example of their isolation.

To date, the lack of diverse stable quinoidal systems has prevented a comparison between *p*QDMs and isomeric *o*QDMs, which would provide new topological information on these π-systems. In **Chapter 2**, the synthesis of a new stable electron-rich *o*QDM system, namely 5,8-dioxapentaphene derivative **11**, and its detailed properties were described. Herein, I have designed and synthesized 2,9-dibromo-7,14-dimesityl-5,12-dioxapentacene (**12**) as an electron-rich *p*QDM system, a structural isomer of *o*QDM **11**. The structural and electronic properties of **12** and **11** were compared to elucidate the fundamental properties arising from the *p*QDM and *o*QDM skeletons. Moreover, the isolation and X-ray structural analysis of $\mathbf{12}^{\bullet+}\bullet SbF_6^-$ is described.

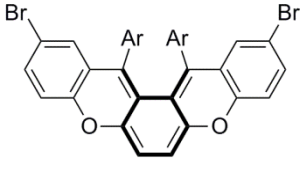

11
(Ar = mesityl)

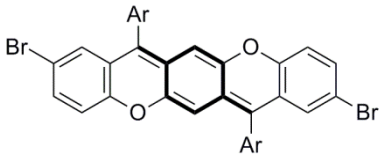

12
(Ar = mesityl)

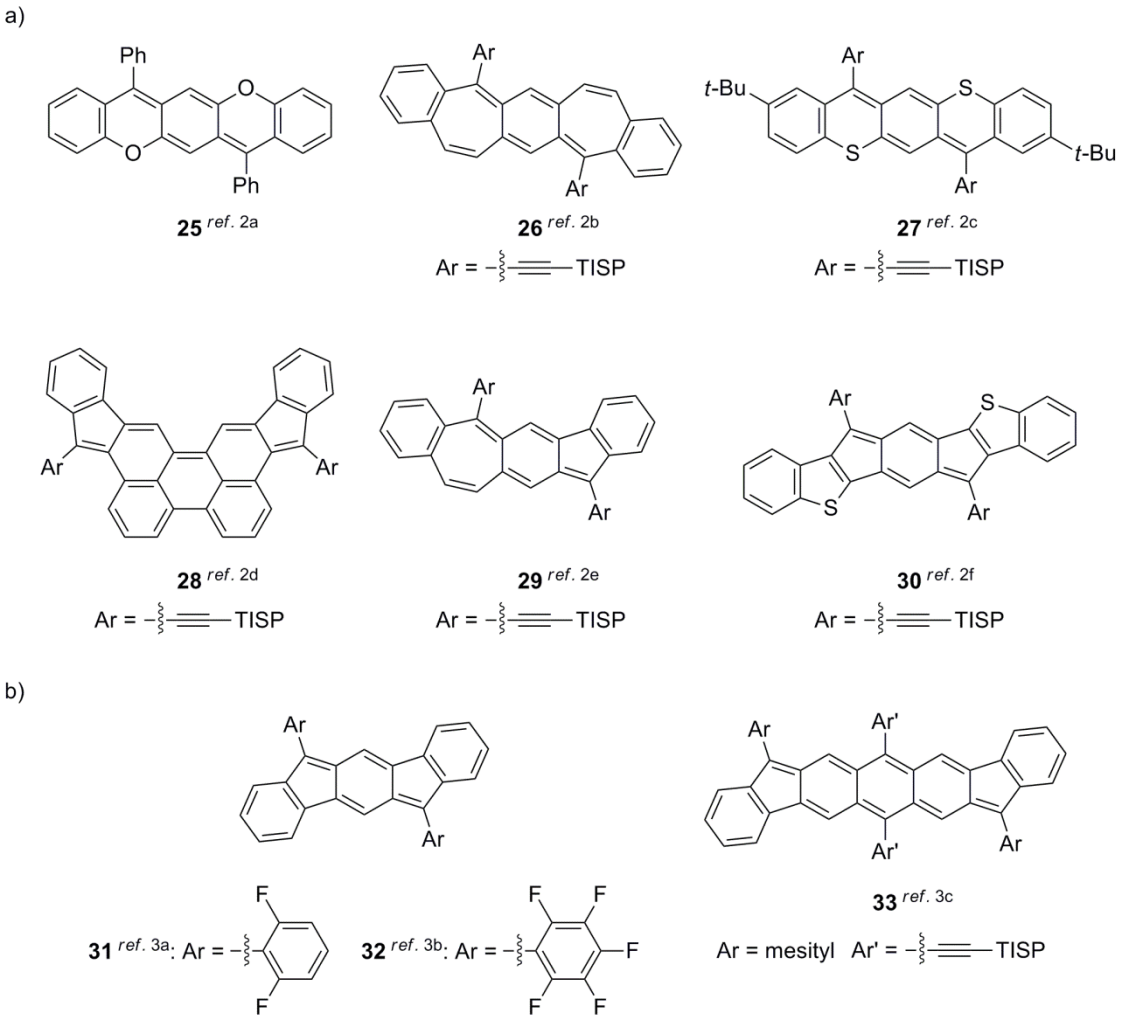

Figure 3-1. Reported *p*QDM derivatives with (a) *p*-type and (b) ambipolar semiconducting characteristics.

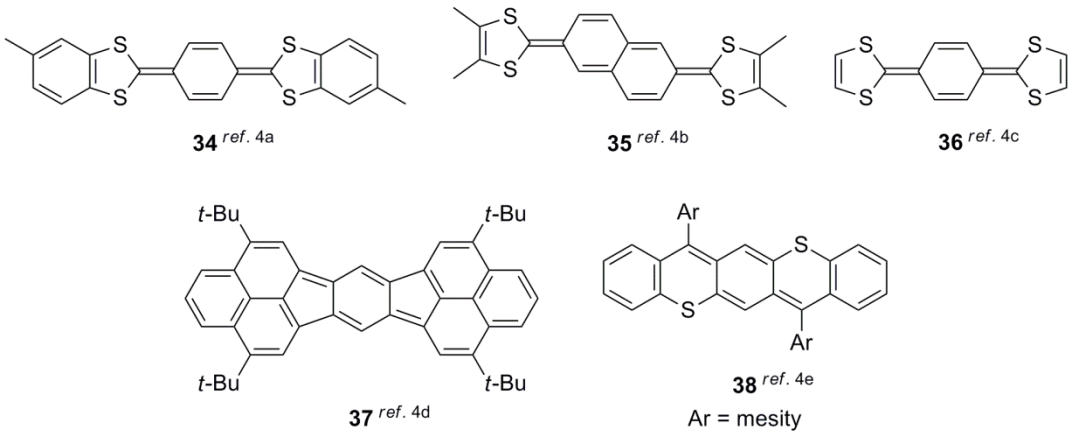

Figure 3-2. *p*QDM derivatives reported to form the radical cationic species.

3-2. Synthesis of 2,9-dibromo-7,14-dimesityl-5,12-dioxapentacene (12)

The previously reported synthesis of 5,12-dioxapentacene derivative **25** (Scheme 3-1)[2a] cannot be applied to the preparation of **12** because of the selectivity of the final annulation step. In addition, the electrophilic cyclization of carboxylic acid **20**, which selectively affords the angular product **21** (see **Chapter 2**), is obviously not applicable in this case. Thus, the linearly fused pentacene-like *p*QDM system **12** was constructed by a different procedure outlined in Scheme 3-2. The starting 2,5-dibromoterephtalic acid, prepared by a reported method,[5] was converted into the corresponding acid chloride **39** using $SOCl_2$. Next, the Friedel–Crafts reaction of **39** with 4-bromoanisole was performed using $AlCl_3$ under heating conditions, and dibenzoylbenzene **40** was obtained in 77% yield over two steps. The linearly fused framework was constructed by the intramolecular Ullmann-type coupling reaction using picolinic acid as a ligand, which afforded dione **41** in 65% yield. Finally, **41** was treated with mesityl Grignard reagent and then $SnCl_2$ to obtain *p*QDM system **12** as a deep red solid in 40% yield.

Scheme 3-1. Reported synthetic route of **25**.

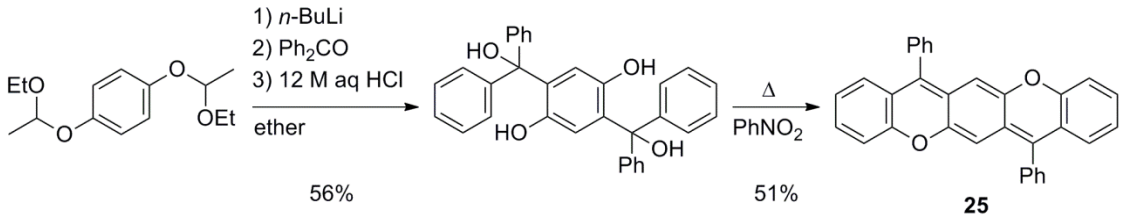

Scheme 3-2. Synthetic route of **12**.

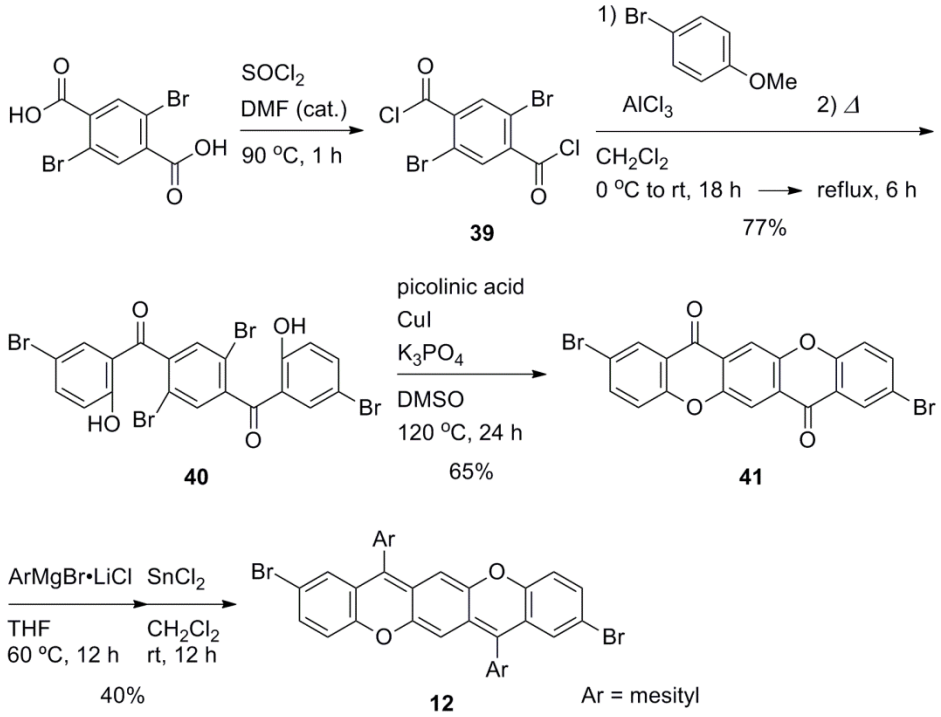

3-3. Molecular structure of 12

The detailed structure of **12** was determined by X-ray structural analysis (Figure 3-3 and Table 3-1). Recrystallization by slow diffusion of acetonitrile into the CH_2Cl_2 solution of **12** gave suitable crystals for X-ray analysis. Two crystallographically independent molecules (**A** and **B**) were observed in the unit cell, each having an inversion center. The dihedral angles of the mesityl groups were almost perpendicular to the backbone (89°). Whereas molecule **A** is almost planar (177.08° between rings *A*–*C*), **B** showed a slightly bent π-system (174.36°). As a result, differences were observed in the lengths of the corresponding bonds (Table 3-2). On the other hand, clear bond-length alternations around the central ring *C* were observed for both molecules **A** and **B**, indicating that **12** is a *p*QDM homologue.

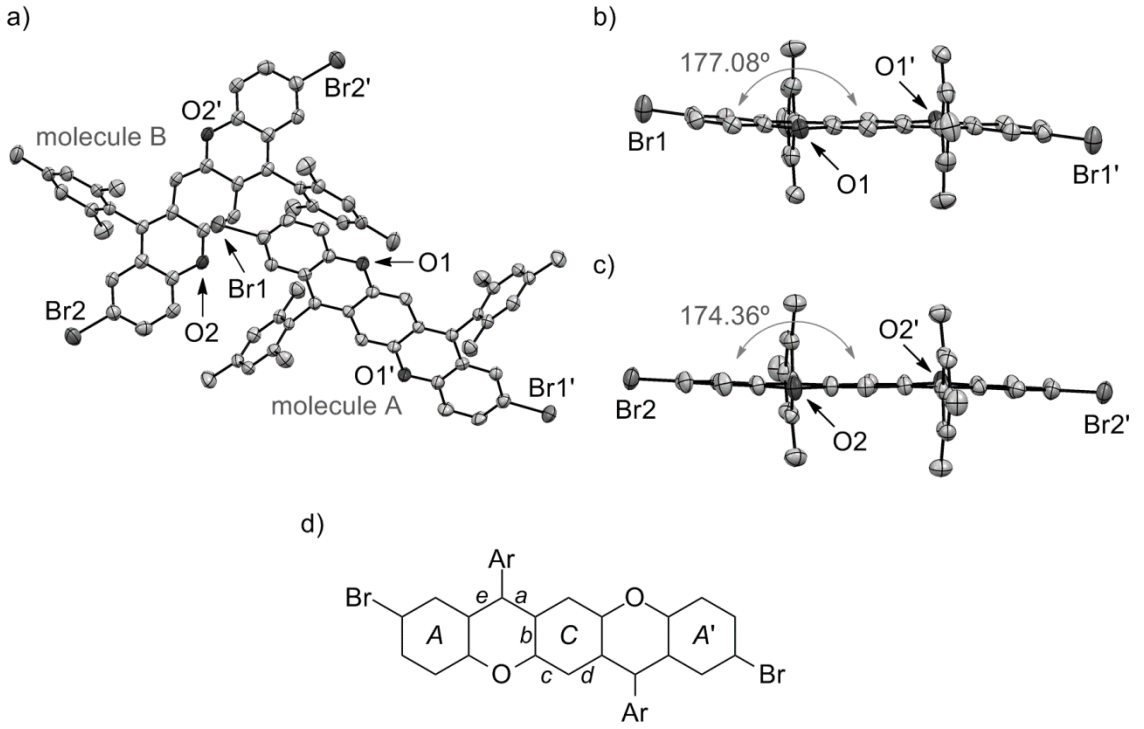

Figure 3-3. Crystal structures of **12**: (a) in the unit cell along *b* axis and side views along short axis of (b) molecule **A** and (c) **B**. Hydrogen atoms are omitted for clarity. Thermal ellipsoids set at 50%. Gray double-headed arrows and values indicate the dihedral angles between rings *A* and *C*. (d) Fused ring system of **12**. Italic symbols denote assigned names of the selected bond and ring positions.

Table 3-1. Crystallographic data of **12**.

Formula	$C_{38}H_{30}Br_2O_2$	D_{calc} / g cm^{-3}	1.457
Formula weight	678.45	F(000)	688.00
Crystal color,	red,	μ / cm^{-1}	26.61
morphology	block	No. of reflections	15719
Size / mm	0.30 × 0.10 × 0.02	measured	
Crystal system	triclinic	No. of unique	6879
Space group	P–1 (No. 2)	reflections	
a / Å	10.082(14)	No. of observed	4380
b / Å	11.400(16)	reflections	
c / Å	14.59(2)	No. of variables	409
α / degree	73.75(4)	Reflection	10.71
β / degree	83.98(5)	/ Parameter Ratio	
γ / degree	74.05(4)	R_1 [$I > 2.00\sigma(I)$]	0.0484
V / Å^3	1547(4)	R_w	0.0684
Z value	2	Goodness-of-fit	1.065
T / K	150		

Table 3-2. The selected bond lengths and HOMA values of **12** in the crystal state.

Bonds[a]	a[b]	b[b]	c[b]	d[b]	e[b]	HOMA[c,d]
molecule **A**	1.380(4)	1.443(4)	1.343(4)	1.438(5)	1.450(5)	0.351
molecule **B**	1.370(5)	1.461(4)	1.353(4)	1.430(5)	1.445(5)	0.285

[a] The crystal structures and assignment bond names are shown in Figure 3-3. [b] In Å unit. [c] Estimated using the bond lengths of *b*, *c*, and *d*.

[d] The HOMA values were estimated using the following equation:[6]

$$\mathrm{HOMA} = 1 - \frac{\alpha}{\mathrm{n}} \sum_{\mathrm{i}=1}^{\mathrm{n}} \left[R_{\mathrm{opt}} - R_{\mathrm{i}} \right]^2$$

where n and R_{i} are the number of bonds and the bond lengths taken into account, respectively, α is the empirical normalization constant for a fully delocalized (HOMA = 1)–localized (HOMA = 0) π-system, and R_{opt} is an estimated value for the precise bond length in a fully delocalized π-system; for conjugated cyclic hydrocarbons, α = 257.7 $\mathrm{Å}^{-1}$ and R_{opt} = 1.388 Å using the benzene–1,3,5-cyclohexatriene system as a standard.

Table 3-3. The selected bond lengths and HOMA value of **11** in the crystal state.

Bonds[a]	a[b]	b[b]	c[b]	d[b]	e[b]	HOMA[c,d]
	1.359(3)	1.458(3)	1.333(3)	1.436(3)	1.473(2)	
Bonds[a]	a'[b]	b'[b]	c'[b]	d'[b]	e'[b]	–0.198
	1.359(3)	1.461(3)	1.333(3)	1.485(3)	1.470(2)	

[a] Assignment bond names are shown in the following drawing. The crystal structure of **11** is shown in Figure 2-3 in **Chapter 2**. [b] In Å unit. [c] Estimated using the bond lengths of *b*, *c*, *d*, *b*', *c*', and *d*'. [d] See the above equation.

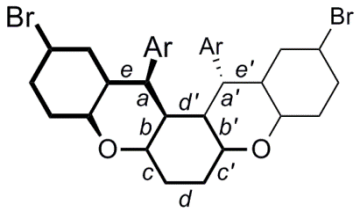

The crystal structure of **12** displays a decrease in the extent of bond-length alternations compared to that of *o*QDM system **11** (Table 3-3), as evidenced by the calculated HOMA (harmonic oscillator model of aromaticity) index.[6] HOMA is an aromaticity index using the normalized bond-length distribution based on the bond lengths of ideal benzene (perfectly delocalized structure) and 1,3,5-cyclohexatriene (the hypothetical Kekulé structure), where ideal benzene and 1,3,5-cyclohexatriene give HOMA values of 1 and 0, respectively. Thus, a HOMA closer to 1 indicates a higher aromaticity. The HOMA values of the central ring *C* were estimated to be –0.198 for **11**, and 0.351 and 0.285 for molecule **A** and **B** of **12**. These results suggest that the fused ring system in **12** had a more delocalized π-conjugation as compared to that in **11**. In fact, the calculated HOMO coefficient of the terminal rings in **12** was relatively larger than that in **11** (see Figure 3-5 in the next section).

The influence of the twisted structure of **11** on the nature of the π-conjugated system should be considered when comparing the properties of the *p*QDM system in **12** with those of the *o*QDM system in **11**. Hence, I examined the optimized structure of the parent compounds **24** and **42**, obtained by DFT calculation at the RB3LYP/6-31G** level (Table 3-4). A relatively small difference in bond lengths was observed between corresponding bonds, except for *d*' of **24**. In addition, the biradical characters of **12** and **42**, expressed as the occupation number of LUMO (*n*), were calculated to be 0.089 and 0.086 which are similar to those of **11** and **24**, respectively. These results suggest a small difference in the extent of bond-length alternations between the *p*QDM and *o*QDM moieties.

Table 3-4. Calculated values of the selected bond lengths and occupation number of LUMO (*n*) for **42**, **24**, **12**, and **11**.

Bonds[a]	*a*[c]	*b*[c]	*c*[c]	*d* (*d*')[c]	*e*[c]	*n*[d]
42 (Ar = H)[a,b]	1.373	1.453	1.361	1.437	1.436	0.0860705
24 (Ar = H)[a,b]	1.370	1.451	1.358	1.433	1.439	0.0901861
				(1.478)		
12[a,b]	1.383	1.451	1.362	1.438	1.451	0.0888799
11[a,b]	1.378	1.467	1.353	1.439	1.476	0.0913711
				(1.488)		

[a] Chemical structures and assignment bond names are shown in Figure 3-3 and Table 3-3. [b] All geometries were optimized by DFT calculation at the RB3LYP/6-31G** level. [c] In Å unit. [d] Calculated at the CASSCF(2,2)/6-31G level.

3-4. Electronic properties of 12

The UV–vis absorption spectrum of **12** in CH_2Cl_2 exhibited an intense and sharp absorption band (λ_{max} = 523 nm, ε_{max} = 1.06 × 10^5 M^{-1} cm^{-1}) in the 400–550 nm region with a defined vibrational structure (Figure 3-4). Form the peak separation values in the absorption band of **12** (λ_{peak} = 523, 487, and 456 nm), the vibrational energies were estimated to be 1413 and 1396 cm^{-1}, which can be attributed to the stretching vibrations of olefinic and/or aromatic C=C bonds ($\nu_{C=C} \approx$ 1500–1650 cm^{-1}). In addition, **12** produced a sharp fluorescence band in the 500–650 nm region (λ_{max} = 534 nm), which resembles a mirror image of the lowest energy absorption band. Thus, the photophysical properties of **12** are drastically different from those of *o*QDM system **11**, which showed a structureless broad absorption and no emission. The small Stokes shift ($\Delta\nu_{0-0}$ = 394 cm^{-1}) suggests a rigid π-backbone for **12** during the excitation and relaxation processes. In addition, the TD-DFT calculation for **12** revealed that the direction of the dipole moment of the HOMO–LUMO excitation was parallel to the C=C bonds in the *p*QDM moiety (Figure 3-5a–c). These results suggest that the HOMO–LUMO excitation of **12** can strongly couple with the asymmetric stretching vibrations of the *p*QDM moiety. On the other hand, the dipole moment of the HOMO–LUMO excitation of **11** was orthogonal to the long axis of the *o*QDM skeleton (Figure 3-5d–f). In addition, considering its flipping motion in solution, the π-backbone of **11** could be assumed to be flexible in the photophysical dynamics; namely, in the excited state, **11** could assume a more planar π-backbone due to the biradical nature of the S_1 state.[7] Presumably, these physical properties of **11** are responsible for the structureless broad absorption band and quenching of the radiative relaxation.[8]

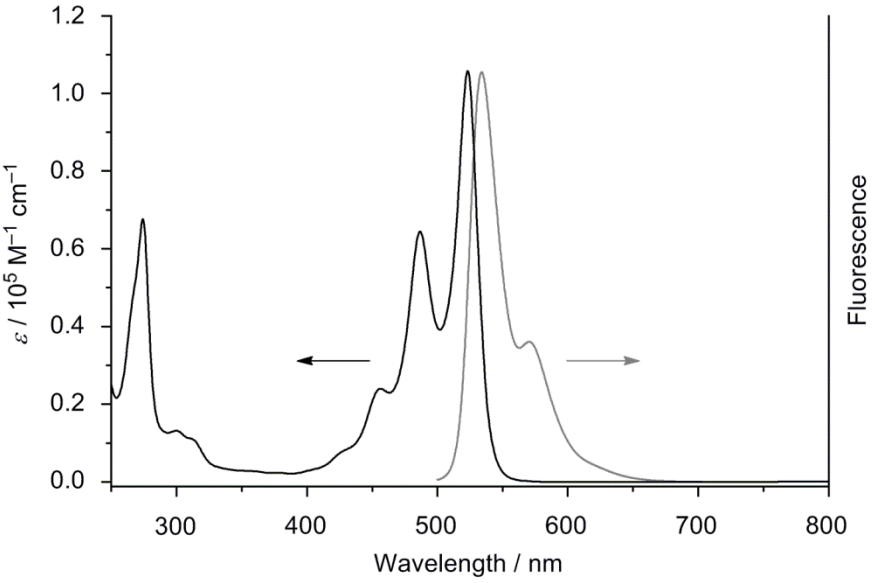

Figure 3-4. UV−vis absorption (black) and fluorescence (gray, λ_{ex} = 487 nm) spectra of **12** in CH_2Cl_2.

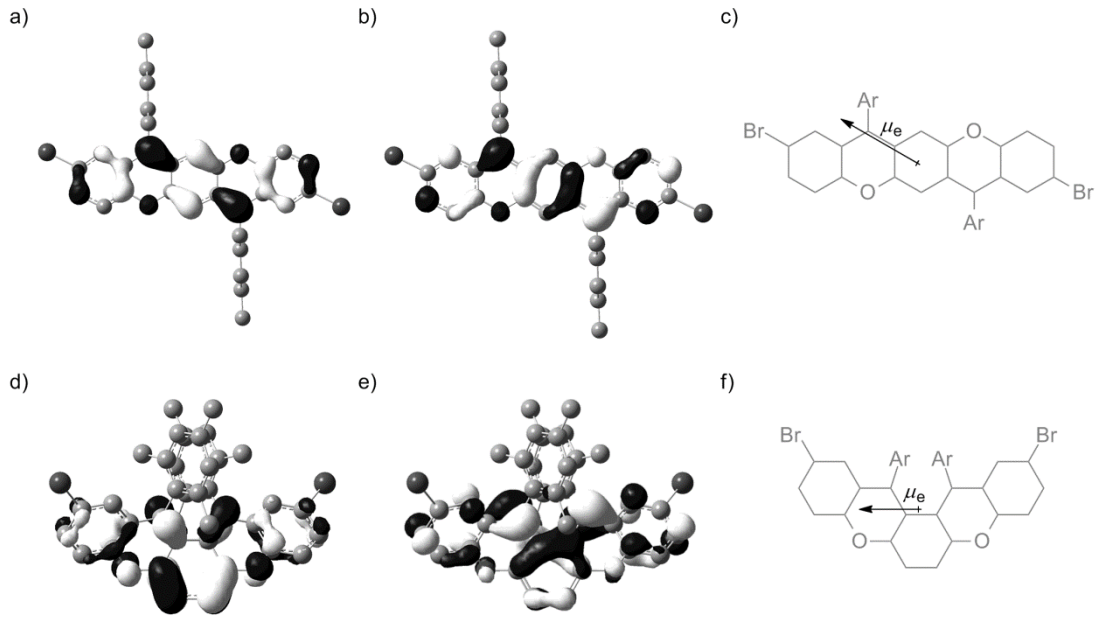

Figure 3-5. Calculated structures and orbitals (a) HOMO and (b) LUMO of **12**, and (d) HOMO and (e) LUMO of **11** (isovalue = 0.035) optimized at the DFT RB3LYP/6-31G** level. And, theoretical dipole moments of the HOMO–LUMO excitation of (c) **12** and (f) **11** calculated by TD-DFT at the RB3LYP/6-31G** level.

The cyclic voltammogram of **12** in CH_2Cl_2 (Figure 3-6) showed two reversible oxidation waves at +0.14 V and +0.69 V (vs Fc/Fc^+) and one irreversible reduction wave (–2.13 V at the peak). Thus, the cationic species of **12** are electrochemically stable, as those of **11**. In fact, the spectral change of **12** under the application of an external potential of +0.24 V (vs Fc/Fc^+) revealed a quantitative generation of the corresponding radical cationic species $\mathbf{12}^{\bullet+}$ (Figure 3-7 and Table 3-5). The first and second oxidation potentials of **12** are shifted to a higher voltage compared to the corresponding potentials of **11** (+0.07 V and +0.42 V, respectively), suggesting that the HOMO of **12** is stabilized by delocalization in the planar π-framework (Figure 3-5). On the other hand, the gap between the first and second oxidation potentials of **12** (ΔE_{ox1-2} = 0.55 V), which is involved by the onsite Coulomb repulsion between the two positive charges, was larger than that of **11** (ΔE_{ox1-2} = 0.35 V) in spite of the delocalized nature of the HOMO of **12**. These results can be explained by the reorientation of the molecules during oxidation processes (Figure 3-8). After the two-electron oxidation, $\mathbf{12}^{2+}$ has a the pentacene-like electronic structure contribution,[4e] whereas $\mathbf{11}^{2+}$ can form a pentaphene-like electronic structure. According to Clar's aromatic sextet theory, pentacene has only one sextet ring whereas the pentaphene skeleton has two sextet rings, indicating that the electronic structure of pentaphene is more stable. Thus, the pentaphene-like resonance hybrid stabilizes $\mathbf{11}^{2+}$ and facilitates the second oxidation.

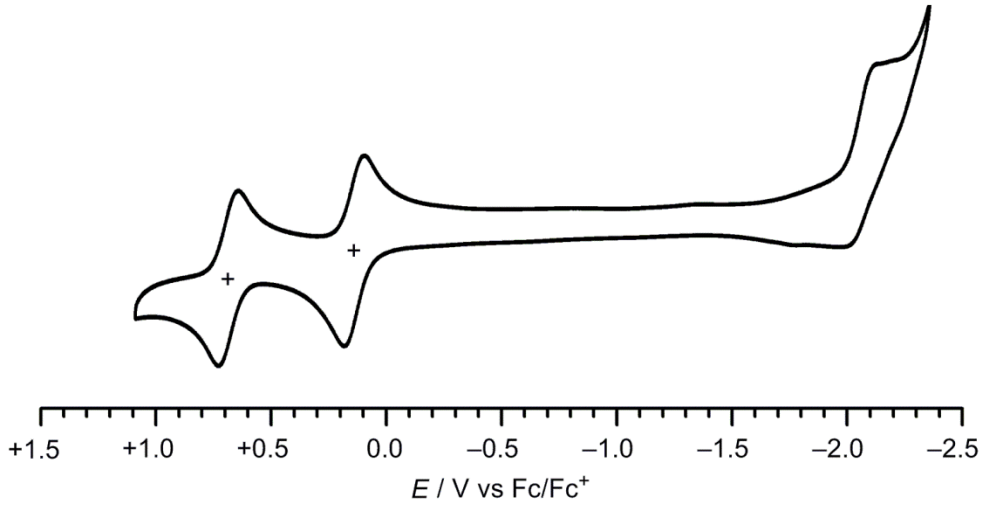

Figure 3-6. Cyclic voltammogram of **12** in CH_2Cl_2 containing 0.1 M *n*-Bu_4NPF_6 as a supporting electrolyte at a scan rate of 100 mV s^{-1}.

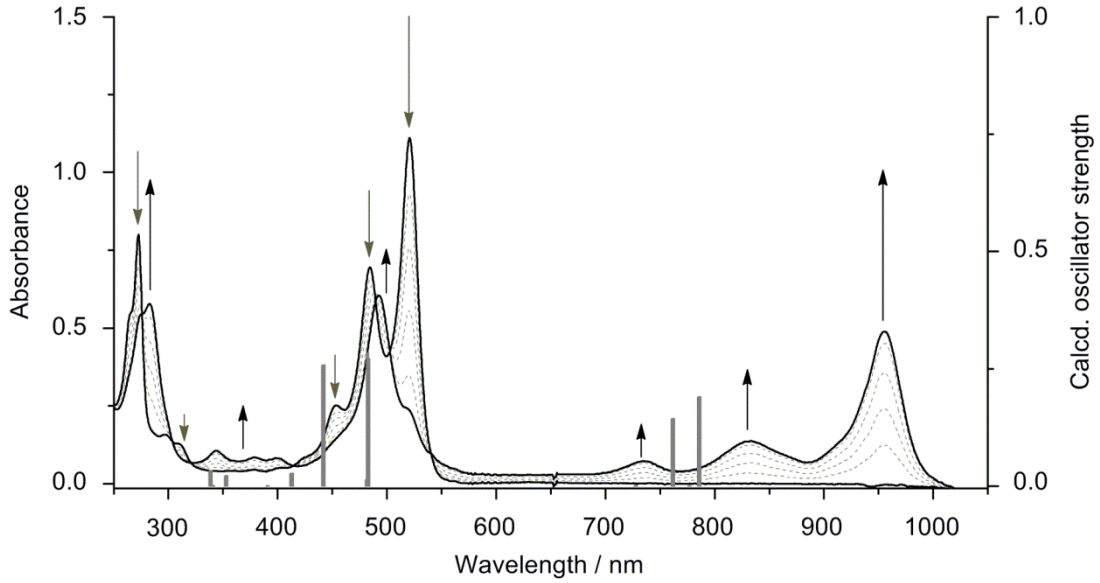

Figure 3-7. UV–vis spectral change of **12** during the electrochemical oxidation (at –0.24 V vs Fc/Fc^+) in CH_2Cl_2 containing 0.1 M *n*-Bu_4NPF_6. The dash lines show intermediate states. The gray solid bars show the theoretical values of excitation wavelengths and oscillator strengths for $\mathbf{12}^{\bullet+}$ calculated by TD-DFT at the UB3LYP/6-31G**//UB3LYP/6-31G** level. See also Table 3-5.

Table 3-5. Characteristic excitation energies of **12**$^{\bullet+}$ calculated by TD-DFT calculation at the UB3LYP/6-31G**//UB3LYP/6-31G** level.

Excited states	Transition energies / eV (Wavelength / nm)	Main CI coefficients	Oscillator strengths
1	1.5769 eV (786.25 nm)	SOMO(α)–LUMO(α) 0.89548	0.1895
3	1.6276 eV (761.78 nm)	HOMO(β)–SOMO(β) 0.89544	0.1438
10	2.5682 eV (482.77 nm)	HOMO–2(β)–SOMO(β) 0.91137	0.2706
14	2.8061 eV (441.83 nm)	HOMO–3(β)–SOMO(β) 0.84400	0.2582

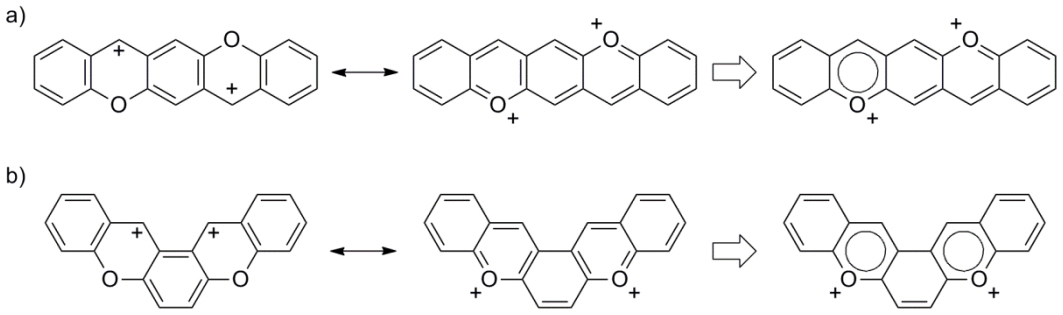

Figure 3-8. Resonance hybrid of the dicationic species in the π-backbones of (a) **12** and (b) **11**.

3-5. Properties and crystal structure of radical cation salt $12^{\bullet+}\bullet SbF_6^-$

Similarly to the preparation of $11^{\bullet+}\bullet SbF_6^-$, the chemical oxidation of **12** was carried out using tris(4-bromophenyl)aminium hexafluoroantimonate (TBPA•SbF_6) as an oxidant (Scheme 3-3), and the desired radical cation salt $12^{\bullet+}\bullet SbF_6^-$ was isolated as a dark red solid in 98% yield by reprecipitation from the CH_2Cl_2 solution using ether. The UV−vis−NIR spectrum of $12^{\bullet+}\bullet SbF_6^-$ in CH_2Cl_2 is consistent with that observed during the electrochemical oxidation (Figure 3-9). Moreover, $12^{\bullet+}\bullet SbF_6^-$ showed negligible spectral change after 1 day under aerated conditions at room temperature, indicating the high stability of $12^{\bullet+}\bullet SbF_6^-$. The lowest-energy absorption band in the 700–1000 nm region, which mainly ascribed to the SOMO−LUMO transition (Figure 3-7 and Table 3-5), showed a clear vibrational structure (λ_{peak} = 958, 835, and 737 nm) similar to the neutral species **12**. The vibrational energies were estimated to be 1578 and 1592 cm^{-1}, suggesting that the electronic structure of $12^{\bullet+}\bullet SbF_6^-$ has a *quasi-p*QDM nature.

Scheme 3-3. Synthesis of $12^{\bullet+}\bullet SbF_6^-$.

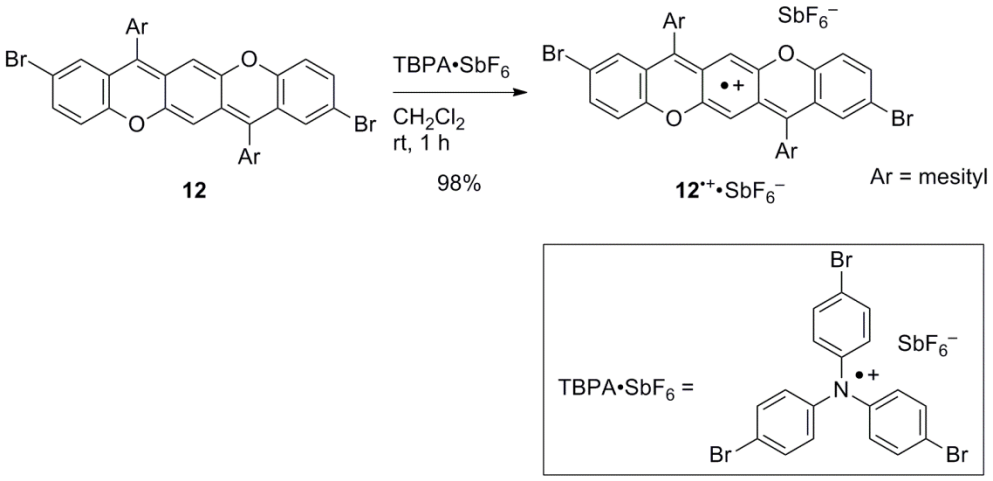

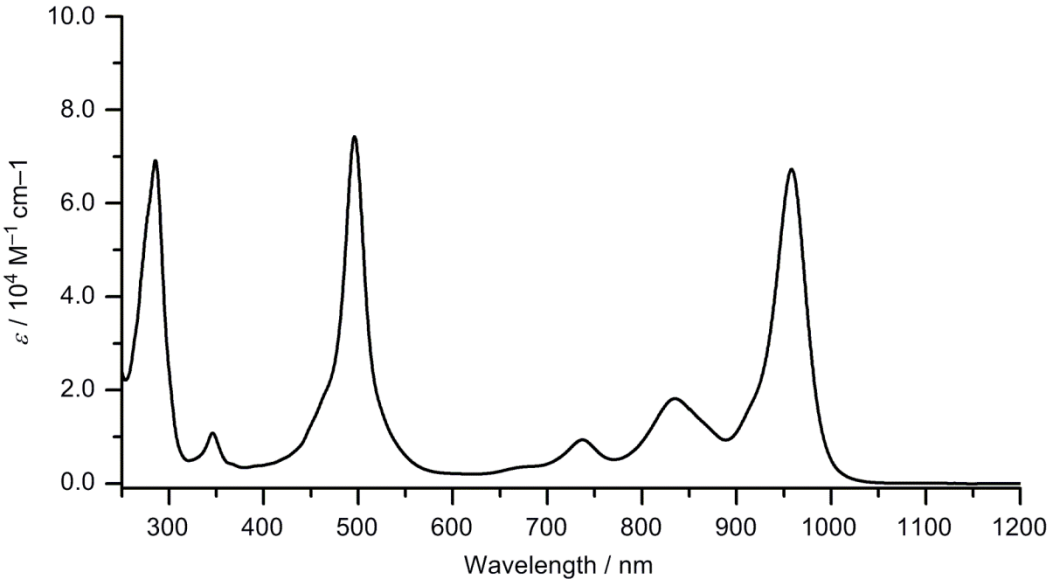

Figure 3-9. UV−vis−NIR absorption spectrum of $\mathbf{12}^{\bullet+}\bullet SbF_6^-$ in CH_2Cl_2.

The electron-spin resonance (ESR) spectrum of $\mathbf{12}^{\bullet+}\bullet SbF_6^-$ in degassed CH_2Cl_2 at room temperature showed multiple split lines with g = 2.0033 (Figure 3-10), which is drastically different from that of *o*QDM system $\mathbf{11}^{\bullet+}\bullet SbF_6^-$. Through trial and error, the observed ESR spectrum was reproduced by spectral simulation with the following hyperfine coupling constants for the four sets of ^{1}H nuclei (I = 1/2): $|a^{1H}|$ (×2) = 0.266 mT, $|a^{1H}|$ (×2) = 0.225 mT, $|a^{1H}|$ (×2) = 0.131 mT, and $|a^{1H}|$ (×4) = 0.046 mT. With the aid of the theoretical calculation of $\mathbf{12}^{\bullet+}$, the former three can be assigned to the two equivalent ^{1}H nuclei at the 6,13-, 3,10-, and 1,8-positions in the 5,12-dioxapentacene moiety, respectively (Figure 3-11). The remaining four ^{1}H nuclei can be attributed to one equivalent ^{1}H nuclei in the four *o*-methyl groups of the mesityl moieties owing to the through-space interactions based on the large spin densities at the 7- and 14-positions of the π-framework of $\mathbf{12}^{\bullet+}$. These results indicate that the electron spin of *p*QDM system $\mathbf{12}^{\bullet+}$ is delocalized over the entire π-conjugated system whereas in $\mathbf{11}^{\bullet+}$ the spin density is localized on the *o*QDM moiety.

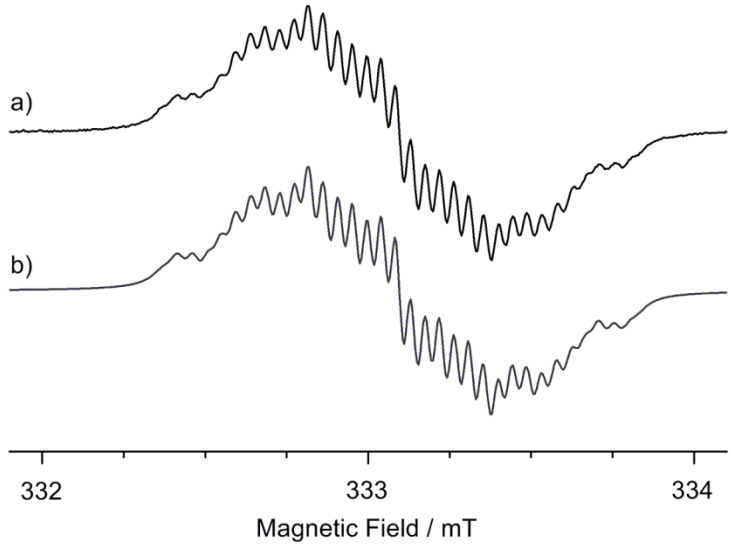

Figure 3-10. (a) Observed and (b) simulated ESR spectra of $\mathbf{12}^{\bullet+}\bullet SbF_6^-$ in CH_2Cl_2 at room temperature. Parameters for simulation: g = 2.0033, $|a^{1H}|$ (×2) = 0.266 mT, $|a^{1H}|$ (×2) = 0.225 mT, $|a^{1H}|$ (×2) = 0.131 mT, and $|a^{1H}|$ (×4) = 0.046 mT.

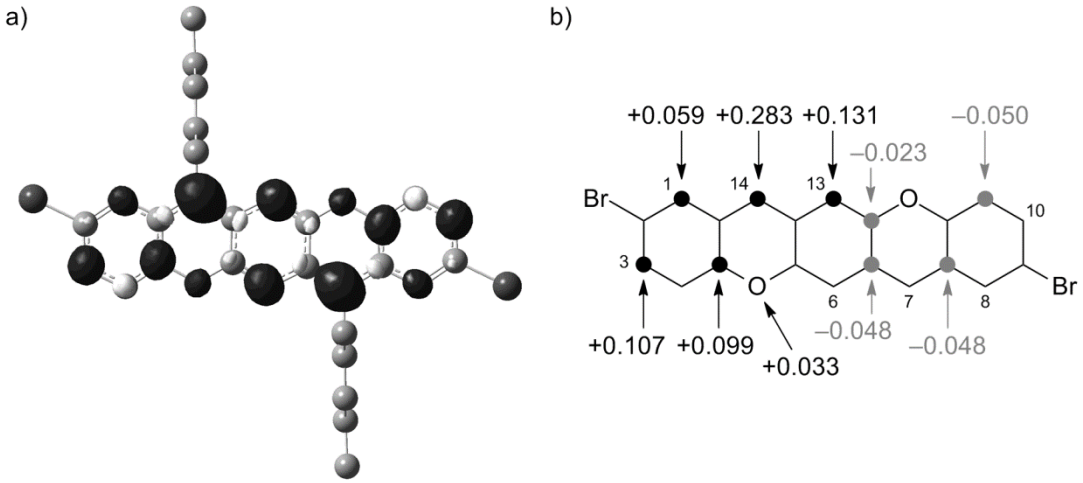

Figure 3-11. (a) Spin density map (isovalue = 0.002, black: positive spin, white: negative spin) and (b) values (mean value) of $\mathbf{12}^{\bullet+}$ optimized at the DFT UB3LYP/6-31G** level.

Moreover, the X-ray structural analysis of **12**$^{\bullet+}$•SbF_6^- was successfully performed (Figure 3-12 and Table 3-6). Recrystallization by slow diffusion of ether into the CH_2Cl_2 solution of **12**$^{\bullet+}$•SbF_6^- gave suitable crystals for X-ray analysis, in which the observed **12**$^{\bullet+}$•SbF_6^- contained two CH_2Cl_2 molecules as crystal solvent. The crystal structure of **12**$^{\bullet+}$•SbF_6^- has an inversion center and a form similar to that of the corresponding neutral species, i.e., a slightly bent (175.48°) π-framework and 87°-twisting mesityl groups. Remaining but reduced bond-length alternations around the central ring *C* were observed (Table 3-7), which is consistent with the NIR absorption band with the vibrational structure. In addition, the HOMA value of the central ring *C* was estimated to be 0.668, and the length of the bond *e* (1.414(4) Å) was close to the aromatic value, clearly indicating delocalization of the π-conjugated system of **12**$^{\bullet+}$ and thus confirming the results of the ESR study.

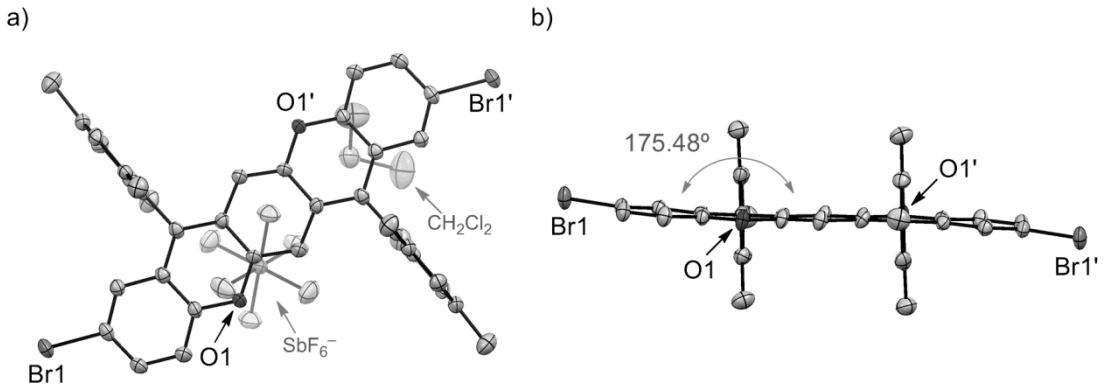

Figure 3-12. Crystal structure of **12**$^{\bullet+}$•SbF_6^-: (a) Top view and (b) side views along short axis of **12**$^{\bullet+}$. Hydrogen atoms are omitted for clarity. Thermal ellipsoids set at 50%. In (b), the counter anion and crystal solvents are omitted for clarity. The gray double-headed arrow and the value indicate the dihedral angle between rings *A* and *C*.

Table 3-6. Crystallographic data of **12**$^{\bullet+}$•SbF_6^-.

Formula	$C_{38}H_{30}Br_2O_2$•SbF_6•$(CH_2Cl_2)_2$	D_{calc} / g cm^{-3}	1.760
Formula weight	1084.07	F(000)	533.00
Crystal color,	green,	μ / cm^{-1}	29.56
morphology	platelet	No. of reflections	7698
Size / mm	0.20 × 0.08 × 0.02	measured	
Crystal system	triclinic	No. of unique	4022
Space group	P–1 (No. 2)	reflections	
a / Å	9.057(11)	No. of observed	3038
b / Å	9.138(13)	reflections	
c / Å	13.85(2)	No. of variables	267
α / degree	79.61(5)	Reflection	11.38
β / degree	77.17(5)	/ Parameter Ratio	
γ / degree	66.90(4)	R_1 [$I > 2.00\sigma(I)$]	0.0330
V / Å^3	1023(2)	R_w	0.0435
Z value	1	Goodness-of-fit	0.834
T / K	150		

Table 3-7. The selected bond lengths and HOMA values of **12**$^{\bullet+}$•SbF_6^-.

Bonds[a]	a[b]	b[b]	c[b]	d[b]	e[b]	HOMA[c,d]
	1.386(4)	1.432(4)	1.358(4)	1.420(4)	1.414(4)	0.668

[a] Assignment bond names are shown in Figure 3-3. [b] In Å unit. [c] Estimated using the bond lengths of *b*, *c*, and *d*. [d] The equation for HOMA are shown in Table 3-2.

3-6. Experimental section

General Methods

- Melting points were taken on a Yanaco MP J-3 and were uncorrected.
- ^{1}H and ^{13}C NMR spectra were recorded on a Bruker Avance III 400 spectrometer (400 MHz for ^{1}H and 100 MHz for ^{13}C).

  # Chemical Shifts were reported in parts per million downfield for tetramethylsilane as an internal (for chloroform-*d*) and external (for sulfuric acid-d_2, using the value in $CDCl_3$) standard or relative to solvent signal (chloroform: δ = 7.26 for ^{1}H NMR and δ = 77.0 ppm for ^{13}C NMR) as internal standards, and all coupling constants are reported in Hz (Multiplicity: s = singlet; d = doublet).
- IR spectra were recorded on a JASCO FT/IR-4600 spectrometer.
- DART-TOF and ESI-TOF mass spectra were recorded on a JEOL AccuTOF spectrometer.
- Elemental analyses were obtained from the Analytical Center in Osaka City University, using a Fisons EA1108 and a J-Science JM10.
- X-ray data were collected by a Rigaku Saturn 724 CCD system with graphite monochromated Mo-Kα radiation.
- Absorption spectra were recorded on a Shimadzu UV-2550 spectrometer and a JASCO V670 spectrometer.
- Redox potential was measured using an ALS Electrochemical analyzer MODEL 610A in a conventional three-electrode cell equipped with a glassy carbon as a working electrode and a platinum wire as a counter electrode with a SCE reference electrode. The measurement was carried out at a scan rate 100 mV s^{-1} in dichloromethane containing 0.1 M tetra-*n*-butylammonium hexafluorophosphate as a supporting electrolyte. The redox potentials were finally corrected by the ferrocene/ferrocenium (Fc/Fc^{+}) couple.
- Absorption spectra of the oxidation species for **12** were recorded on an Ocean Optics HR4000 spectrometer using a 1 mm width cell equipped with a fine mesh platinum as a working electrode, a platinum wire as a counter electrode, and a SCE reference electrode. The external potential of –0.20 V vs Fc/Fc^{+} (+0.41 V vs SCE) was applied using a Bi-Potentiostat ALS/DY2323 for the electrochemical oxidation of **12** in dichloromethane containing 0.1 M tetra-*n*-butylammonium hexafluorophosphate.
- ESR spectrum of $\mathbf{12}^{\bullet+}\bullet SbF_6^{-}$ was recorded on a Bruker ELEXSYS E500 spectrometer.

Materials

- Merck gel 60 (63–200 mesh) or Kanto Chemical Silica gel 60 (100–200 mesh) were used for column chromatography.
- The progress of reactions was monitored using thin-layer chromatography using Merck TLC silica gel 60 F254.
- All commercially available compounds were reagent grade and used without further purification.
- 2,5-Dibromoterephtalic acid was prepared by the reported method.[5]
- Dehydrate dimethyl sulfoxide was purchased.
- Tetrahydrofuran was dried and distilled over sodium.
- Dichloromethane was dried and distilled over calcium hydride.

Synthetic procedures and compounds data

1,4-Dibromo-2,5-di(5-bromo-2-hydroxybenzoyl)benzene (40)

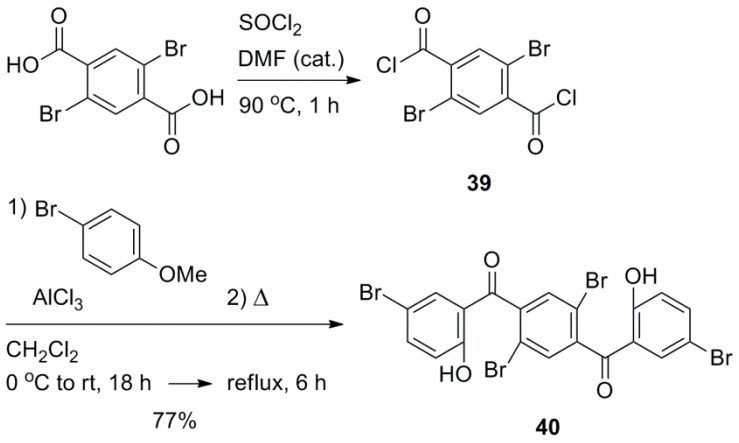

2,5-Dibromoterephtalic acid (4.56 g, 15.0 mmol) and one drop of DMF were placed in a 300 mL two-necked round bottom flask with thionyl chloride (65 mL). The suspension was refluxed at 90 °C for 1 h under an N_2 atmosphere. After cooling to rt, an excess amount of thionyl chloride was removed under reduced pressure to obtain the corresponding acid chloride **39** as a pale-brown crude solid. This crude compound was used in the next step without further purification.

After refilling the reaction equipment with N_2, the obtained crude **39** was dissolved in dichloromethane (100 mL), and the mixture was cooled at 0 °C. To this solution was added finely-grounded $AlCl_3$ by a portion. The resulting mixture was stirred at 0 °C for 30 min and then warmed up to rt. After stirring for 30 min at rt, the mixture was cooled again to 0 °C, and then a solution of 4-bromoanisole (11.2 mmol 60.0 mmol) in dichloromethane (50 mL) was added slowly. The resulting mixture was allowed to warm up to rt. After stirring for 18 h at rt, the mixture was refluxed at 90 °C for additional 6 h. After cooling to rt, the mixture was poured in to an excess amount of 4 M aq HCl cooled at 0 °C. The resulting precipitate was collected by filtration, and the residue was washed with water and ethanol to obtain **40** (7.34 g, 77%) as a pale yellow powder.

40: $C_{20}H_{10}Br_4O_4$; MW 633.91; mp 276–277 °C; ^{1}H NMR (400 MHz, $CDCl_3$, δ): 11.63 (s, 2H), 7.66 (dd, J = 8.9 and 2.4 Hz, 2H), 7.63 (s, 2H), 7.35 (d, J = 2.4 Hz, 2H), 7.03 (d, J = 8.9 Hz, 2H); ^{13}C NMR (100 MHz, $CDCl_3$, δ): 197.65, 162.42, 141.63, 140.76, 134.79, 132.80, 120.88, 119.67, 118.51, 111.22; IR (KBr) ν_{max} (cm^{-1}): 3147 (br), 3086, 1762, 1735, 1678, 1630, 1607, 1568, 1463, 1348, 1285, 1231, 1207, 1154, 1065, 945, 893, 827, 733, 645, 521; MS (DART-TOF$^-$) m/z: 630.9, 632.9, and 634.9 [M – H$^-$]; Anal Calcd for $C_{20}H_{10}Br_4O_4$: C, 37.89; H, 1.59. Found: C, 38.16; H, 1.63.

2,9-Dibromo-7,14-dihydro-5,12-dioxapentacene-7,14-dione (41)

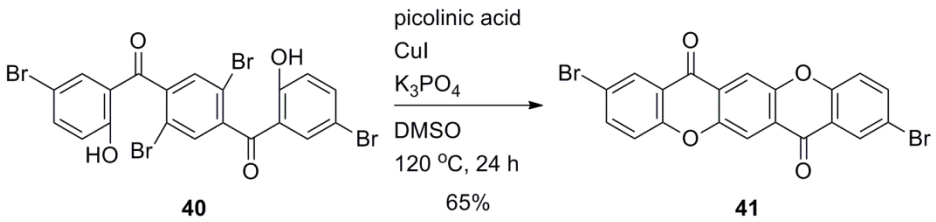

Picolinic acid (118 mg, 0.96 mmol), CuI (91 mg, 0.48 mmol), and K_3PO_4 (1.36 g, 6.41 mmol) were placed in a 50 mL two-neck round bottom flask with DMSO (16 mL). The mixture was degassed by an N_2-bubbling for 5 min and heated at 50 °C for 30 min. To this suspension after cooling to rt, 1,4-dibromo-2,5-di(5-bromo-2-hydroxybenzoyl)benzene (**41**) (1.01 g, 1.60 mmol) was added using DMSO (8 mL) as a rinse solvent. The mixture was heated at 120 °C for 24 h under an N_2 atmosphere. After cooling to rt, the mixture was poured in to an excess amount of 4 M aq HCl. The resulting precipitate was collected by filtration, and the residue was washed with ethanol. The obtained crude product was completely dissolved in 18 M H_2SO_4, and then the deep-red solution was added dropwise into ice-cooled water. The generated precipitate was collected by filtration, and the residue was washed with water and ethanol to obtain **41** (490 mg, 65%) as a brownish yellow powder.

41: $C_{20}H_8Br_2O_4$; MW 472.08; mp > 300 °C; ^{1}H NMR (400 MHz, D_2SO_4, δ): 8.65 (s, 2H), 8.11 (d, J = 1.8 Hz, 2H), 7.81 (dd, J = 9.3 and 1.8 Hz, 2H), 7.35 (d, J = 9.3 Hz, 2H); ^{13}C NMR (100 MHz, D_2SO_4, δ): 177.51, 159.74, 150.91, 149.15, 127.46, 122.70, 121.43, 121.04, 118.08, 114.65; IR (KBr) ν_{max} (cm^{-1}): 3086, 1664, 1602, 1463, 1447, 1339, 1269, 1205, 1127, 913, 823, 787, 662, 531, 418; MS (DART-TOF$^+$) m/z: 471.0, 472.0, and 474.0 [M + H$^+$]; Anal Calcd for $C_{20}H_8Br_2O_4$: C, 50.88; H, 1.71. Found: C, 50.72; H, 1.84.

2,9-Dibromo-7,14-dimesityl-5,12-dioxapentacene (12)

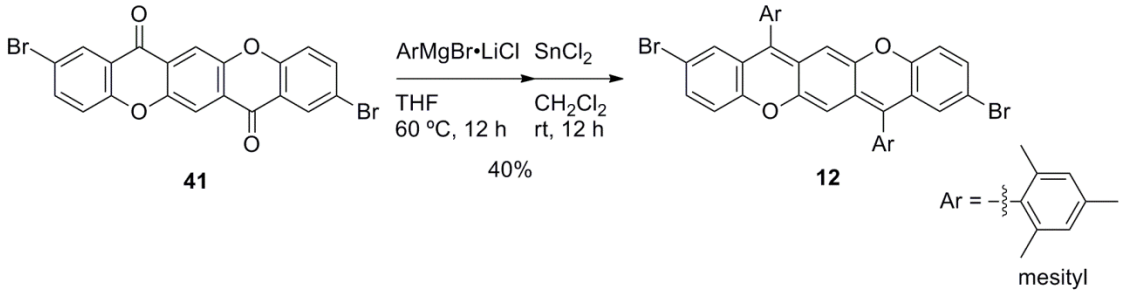

To prepare mesityl Grignard reagent, in a 10 mL two-necked round bottom flask under an N_2 atmosphere, the solution of 2-bromomesitylene (1.19 g, 6.00 mmol) in THF (3 mL) was added slowly to the suspension of anhydrous LiCl (212 mg, 5.00 mmol) and Mg turnings (120 mg, 5.00 mmol) in THF (3 mL) at 40 °C, and the mixture was stirred for 1 h.

In another 30 mL two-necked round bottom flask under an N_2 atmosphere, 2,9-dibromo-7,14-dihydro-5,12-dioxapentacene-7,14-dione (**41**) (472 mg, 1.00 mmol) was placed with THF (10 mL) at 60 °C. To the suspension of **41** was added dropwise slowly the prepared mesityl Grignard reagent, and then the mixture was stirred for 12 h. After cooling to rt, 4 M aq HCl was added to quench the reaction. The aqueous layer was extracted with dichloromethane, and the combined organic layer was dried over Na_2SO_4. A removal of the solvent under reduced pressure gave the crude mesitylated diol.

The obtained crude diol was dissolved in dichloromethane (60 mL), and the mixture was degassed by an N_2-bubbling for 5 min. After the degassing, one drop of 4 M aq HCl and anhydrous $SnCl_2$ (1.14 g, 6.00 mmol) was added, and then the mixture was stirred at rt for 12 h. The resulting mixture was passed through Celite® to remove the excess amount of $SnCl_2$, and then the filtrate was concentrated under reduced pressure. The residue was purified by silica gel column chromatography using *n*-hexane–dichloromethane (1:1 v/v) as an eluent, and then the obtained product was washed with ethanol to obtain **12** (274 mg, 40 %) as a deep red solid. Single crystals of **12** suitable for X-ray analysis were obtained by a liquid diffusion of acetonitrile with a solution of **12** in CH_2Cl_2.

12: $C_{38}H_{30}Br_2O_2$; MW 678.45; mp 255–260 °C (decomp); ^{1}H NMR (400 MHz, $CDCl_3$, δ): 7.06 (dd, J = 8.6 and 2.3 Hz, 2H), 7.00 (s, 4H), 6.63 (d, J = 8.6 Hz, 2H), 6.48 (d, J = 2.3 Hz, 2H), 5.41 (s, 2H), 2.08 (s, 12H), 1.86 (s, 6H); ^{13}C NMR (100 MHz, $CDCl_3$, δ): 152.20, 150.84, 137.85, 137.01, 130.46, 129.77, 128.74, 128.09, 126.03, 125.80, 124.60, 116.54, 116.32, 100.00, 21.17, 19.69; IR (KBr) ν_{max} (cm^{-1}): 2969, 2916, 2855, 1577, 1555, 1468, 1407, 1377, 1302, 1260, 1212, 1190, 1165, 1072, 966, 914, 849, 808, 761, 664, 581; MS (DART-TOF$^+$) *m*/*z*: 677.2, 679.2, and 681.2 [M + H$^+$]; Anal Calcd for $C_{38}H_{30}Br_2O_2$: C, 67.27; H, 4.46. Found: C, 67.50; H, 4.66.

Radical cation hexafluoroantimonate salt $12^{\bullet+}\bullet SbF_6^-$

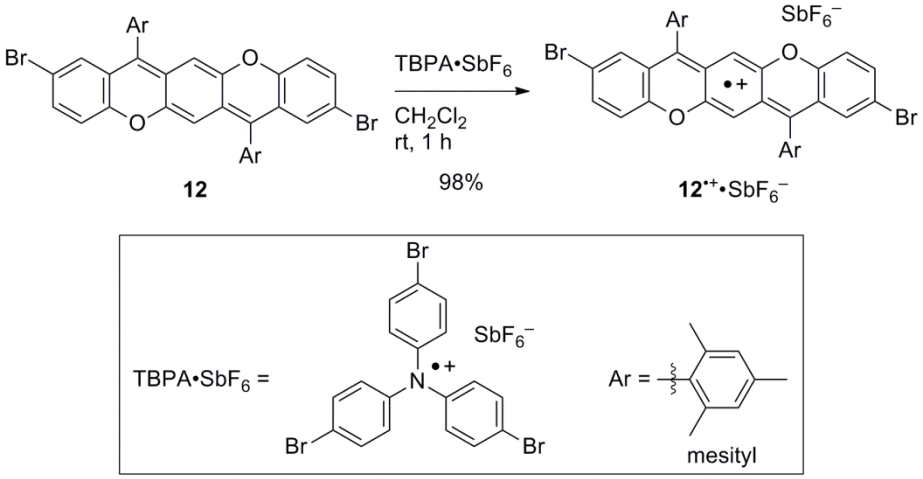

In a glove box filled with argon, 2,9-dibromo-7,14-dimesityl-5,12-dioxapentacene (**12**) (21.4 mg, 0.0315 mmol) was dissolved in dichloromethane (3 mL). To this solution was added a solution of tris(4-bromophenyl)aminium hexafluoroantimonate (TBPA•SbF_6, 22.0 mg, 0.0307 mmol) in dichloromethane at rt, and the mixture was stirred for 1 h. The resulting mixture was evaporated under reduced pressure. The residue was dissolved in a minimum amount of dichloromethane, and then ether was added slowly. The generated precipitate was collected by filtration to obtain $\mathbf{12}^{\bullet+}\bullet SbF_6^-$ (28.8 mg obtained as $\mathbf{12}^{\bullet+}\bullet SbF_6^-\bullet(CH_2Cl_2)_{0.2}$, 98%) as a dark-red solid.

$\mathbf{12}^{\bullet+}\bullet SbF_6^-$: $C_{38}H_{30}Br_2F_6O_2Sb$; MW 914.20; mp 250–255 °C (decomp); IR (KBr) ν_{max} (cm^{-1}): 3082, 2973, 2919, 2859, 1609, 1553, 1482, 1434, 1390, 1333, 1275, 1173, 1139, 1067, 970, 918, 822, 766, 660, 580, 547; MS (ESI-TOF$^+$) *m*/*z*: 676.1, 678.1, and 680.1 [$C_{38}H_{30}Br_2O_2^+$], (ESI-TOF$^-$) *m*/*z*: 234.9 and 236.9 [SbF_6^-]; Anal Calcd for $(C_{38}H_{30}Br_2O_2\bullet SbF_6)\bullet(CH_2Cl_2)_{0.2}$: C, 49.27; H, 3.29. Found: C, 49.11; H, 3.51.

3-7. References

(1) (a) Martin, N.; Segura, J. L.; Seoane, C. *J. Mater. Chem.* **1997**, *7*, 1661−1676.
(b) Hünig, S.; Herberth, E. *Chem. Rev.* **2004**, *104*, 5535−5563.
(c) Saito, G.; Yoshida, Y. *Bull. Chem. Soc. Jpn.* **2007**, *80*, 1−137.
(d) Mori, T.; Yanai, N.; Osaka, I.; Takimiya, K. *Org. Lett.* **2014**, *16*, 1334−1337.

(2) (a) Kalb, W. L.; Stassen, A. F.; Batlogg, B.; Berens, U.; Schmidhalter, B.; Bienewald, F.; Hafner, A.; Wagner, T. *J. Appl. Phys.* **2009**, *105*, 043705.
(b) Yang, X.; Liu, D.; Miao, Q. *Angew. Chem., Int. Ed.* **2014**, *53*, 6786−6790.
(c) Qun Ye, Q.; Jingjing Chang, J.; Xueliang Shi, X.; Gaole Dai, G.; Wenhua Zhang, W.; Huang, K. -W.; Chi, C. *Org. Lett.* **2014**, *16*, 3966−3969.
(d) Sbargoud, K.; Mamada, M.; Marrot, J.; Tokito, S.; Yassar, A.; Frigoli, M. *Chem. Sci.* **2015**, *6*, 3402−3409.
(e) Yang, X.; Shi, X.; Aratani, N.; Gonçalves, T. P.; Huang, K. -W.; Yamada, H.; Chi, C.; Miao, Q. *Chem. Sci.* **2016**, *7*, 6176−6181.
(f) Marshall, J. L.; Uchida, K.; Frederickson, C. K.; Schütt, C.; Zeidell, A. M.; Goetz, K. P.; Finn, T. W.; Jarolimek, K.; Zakharov, L. N.; Risko, C.; Herges, R.; Jurchescu, O. D.; Haley, M. M. *Chem. Sci.* **2016**, *7*, 5547−5558.

(3) (a) Nishida, J.; Tsukaguchi, S.; Yamashita, Y. *Chem. - Eur. J.* **2012**, *18*, 8964−8970.
(b) Chase, D. T.; Fix, A. G.; Kang, S. J.; Rose, B. D.; Weber, C. D.; Zhong, Y.; Zakharov, L. N.; Lonergan, M. C.; Nuckolls, C.; Haley, M. M. *J. Am. Chem. Soc.* **2012**, *134*, 10349−10352.
(c) Rudebusch, G. E.; Zafra, J. L.; Jorner, K.; Fukuda, K.; Marshall, J. L.; Arrechea-Marcos, I.; Espejo, G. L.; Ortiz, R. P.; Gómez-García, C. J.; Zakharov, L. N.; Nakano, M.; Ottosson, H.; Casado, J.; Haley, M. M. *Nat. Chem.* **2016**, *8*, 753−759.

(4) (a) Ueno, Y.; Nakayama, A.; Okawara, M. *J. Chem. Soc., Chem. Commun.* **1978**, 74−75.
(b) Bryce, M. R. *J. Chem. Soc., Perkin Trans. 1* **1985**, 1675−1679.
(c) Yamashita, Y.; Kobayashi, Y.; Miyashi, T. *Angew. Chem., Int. Ed. Engl.* **1989**, *28*, 1052−1053.
(d) Ohashi, K.; Kubo, T.; Masui, T.; Yamamoto, K.; Nakasuji, K.; Takui, T.; Kai, Y.; Murata, I. *J. Am. Chem. Soc.* **1998**, *120*, 2018−2027.

(5) Yao, Y.; Tour, J. M. *Macromolecules* **1999**, *32*, 2455−2461.

(6) (a) Krygowski, T. M.; Cyrański, M. *Tetrahedron* **1996**, *52*, 1713−1722.
(b) Gleiter, R.; Haberhauer, G.; Hoffmann, R. Aromaticity and Other Conjugation Effects; Wiley−VCH: Weinheim, 2012.

(7) (a) Flynn, C. R.; Michl, J. *J. Am. Chem. Soc.* **1974**, *96*, 3280−3288.
(b) Migirdicyan, E.; Baudet, J. *J. Am. Chem. Soc.* **1975**, *97*, 7400−7404.

(8) Nijegorodov, N. I.; Downey, W. S. *J. Phys. Chem.* **1994**, *98*, 5639−5643.

Chapter 4
Synthesis and properties of functionalized 5,8-dioxapentaphene systems

4-1. Introduction

The investigations in **Chapter 2** and **Chapter 3** revealed the attractive properties of 5,8-dioxapentaphene (DOP) derivative **11**, namely the wide absorption band in the visible region and the amphoteric redox ability, which arise from its unique electronic and molecular structure and were not observed for the *p*-quinodimethane system **12**. In addition, I have developed the simple, short, and multigram-scale synthetic route to **11**, which does not involve any cross-coupling reactions, such as the Suzuki-Miyaura reaction. Thus, the two bromine atoms of **11** are preserved and can be used to extend the π-conjugation of the DOP core through cross-coupling reactions.

The unique properties and easy accessibility of the DOP framework encouraged the synthesis of functionalized DOP derivatives for the development of novel fused *o*-quinodimethane (*o*QDM) systems (Figure 4-1). Here, 3,10-dibromo-DOP **14**, a positional isomer of **11**, was designed, in which the two bromine atoms on the peripheral benzene rings are located at the *para*-position of the *o*QDM skeleton. The *o*QDM moiety of **14** is expected to strongly conjugate with functional groups introduced in the DOP framework by substitution of the bromine atoms. In this chapter, dicyano derivatives **13** and **15** were synthesized, and the substituent effect on their properties was investigated. Moreover, π-extension of the DOP system was performed to obtain **16** through the further bromination of **15**.

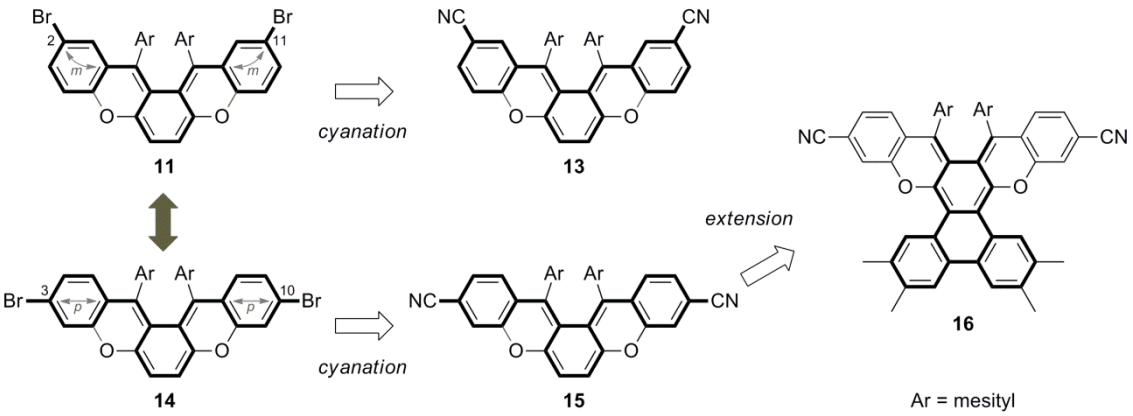

Figure 4-1. Outline for synthesis of π-extended DOP systems.

A notable property of **11** is helicity. [*n*]Helicenes and their analogues have been applied to chiroptical materials,[1] molecular-based devices,[2] and magnetoresistance elements.[3] As described in **Chapter 2**, **11** exists as two enantiomeric forms (the *P*- and *M*-isomers) because of the twisting structure due to the steric repulsion between the two mesityl groups. However, despite the steric congestion, these enantiomers are expected to rapidly racemize by flipping of the DOP framework. Here, compounds **17** and **18** (Figure 4-2) were designed in which the *p*-methyl group on the mesityl units of **11** was replaced with a *t*-butyl and trimethylsilyl group, respectively. These bulky substituents are expected to suppress the flipping motion. Hence, **17** and **18** were synthesized, and their flipping dynamics were investigated.

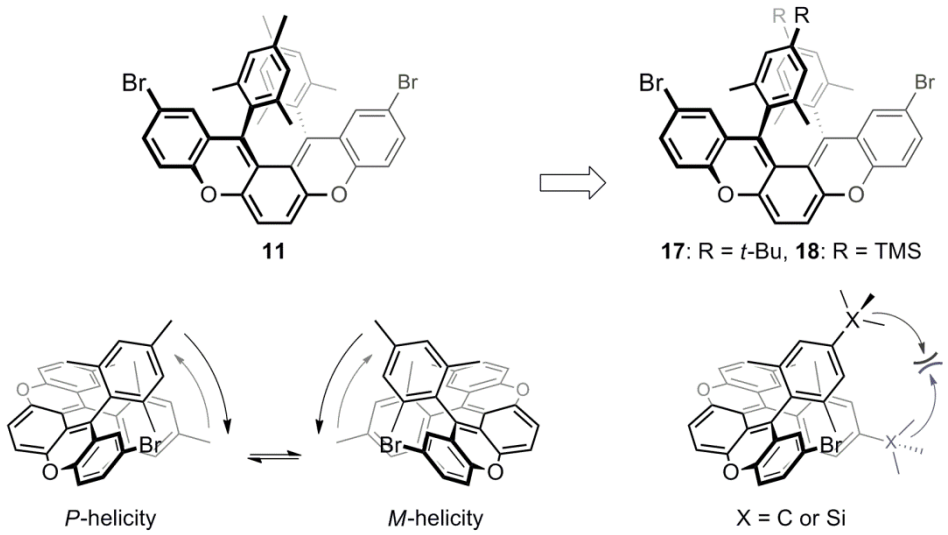

Figure 4-2. Strategy for a suppression of the flipping behavior.

4-2. Synthesis of 3,10-dibromo-13,14-dimesityl-5,8-dioxapentaphene (14)

3,10-Dibromo-DOP **14** was synthesized using a slightly modified version of the procedure described for 2,11-dibromo-DOP **11** (Scheme 4-1). Dinitrile **43** was prepared in 96% yield by the nucleophilic substitution reaction between commercially available 4-bromo-2-fluoro-benzonitrile and hydroquinone in the presence of K_2CO_3. Unfortunately, the hydrolysis of **43** under basic conditions gave the corresponding diamide because of its low solubility. Thus, **43** was converted to the corresponding dicarboxylic acid **44** in 92% yield by the acid-catalyzed hydrolysis. For the subsequent intramolecular electrophilic cyclization of **44**, whereas the reaction using concentrated H_2SO_4 gave dione **45** in low yield (~40%), the Friedel-Crafts reaction with $AlCl_3$ afforded **45** in 90% yield. Finally, the nucleophilic addition of the Grignard reagent followed by the treatment with $SnCl_2$ afforded the desired **14** as a purple solid in 39% yield over two steps.

Scheme 4-1. Synthetic route of **14**.

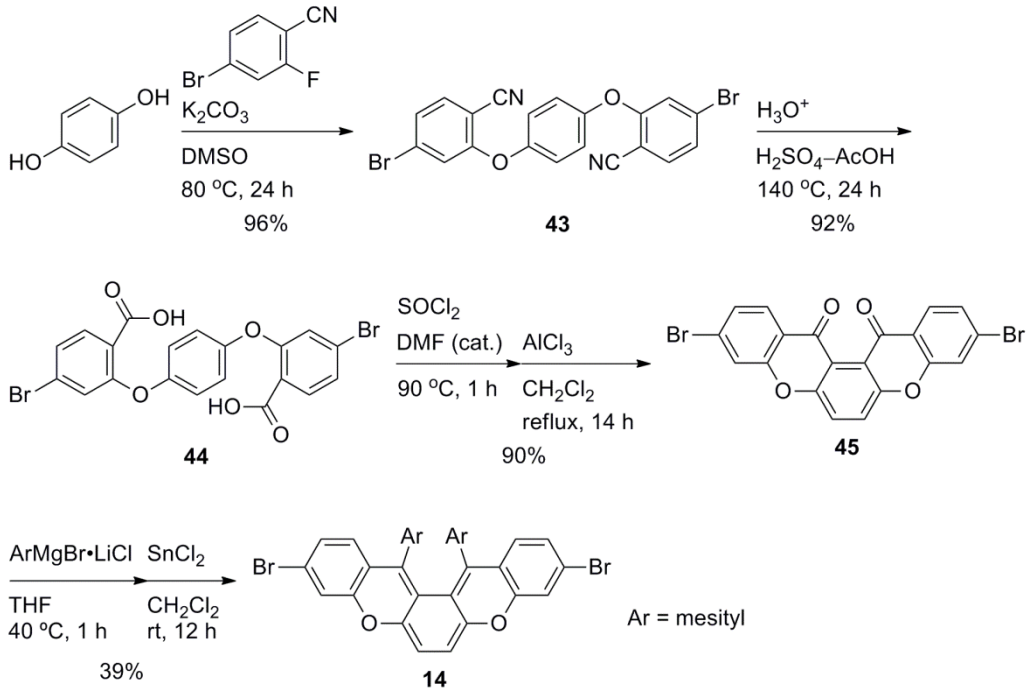

4-3. Synthesis of 2,11- and 3,10-dicyano-5,8-dioxapentaphene derivatives (13 and 15)

Cyanation of **11** and **14** was achieved by Pd-catalyzed cross-coupling reaction with $Zn(CN)_2$ (Scheme 4-2), affording the corresponding dicyano derivatives **13** and **15** in good yields (**13**: 84% and **15**: 83%). Interestingly, **13** was obtained as a purple solid similar to **11** and **14**, whereas **15** was obtained as a deep blue solid, suggesting a strong substituent effect of the cyano groups in **15**.

Scheme 4-2. Synthesis of **13** and **15**.

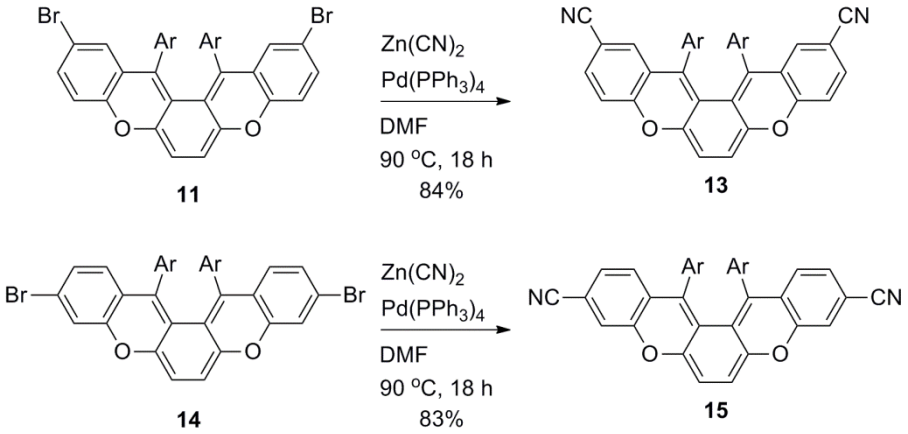

4-4. Molecular structures of 13–15

In order to gain detailed structural information on DOP derivatives **13**–**15**, X-ray structural analysis was carried out. Suitable single crystals of **13**–**15** were prepared by slow diffusion of acetonitrile into the corresponding CH_2Cl_2 solutions, and the results of the X-ray analyses are summarized in Figure 4-3 and Table 4-1–3. In the crystal state, these derivatives have a twisting structure similar to that of **11**; namely, the dihedral angles between the terminal rings *A* and *E* are 70.56° for **13**, 69.02° for **14**, and 64.34° for **15** (**11**: 64.40°). The unit cells were composed of two enantiomers in a 1:1 ratio. All of derivatives, including different colored **15**, showed clear bond-length alternations of similar extent around the central ring *C* (Table 4-4). The theoretical biradical character based on the occupation number of LUMO (*n*) was 0.091 for **13**, 0.091 for **14**, and 0.092 for **15**, (**11**: 0.091) (Table 4-5), indicating that, in the ground state, the contribution of the closed-shell structure was dominant for all DOPs.

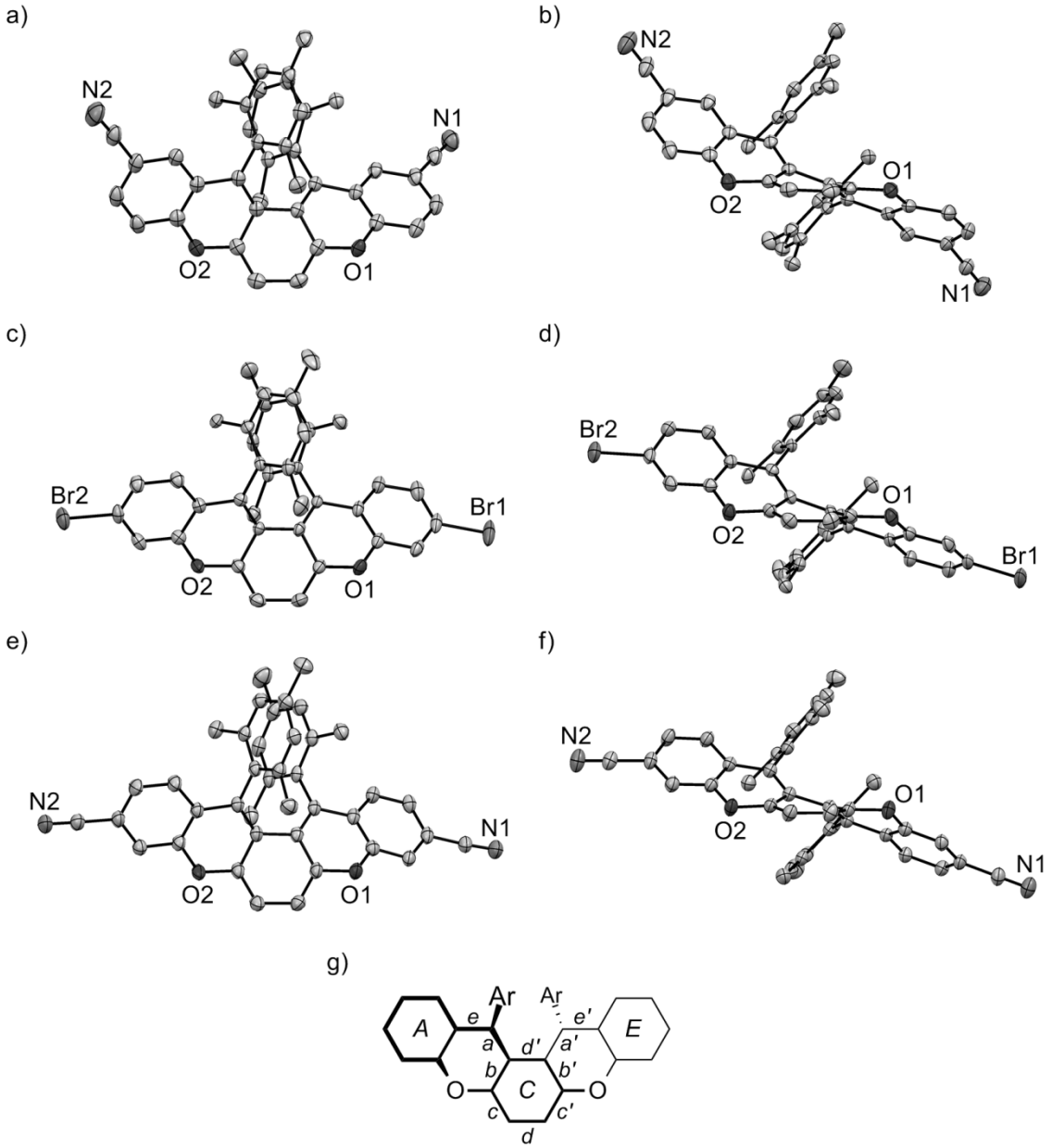

Figure 4-3. Crystal structures of (a) (b) **13**, (c) (d) **14**, and (e) (f) **15**: (a) (c) (e) TOP views and (b) (d) (f) side views along short axis of each DOP unit. Hydrogen atoms are omitted for clarity. Thermal ellipsoids set at 50%. All crystal structures were displayed as the conformer with *M*-helicity. (g) Framework of DOP skeleton. Italic symbols denote assigned names of the selected bond and ring positions.

Table 4-1. Crystallographic data of **13**.

Formula	$C_{40}H_{30}N_2O_2$	D_{calc} / g cm^{-3}	1.301
Formula weight	570.69	F(000)	600
Crystal color,	blue,	μ / cm^{-1}	0.80
morphology	block	No. of reflections	15160
Size / mm	0.15 × 0.10 × 0.03	measured	
Crystal system	triclinic	No. of unique	7904
Space group	P–1 (No. 2)	reflections	
a / Å	9.118(3)	No. of observed	5416
b / Å	12.368(4)	reflections	
c / Å	13.142(5)	No. of variables	451
α / degree	85.338(8)	Reflection	12.01
β / degree	88.100(7)	/ Parameter Ratio	
γ / degree	80.481(8)	R_1 [$I > 2.00\sigma(I)$]	0.0579
V / Å^3	1456.5(9)	R_w	0.1662
Z value	2	Goodness-of-fit	1.033
T / K	150		

Table 4-2. Crystallographic data of **14**.

Formula	$C_{38}H_{30}Br_2O_2$	D_{calc} / g cm^{-3}	1.496
Formula weight	678.45	F(000)	688
Crystal color,	blue,	μ / cm^{-1}	27.33
morphology	platelet	No. of reflections	15486
Size / mm	0.17 ×0.03 × 0.01	measured	
Crystal system	triclinic	No. of unique	6738
Space group	P–1 (No. 2)	reflections	
a / Å	8.152(12)	No. of observed	4275
b / Å	11.964(18)	reflections	
c / Å	15.91(2)	No. of variables	381
α / degree	102.80(2)	Reflection	11.22
β / degree	93.39(2)	/ Parameter Ratio	
γ / degree	93.542(18)	R_1 [$I > 2.00\sigma(I)$]	0.0479
V / Å^3	1506(4)	R_w	0.1345
Z value	2	Goodness-of-fit	0.947
T / K	150		

Table 4-3. Crystallographic data of **15**.

Formula	$C_{40}H_{30}N_2O_2$	D_{calc} / g cm^{-3}	1.283
Formula weight	570.69	F(000)	1200
Crystal color,	blue,	μ / cm^{-1}	0.79
morphology	block	No. of reflections	22534
Size / mm	0.16 × 0.13 × 0.06	measured	
Crystal system	monoclinic	No. of unique	6279
Space group	$P2_1/n$ (No. 14)	reflections	
a / Å	8.577(13)	No. of observed	4575
b / Å	24.91(4)	reflections	
c / Å	13.86(2)	No. of variables	397
α / degree	–	Reflection	11.52
β / degree	94.238(19)	/ Parameter Ratio	
γ / degree	–	R_1 [$I > 2.00\sigma(I)$]	0.0640
V / Å^3	2954(8)	R_w	0.2043
Z value	4	Goodness-of-fit	1.070
T / K	150		

Table 4-4. The selected bond lengths of **11**, **13**, **14**, and **15**.

Bonds[a]	a[b]	b[b]	c[b]	d[b]	e[b]
11	1.359(3)	1.458(3)	1.333(3)	1.436(3)	1.473(2)
13	1.371(2)	1.461(2)	1.339(2)	1.438(2)	1.472(2)
14	1.361(4)	1.466(5)	1.340(5)	1.436(5)	1.476(5)
15	1.369(3)	1.464(4)	1.346(3)	1.449(3)	1.478(3)
Bonds[a]	a'[b]	b'[b]	c'[b]	d'[b]	e'[b]
11	1.359(3)	1.461(3)	1.333(3)	1.485(3)	1.470(2)
13	1.369(2)	1.468(2)	1.332(2)	1.484(2)	1.470(2)
14	1.361(6)	1.462(5)	1.336(5)	1.476(5)	1.483(5)
15	1.367(3)	1.466(4)	1.338(4)	1.500(3)	1.487(3)

[a] Assignment bond names are shown in Figure 4-3. [b] In Å unit.

Table 4-5. Calculated occupation number of LUMO (n) of **13**, **14**, and **15**.

Compounds	**13**	**14**	**15**
Occupation number of LUMO (n)[a]	0.0913810	0.0913084	0.0908010

[a] Calculated at the CASSCF(2,2)/6-31G//RB3LYP/6-31G** level.

4-5. Electronic properties of 13–15

The UV–vis absorption spectra of **13** and **14** in CH_2Cl_2 (Figure 4-4) showed a broad absorption band in the visible region (**13**: λ_{max} = 554 nm, $\varepsilon = 9.73 \times 10^3$ M^{-1} cm^{-1}; **14**: λ_{max} = 554 nm, $\varepsilon = 1.24 \times 10^4$ M^{-1} cm^{-1}) similar to that of **11**. On the other hand, 3,10-dicyano derivative **15** has a highly red-shifted absorption band up to ~800 nm (λ_{max} = 595 nm, $\varepsilon = 1.12 \times 10^4$ M^{-1} cm^{-1}). To understand these results, the HOMOs and LUMOs were compared (Figure 4-5). The DFT calculations showed that the LUMO of **15** was extended over cyano groups, whereas the shape of the HOMO was similar to that of the other derivatives, indicating that the cyano groups at the 3- and 10-positions of **15** mainly affected the LUMO energy level.

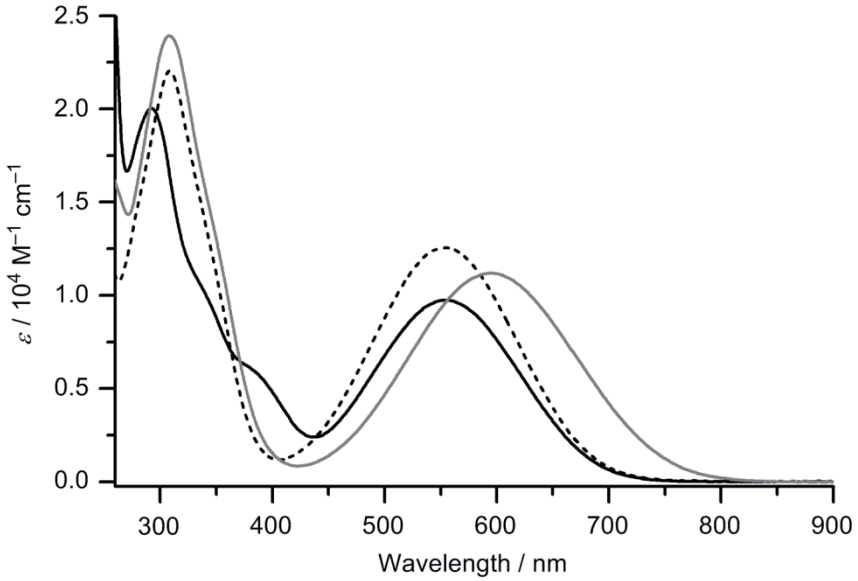

Figure 4-4. UV−vis absorption spectra of **13** (black solid), **14** (black dash), and **15** (gray solid) in CH_2Cl_2.

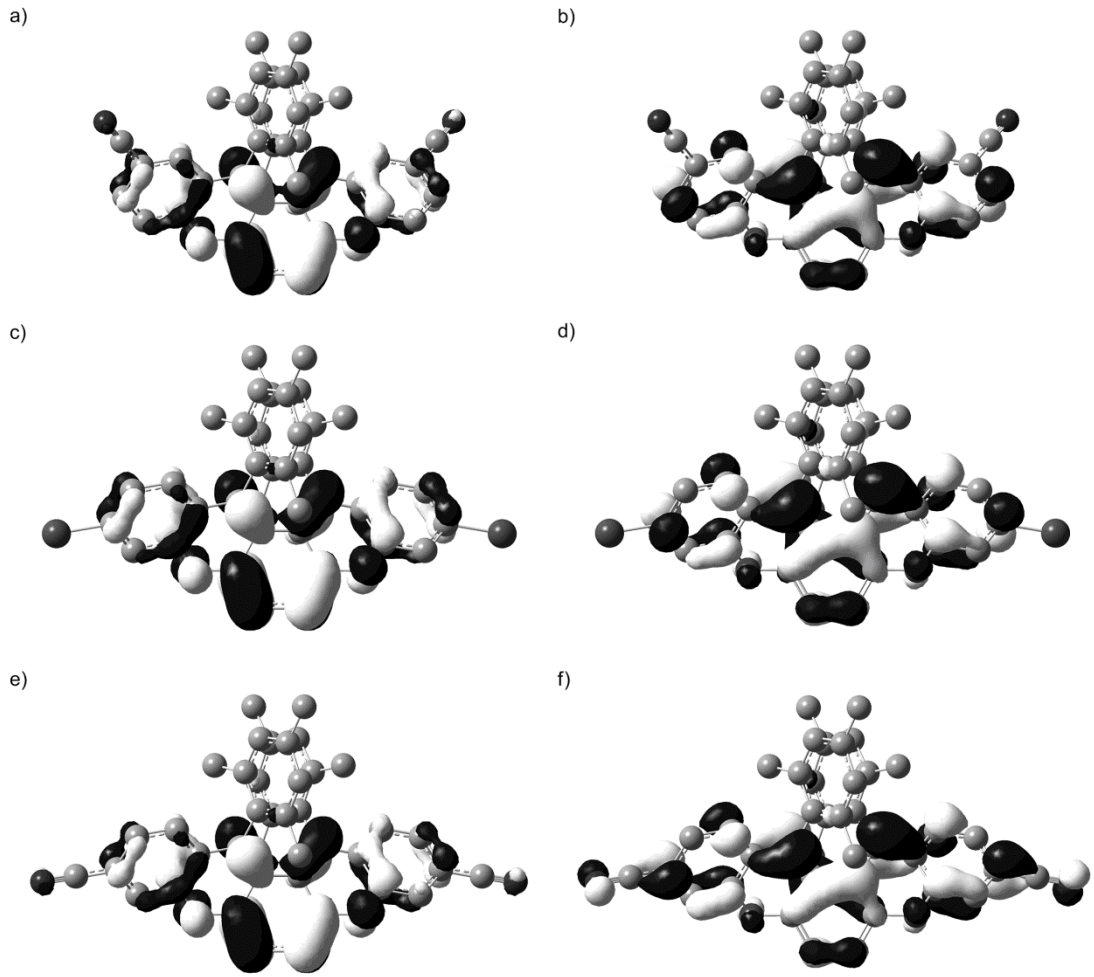

Figure 4-5. Calculated structures and orbitals; (a) HOMO and (b) LUMO of **13**, (c) HOMO and (d) LUMO of **14**, and (e) HOMO and (f) LUMO of **15** (isovalue = 0.030) optimized at the DFT RB3LYP/6-31G** level. Hydrogen atoms are omitted for clarity.

The cyclic voltammograms of 3,10-dibromo derivative **14** in CH_2Cl_2 (Figure 4-6) showed two reversible oxidation waves similar to those of 2,11-dibromo DOP **11**, but no reduction wave was observed. On the other hand, the voltammograms of **13** and **15** showed one reversible oxidation wave at the same potential (+0.25 V vs Fc/Fc^+), suggesting that the cyano groups had a similar degree of effect on the HOMO energy level through different conjugation pathways. Moreover, **15** revealed two reversible reduction waves at –1.68 V and –1.96 V. These results indicate that the mono- and di-anionic species of **15** are electrochemically stable because of the delocalization of the LUMO over the two cyano groups. The observed redox potentials are summarized in Table 4-6.

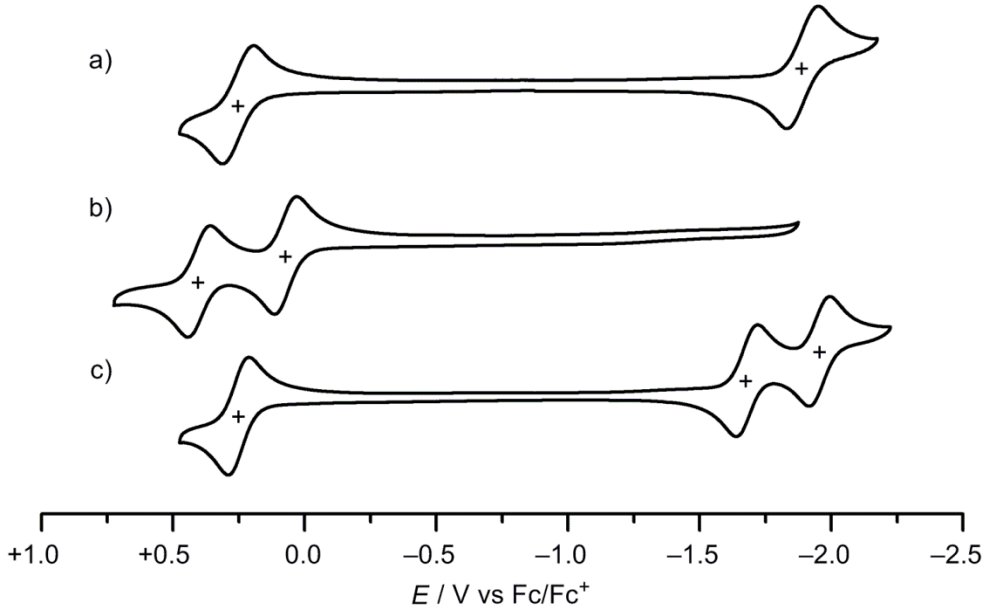

Figure 4-6. Cyclic voltammograms of (a) **13**, (b) **14**, and (c) **15** in CH_2Cl_2 containing 0.1 M *n*-Bu_4NPF_6 as a supporting electrolyte at a scan rate of 100 mV s^{-1}.

Table 4-6. Redox potentials of **13**, **14**, and **15** in CH_2Cl_2.[a]

Compounds	E_{ox2}	E_{ox1}	E_{red1}	E_{red2}
13	–[b]	+0.25	–1.89	–[b]
14	+0.40	+0.07	–[c]	–[b]
15	–[b]	+0.25	–1.68	–1.96

[a] vs Fc/Fc^+ (+0.38 V vs SCE). [b] Not observed. [c] Irreversible at around –2.0V.

4-6. Synthesis of π-extended 5,8-dioxapentaphene system (16)

The two reduction waves and one oxidation wave observed for 3,10-dicyano-DOP **15** suggest that the DOP system has amphoteric multistep redox ability based on the quinoidal conjugation. In addition, the signal of the central *o*QDM protons of **15** appeared at 5.71 ppm in the ^{1}H NMR spectrum (in $CDCl_3$), suggesting that the carbon atoms at the 6- and 7-positions are electron-rich even after the cyanation.

Thus, further bromination at the 6- and 7-positions of **15** was performed to create new reactive sites for π-extension. After optimization, the desired 6,7-dibromo derivative **46** was obtained in 88% yield using *N*-bromosuccinimide in THF (Scheme 4-3). The Suzuki-Miyaura coupling reaction of **46** with 2,2'-bis(4,4,5,5-tetramethyl-1,3,2-dioxaborolane-2-yl)-4,4',5,5'-tetramethylbiphenyl produced the crude phenanthrene-fused DOP derivative **16** in poor yield (6%, crude). After repeating purification by column chromatography on silica gel, almost pure **16** was obtained in sufficient amount for photophysical and electrochemical studies.

Scheme 4-3. Synthesis of **16**.

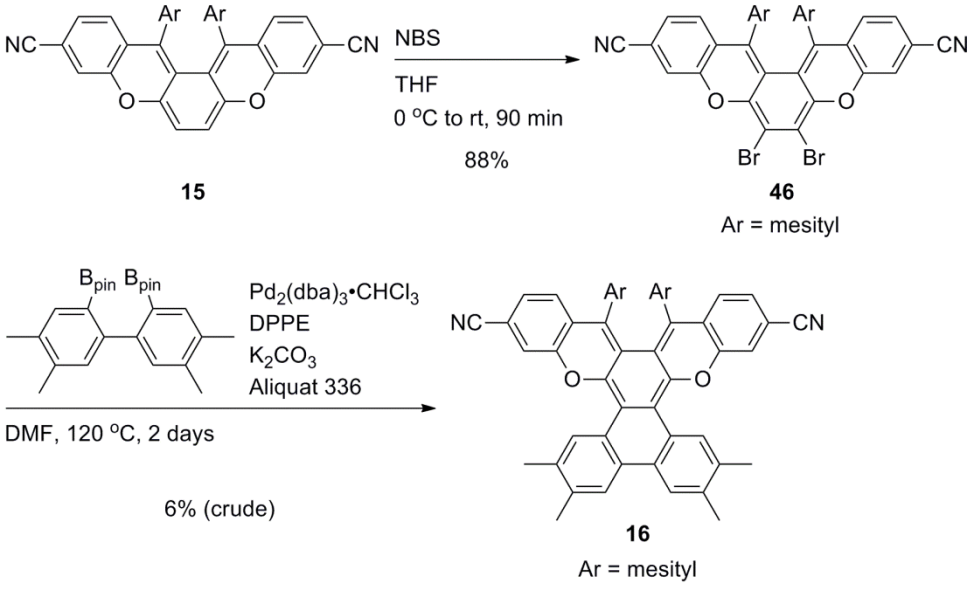

4-7. Electronic properties of 16

The UV–vis absorption spectrum of **16** in CH_2Cl_2 showed a significantly red-shifted absorption band up to 900 nm (Figure 4-7), indicating that the electronic structure of the DOP unit was strongly conjugated with the fused phenanthrene skeleton. In fact, the DFT calculation of **16** (Figure 4-8) revealed a large HOMO coefficient around the phenanthrene-fused *o*QDM skeleton. On the other hand, the shape of the LUMO of **16** was similar to that of **15**. These results indicate that, in contrast to cyanation, the π-extension in **16** mainly affected the HOMO energy level. In addition, the observed lowest-energy absorption band can be presumably attributed to a charge-transfer transition. The occupation number of LUMO (*n*) of **6** was calculated to be 0.091, indicating its closed-shell structure, similarly to the other derivatives.

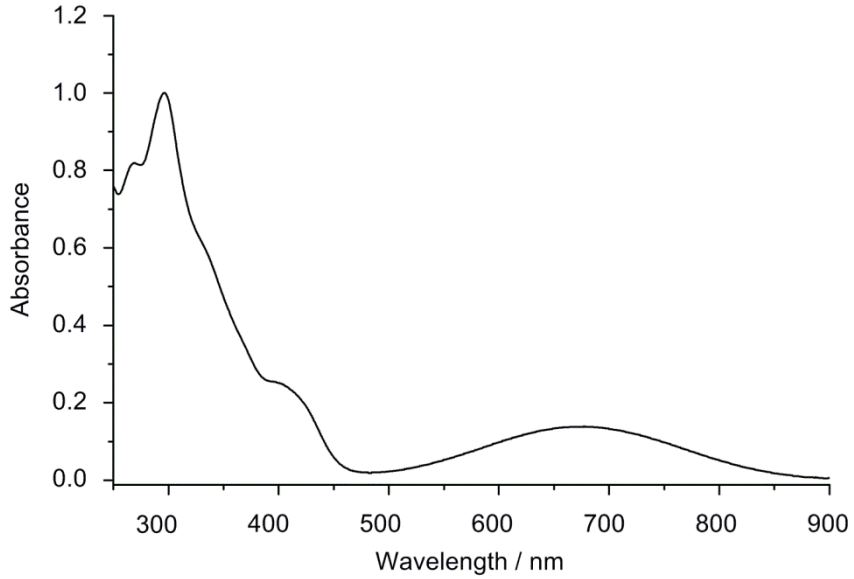

Figure 4-7. UV−vis absorption spectrum of **16** in CH_2Cl_2.

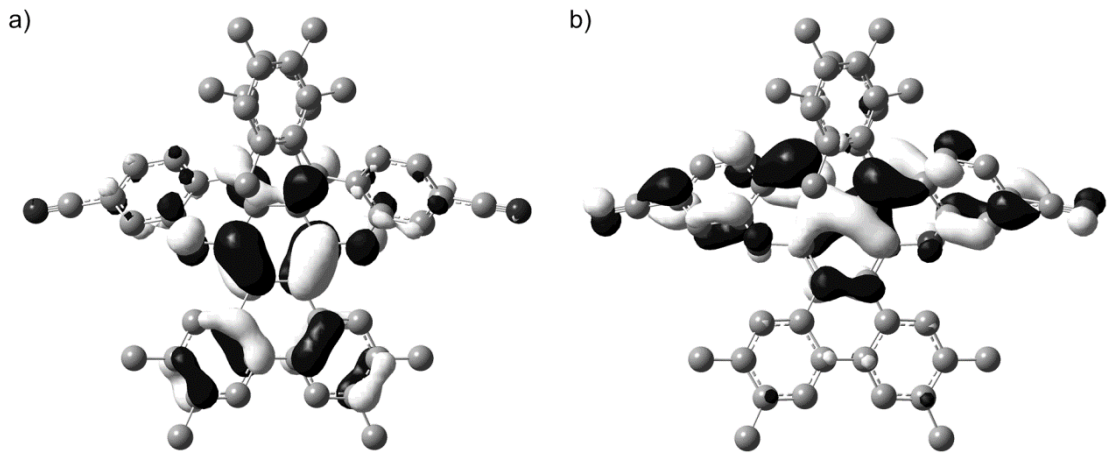

Figure 4-8. Calculated structure and orbitals; (a) HOMO and (b) LUMO of **16** (isovalue = 0.030) optimized at the DFT RB3LYP/6-31G** level. Hydrogen atoms are omitted for clarity.

The cyclic voltammogram of **16** in CH_2Cl_2 (Figure 4-9) showed two reversible reduction waves and two reversible oxidation waves (E^{ox2} = +0.31 V, E^{ox1} = +0.05 V, E^{red1} = –1.60 V, E^{red2} = –1.87 V vs Fc/Fc^+), suggesting that the DOP system of **16** is able to form the electrochemically stable mono- and di-anionic and -cationic species. These results clearly indicate the superior amphoteric redox ability of **16** due to the extended π-system.

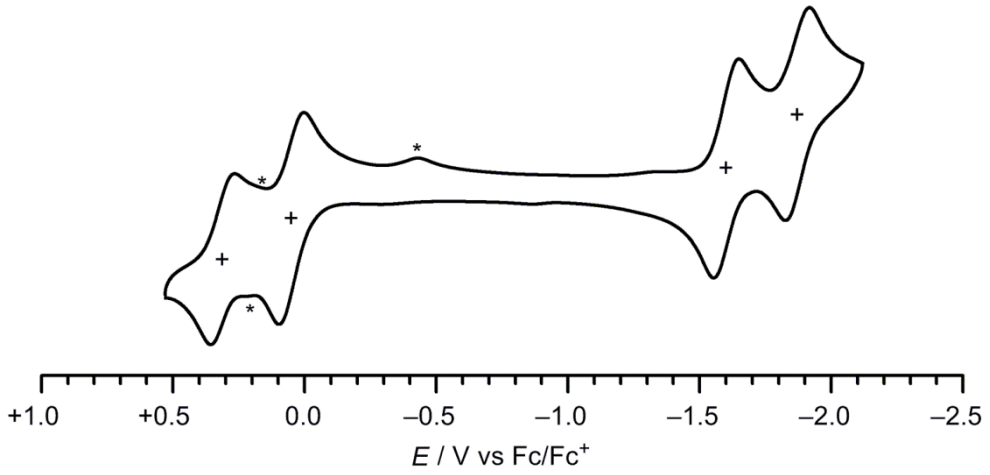

Figure 4-9. Cyclic voltammogram of **16** in CH_2Cl_2 containing 0.1 M *n*-Bu_4NPF_6 as a supporting electrolyte at a scan rate of 100 mV s^{-1}; *peaks of some impurity.

4-8. Synthesis of 5,8-dioxapentaphenes bearing bulky aryl groups (17 and 18)

DOP derivatives **17** and **18** bearing bulky aryl groups were prepared following a procedure similar to that described for **11**, using the corresponding aryl Grignard reagent instead of the mesityl Grignard reagent (Scheme 4-4).

Scheme 4-4. Synthesis of **17** and **18**.

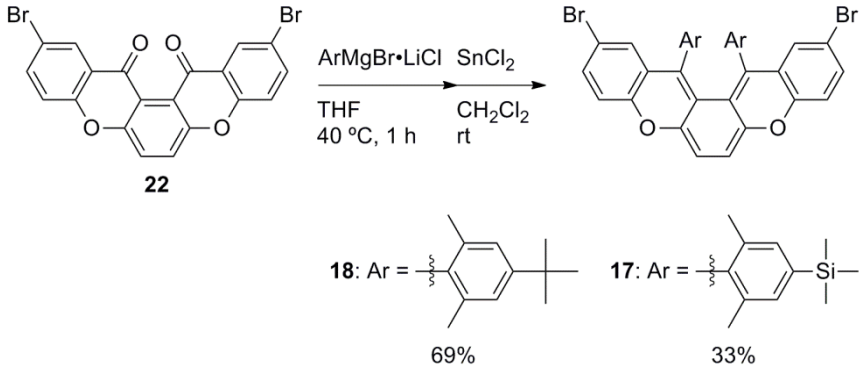

4-9. Molecular structures of 17 and 18

The detailed structures of **17** and **18** were determined by X-ray structural analysis (Figure 4-10 and Table 4-8–9). Recrystallization by slow diffusion of acetonitrile into the corresponding CH_2Cl_2 solution gave suitable crystals for X-ray analysis. In the crystal state, both **17** and **18** showed a twisting structure (**17**: 62.97° and **18**: 73.18°) similar to that of **11**. From the crystal structures, the cone angles (θ) and radii (r) were estimated to be θ = 52.74° and r = 0.905 Å for the methyl group (Me) in **11**, θ = 99.00° and r = 2.047 Å for the *t*-butyl group (*t*-Bu) in **17**, θ = 95.01° and r = 2.351 Å for the trimethylsilyl group (TMS) in **18** (Table 4-7).

Table 4-7. Cone angles (θ) and radii (r) of methyl (Me), *t*-butyl (*t*-Bu), and trimethylsilyl (TMS) groups in the crystal structures of **11**, **17**, and **18**, respectively.

Groups (Compounds)	Cone angles $(\theta)^{[a,b]}$ / deg	Radii $(r)^{[a,b]}$ / Å
Me (**11**)	52.74	0.905
t-Bu (**17**)	99.00	2.047
TMS (**18**)	95.01	2.351

[a] Mean values. [b] The measured positions are shown in the following drawing:

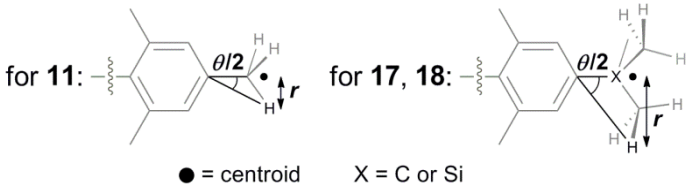

where each centroid was defined as a middle position of the hydrogen atoms in a bottom of the corresponding cones.

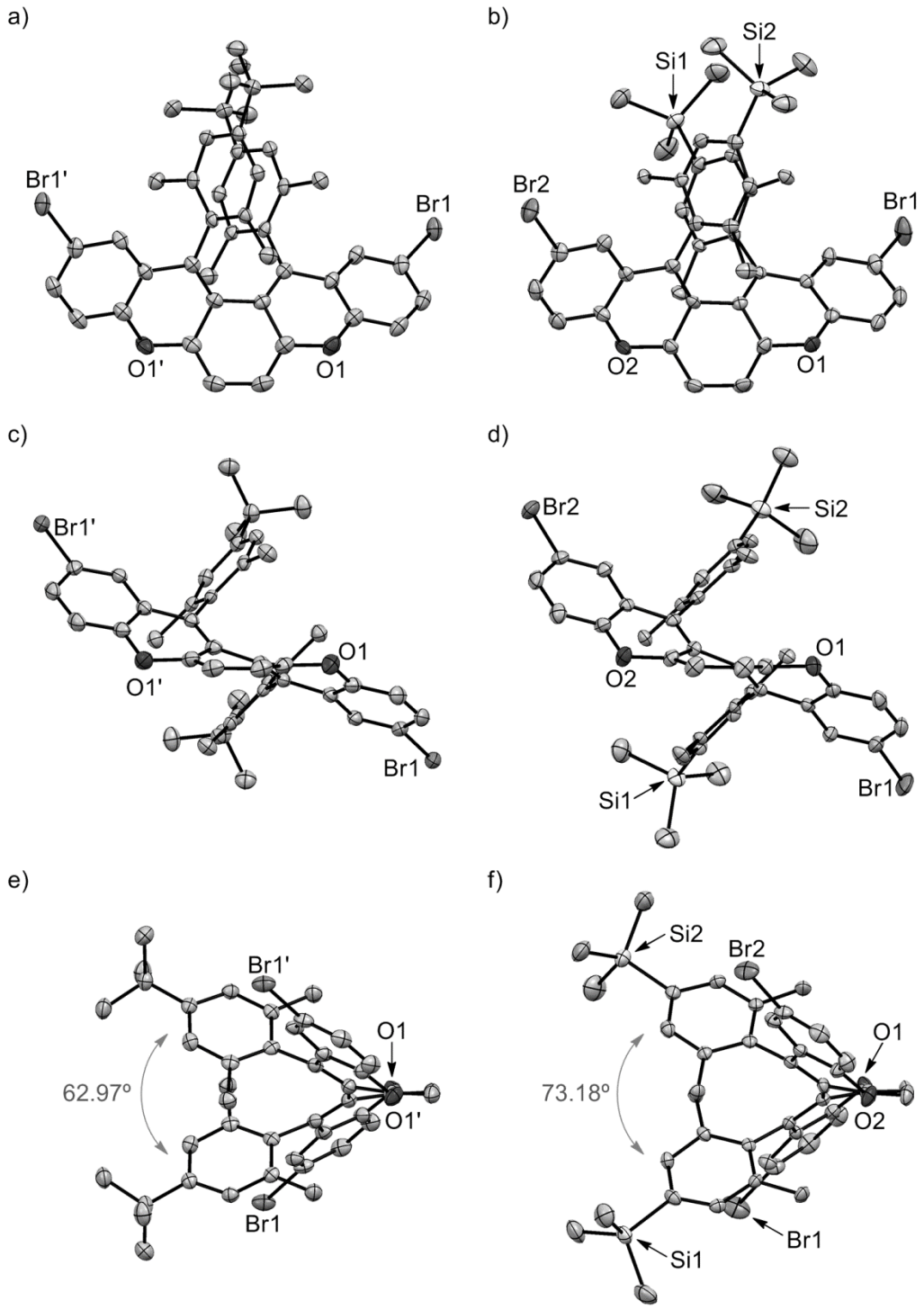

Figure 4-10. Crystal structures of (a) (c) (e) **17** and (b) (d) (f) **18**: (a) (b) TOP views and side views along (c) (d) long and (e) (f) short axis of each DOP unit. Hydrogen atoms are omitted for clarity. In (b), (d), and (f), crystal solvent was omitted for clarity. Thermal ellipsoids set at 50%. All crystal structures were displayed as the conformer with *M*-helicity. In (e) and (f), gray double-headed arrows and values indicate the dihedral angles between terminal rings in each DOP unit.

Table 4-8. Crystallographic data of **17**.

Formula	$C_{44}H_{42}Br_2O_2$	D_{calc} / g cm^{-3}	1.435
Formula weight	762.62	F(000)	1568
Crystal color,	blue,	μ / cm^{-1}	23.41
morphology	block	No. of reflections	22299
Size / mm	0.30 × 0.05 × 0.02	measured	
Crystal system	orthorhombic	No. of unique	3500
Space group	*Pbcn* (No. 60)	reflections	
a / Å	12.003(2)	No. of observed	2835
b / Å	17.626(3)	reflections	
c / Å	13.142(5)	No. of variables	238
α / degree	–	Reflection	11.91
β / degree	–	/ Parameter Ratio	
γ / degree	–	R_1 [$I > 2.00\sigma(I)$]	0.0338
V / Å^3	3529.4(10)	R_w	0.0497
Z value	4	Goodness-of-fit	1.024
T / K	150		

Table 4-9. Crystallographic data of **18**.

Formula	$C_{42}H_{42}Br_2O_2Si_2$•C_2H_3N	D_{calc} / g cm^{-3}	1.351
Formula weight	835.82	F(000)	860
Crystal color,	blue,	μ / cm^{-1}	20.74
morphology	platelet	No. of reflections	21371
Size / mm	0.12 ×0.03 × 0.01	measured	
Crystal system	triclinic	No. of unique	9296
Space group	*P*–1 (No. 2)	reflections	
a / Å	10.21(2)	No. of observed	6288
b / Å	11.76(2)	reflections	
c / Å	19.48(5)	No. of variables	460
α / degree	72.85(11)	Reflection	13.67
β / degree	83.50(14)	/ Parameter Ratio	
γ / degree	66.81(10)	R_1 [$I > 2.00\sigma(I)$]	0.0496
V / Å^3	2054(8)	R_w	0.1497
Z value	2	Goodness-of-fit	1.025
T / K	150		

4-10. Experimental investigation of the flipping dynamics of 17 and 18

Flipping dynamics were observed in the variable-temperature ^{1}H NMR spectra of **17** and **18** in *o*-dichlorobenzene-d_4 (Figure 4-11). Because the signals of the *m*-aryl protons overlapped with other aromatic signals, the parameters of the dynamics were estimated using the *o*-methyl protons. In the measurements of **17** and **18**, the correlated peaks *D* and *E* showed clear line-width broadening over ~383 K, but coalescence was not observed in the range 298–403 K. The racemization barriers ($\Delta G^{\ddagger}$) of **17** and **18** were estimated by line-shape analysis (Table 4-10–11).[4] Unexpectedly, a decrease in their line width was observed with increasing temperature in the range 298–343 K regions, probably due to the relaxation of the steric constraints. Thus, the line widths at 343 K were used as the reference for the analysis. As a result, the activation barrier $\Delta G^{\ddagger}$ was estimated from the Arrhenius plots to be ~83.81 kJ mol^{-1} for **17** and ~97.91 kJ mol^{-1} for **18** (Figure 4-12). Unfortunately, these $\Delta G^{\ddagger}$ values were lower than the 100 kJ mol^{-1} required to perform optical resolution at room temperature.[5] These results clearly indicate that the flipping behavior of the DOP unit is suppressed by the bulky substituents at the *para*-position of the aryl moieties.

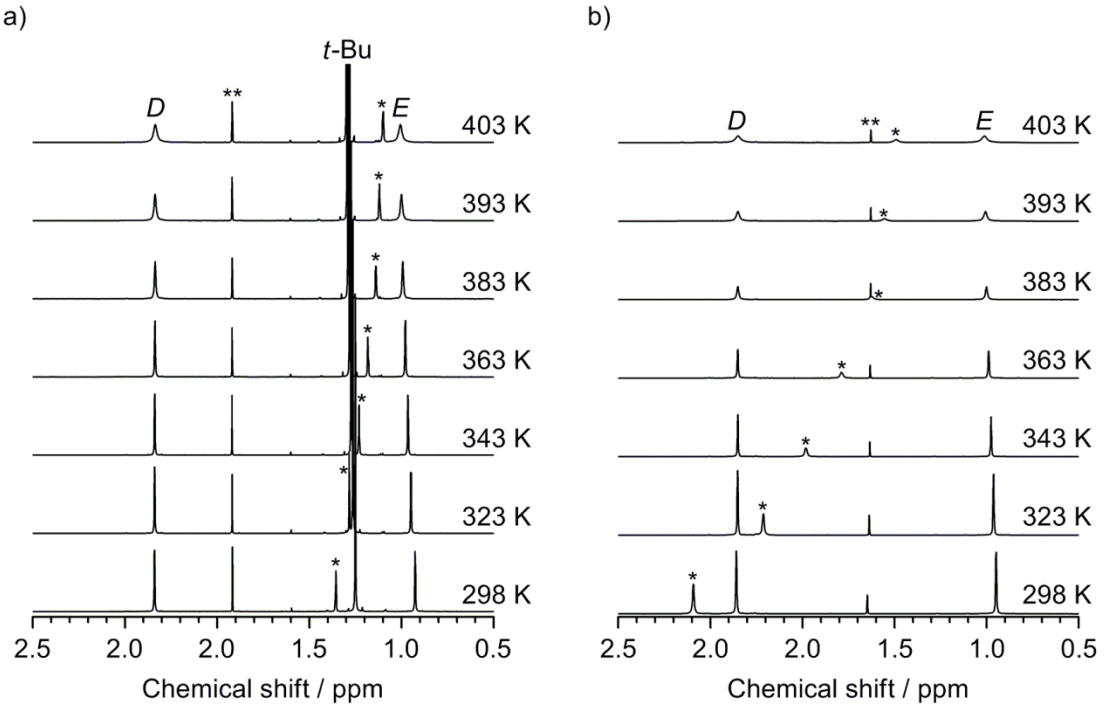

Figure 4-11. Temperature-dependent ^{1}H NMR spectra (from 298 K to 403 K, 400 MHz) of (a) **17** and (b) **18** in *o*-dichlorobenzene-d_4 at selected regions (2.50–0.50 ppm); * and ** indicate water and residual solvent, respectively. Assignments of signals are shown in Table 4-11.

Table 4-10. Experimental values of line widths (W) and rate constants (k) at each temperature for the flipping dynamics of **17** in *o*-dichlorobenzene-d_4.

T / K	298	323	343	363	383	393	403
$W_{obs}{}^{D}$ / Hz[a]	1.655	1.659	1.684	1.901	3.354	5.147	9.059
$W_{obs}{}^{E}$ / Hz[a]	1.811	1.512	1.491*	1.900	3.476	5.347	8.911
$W_{ave}{}^{DE}$ / Hz[b]	1.733	1.585	1.588	1.901	3.415	5.247	8.987
k / s^{-1}[c]	–	–	0.302	1.286	6.043	11.799	23.540

[a] Full width at half maximum values of the observed signals *D* and *E*. Assignments of signals are shown in Table 4-11. [b] Mean values of $W_{obs}{}^{D}$ and $W_{obs}{}^{E}$. [c] The exchanging rate constants were estimated by the line-shape analysis method[4] using the following equation:

$$k = \pi \left(W_{obs} - W_{ref} \right)$$

where W_{obs} is the width at half maximum values of the observed signals and W_{ref} is the width at half maximum values of the signal when the exchanging effect on the line width can be ignored. In this analysis, W_{obs} and W_{ref} set $W_{ave}{}^{DE}$ and the value shown with the * symbol, respectively.

Table 4-11. Experimental values of line widths (W) and rate constants (k) at each temperature for the flipping dynamics of **18** in *o*-dichlorobenzene-d_4.

T / K	298	323	343	363	383	393	403
$W_{obs}{}^{D}$ / Hz[a]	2.386	2.107	1.716*	2.353	4.902	8.437	15.082
$W_{obs}{}^{E}$ / Hz[a]	2.337	2.115	1.866	2.444	4.942	8.278	14.406
$W_{ave}{}^{DE}$ / Hz[b]	2.3617	2.111	1.791	2.398	4.922	8.357	14.744
k / s^{-1}[c]	–	–	0.236	2.143	10.072	20.864	40.929

[a] Full width at half maximum values of the observed signals *D* and *E*. Assignments of signals are shown in the following drawing. [b] Mean values of $W_{obs}{}^{D}$ and $W_{obs}{}^{E}$. [c] See the above equation.

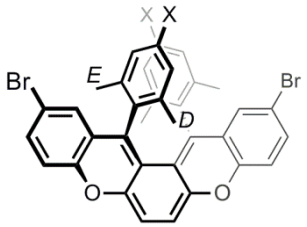

17: X = *t*-Bu, **18**: X = TMS

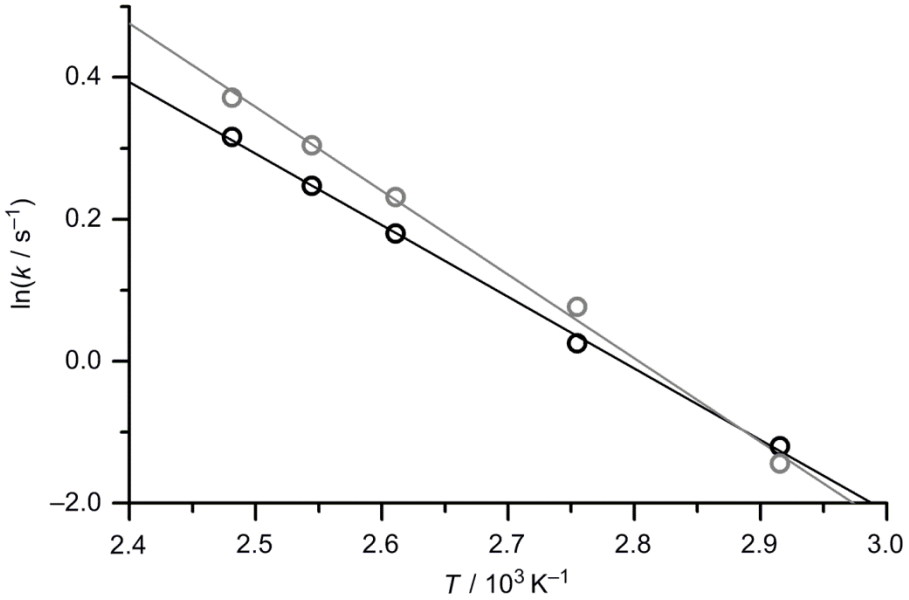

Figure 4-12. Arrhenius plots for the estimated rates of the flipping dynamics of **17** (black circles) and **18** (gray circles) in *o*-dichlorobenzene-d_4. Black and gray lines are approximation straight lines for the plots of **17** and **18**, respectively; the fitted functions are the following equations.

$$\text{for } \mathbf{17}: \quad y = -10081x + 28.126 \quad \left(R^2 = 0.9986\right)$$

$$\text{for } \mathbf{18}: \quad y = -11776x + 33.018 \quad \left(R^2 = 0.9965\right)$$

4-11. Computational investigation of the flipping dynamics of 11, 17, and 18

To obtain further information on the flipping behavior of the DOP unit, I conducted theoretical calculations for the racemization processes of **47**, **48**, and **49**, which were selected as the model compounds of **11**, **17**, and **18**, respectively, without bromine atoms to reduce the calculation time.

First, in order to find the saddle points of the racemization reaction, the energy paths from the *M*- to the *P*-form were estimated by the *MOPAC* program using the keywords EF (i.e., optimization) and STEP at the PM7 level to modify the twisting angles (Figure 4-13). It should be noted that the energy values estimated by this method are not accurate because through-space interactions are underestimated by the MNDO-type PM7 Hamiltonian method. Interestingly, the crossing points of the *p*-substituents (*C*) were observed before the saddle points, whereas the flipping points of the DOP unit (*F*) appeared after the saddle points. These results suggest that racemization of the twisted DOP skeleton is mainly due to the crossing of the two aryl groups at the 13- and 14-positions.

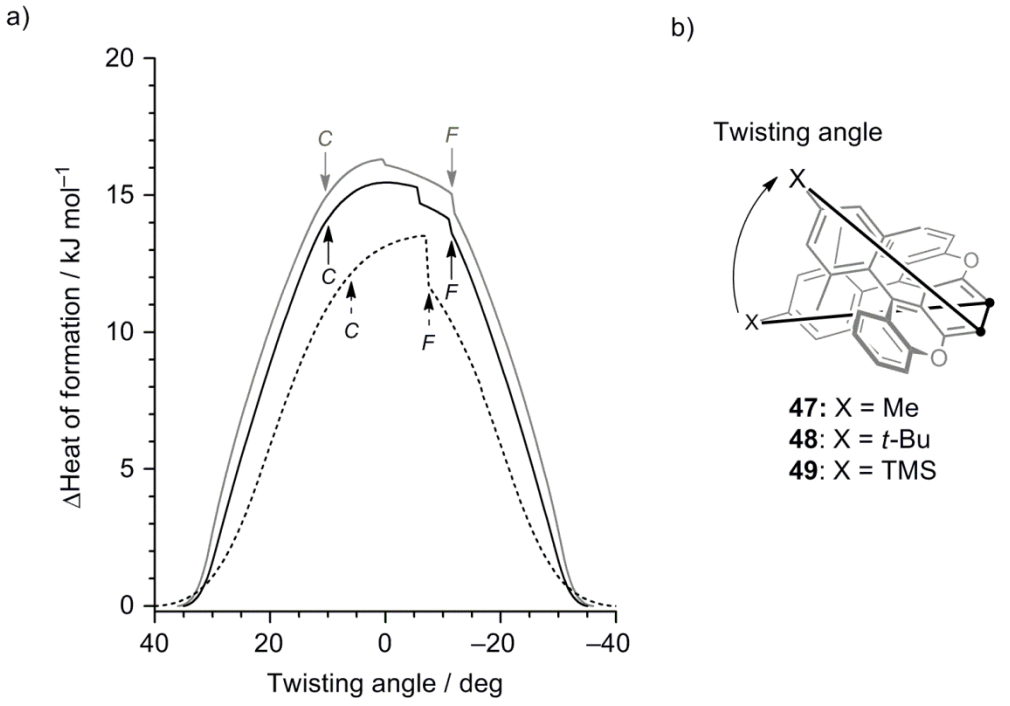

Figure 4-13. (a) Racemization energy paths of **47** (black dash), **48** (black solid), and **49** (gray solid) calculated at PM7 level. Arrowed points *C* denote the crossing point of the *p*-substituents. Arrowed points *F* denote the filling points of each DOP unit. (b) Framework of **47**, **48**, and **49**. Black solid lines and arrow denote the dihedral angle to define their twisting angles.

Next, calculations using the TS keyword at the PM7 level were performed to pre-optimize the structures at the saddle points. Finally, to examine the structures and energies at the transition state, the calculated structures were optimized at the DFT RB3LYP/6-31** level using the Opt=TS keyword of the *Gaussian* program, followed by calculations using the Freq keyword. The most stable structures of **47**, **48**, and **49** were optimized using the standard method at the same level.

The resulting structures of **48** and **49** at the transition states (Figure 4-14) showed highly bent aryl groups as compared to that of **47**, due to the steric repulsion around the *para*-substituents. The theoretical racemization barriers were estimated from the difference between the heat of formation (*HF*) of the transition state and that of the most stable state, with (ΔG) or without (ΔHF) zero-point correction (Table 4-12). All calculated racemization barriers ΔG were similar to the corresponding experimental $\Delta G^{\ddagger}$ values. Interestingly, **49** had the highest ΔG value, whereas the calculated ΔHF value of **49** was smaller than that of **48**. In fact, the experimental $\Delta G^{\ddagger}$ of **49** was higher than that of **48** despite the smaller cone angle of the TMS group compared to that of the *t*-Bu group. From the theoretical results, the higher of $\Delta G^{\ddagger}$ of **49** was assumed to be due to the rotation dynamics of TMS group in the congested area.

The experimental and theoretical results for the racemization of DOP unit indicate that optimization of the aryl groups may allow to separate the helicity of twisting DOP units.

Table 4-12. Calculated values of **47**, **48**, and **49** by DFT at the RB3LYP/6-31** level: Number of imaginary frequencies (N_i), Heat of formations (*HF*), and Gibbs free energies (*G*).

Compounds	N_i	HF[c] / Hartrees	ΔHF[c] / kJ mol^{-1}	G[d] / Hartrees	ΔG[d] / kJ mol^{-1}
47[a]	0	–1617.807369	0	–1617.284745	0
47-TS[b]	1	–1617.778030	77.03	–1617.254242	80.09
48[a]	0	–1853.697443	0	–1853.011398	0
48-TS[b]	1	–1853.663876	88.13	–1852.976923	90.51
49[a]	0	–2356.543179	0	–2355.887601	0
49-TS[b]	1	–2356.510457	85.91	–2355.852042	93.36

[a] The optimized most stable states. [b] Transition states. [c] Without zero-point correction. [d] The values of Sum of electronic and thermal Free Energies. See also Figure 4-14.

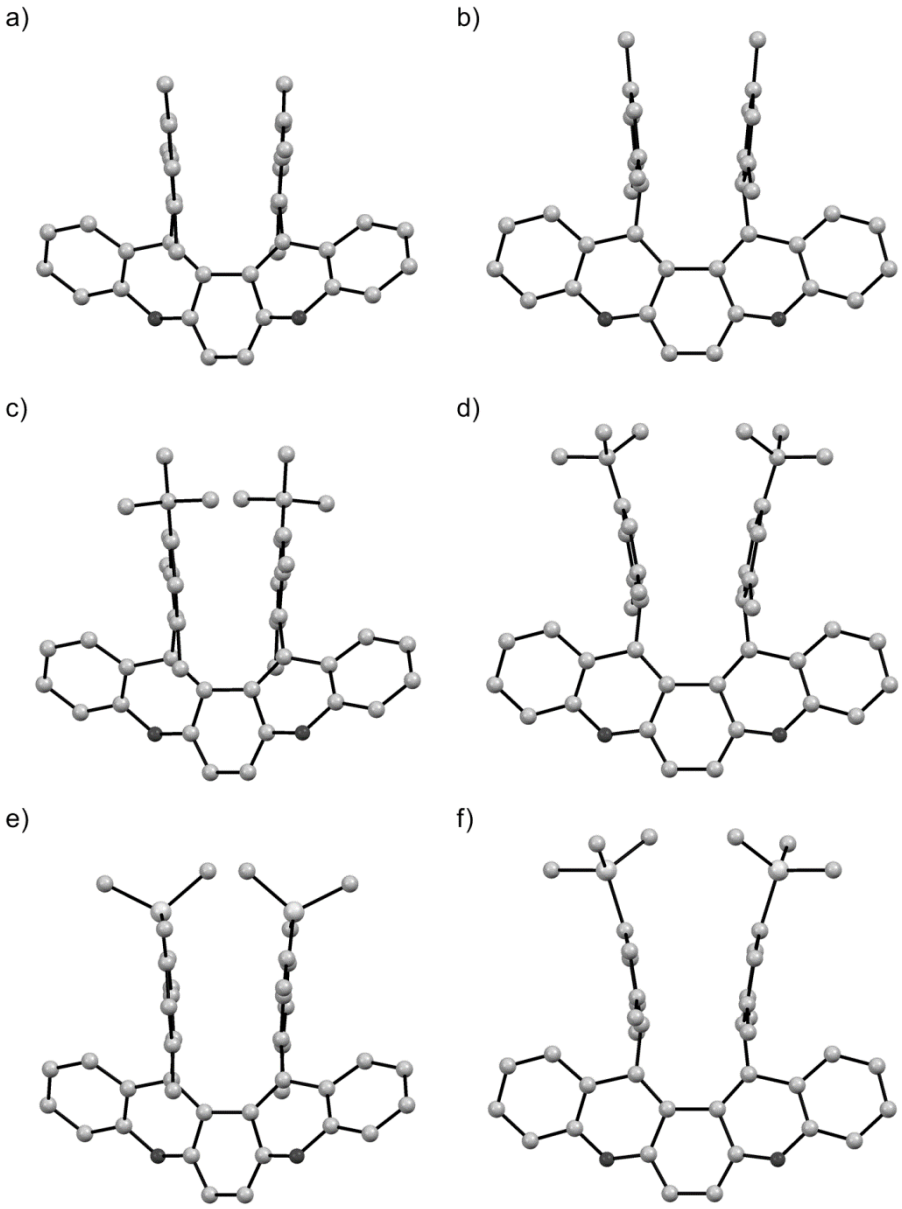

Figure 4-14. The optimized structures of (a) (b) **47**, (c) (d) **48**, and (e) (f) **49** as (a) (c) (e) their most stable states and (b) (d) (f) their transition states at DFT at the RB3LYP/6-31** level.

4-12. Experimental section

General Methods

- Melting points were taken on a Yanaco MP J-3 and were uncorrected.
- ^{1}H and ^{13}C NMR spectra were recorded on a Bruker Avance III 400 spectrometer (400 MHz for ^{1}H and 100 MHz for ^{13}C).
- Variable temperature ^{1}H NMR spectra of **17** and **18** were recorded on a JEOL ECZ-400 spectrometer (400 MHz for ^{1}H).

  # Chemical Shifts were reported in parts per million downfield for tetramethylsilane as an internal standard or relative to solvent signal (chloroform: δ = 7.26 for ^{1}H NMR and δ = 77.0 ppm for ^{13}C NMR; dimethyl sulfoxide: δ = 2.50 for ^{1}H NMR and δ = 39.5 ppm for ^{13}C NMR; trifluoroacetic acid: δ = 11.50 for ^{1}H NMR and δ = 164.2 and 116.6 ppm for ^{13}C NMR; *o*-dichlorobenzene: δ = 7.19 and 6.93 ppm for ^{1}H NMR) as internal standards, and all coupling constants are reported in Hz (Multiplicity: s = singlet; d = doublet; br = broad).
- IR spectra were recorded on a JASCO FT/IR-4600 spectrometer.
- DART-TOF and ESI-TOF mass spectra were recorded on a JEOL AccuTOF spectrometer.
- High-resolution mass spectra (DART-TOF and ESI-TOF) were recorded on a JEOL AccuTOF spectrometer.
- Elemental analyses were obtained from the Analytical Center in Osaka City University, using a Fisons EA1108 and a J-Science JM10.
- X-ray data were collected by a Rigaku Saturn 724 CCD system with graphite monochromated Mo-Kα radiation.
- Absorption spectra were recorded on a Shimadzu UV-2550 spectrometer
- Redox potentials were measured using an ALS Electrochemical analyzer MODEL 610A in a conventional three-electrode cell equipped with a glassy carbon as a working electrode and a platinum wire as a counter electrode with a SCE reference electrode. The measurement was carried out at a scan rate 100 mV s^{-1} in dichloromethane containing 0.1 M tetra-*n*-butylammonium hexafluorophosphate as a supporting electrolyte. The redox potentials were finally corrected by the ferrocene/ferrocenium (Fc/Fc^{+}) couple.

Materials

- Merck gel 60 (63–200 mesh) or Kanto Chemical Silica gel 60 (100–200 mesh) were used for column chromatography.
- The progress of reactions was monitored using thin-layer chromatography using Merck TLC silica gel 60 F254.
- All commercially available compounds were reagent grade and used without further purification.
- Dehydrate dimethyl sulfoxide was purchased.
- Tetrahydrofuran was dried and distilled over sodium.
- Dichloromethane was dried and distilled over calcium hydride.

Synthetic procedures and compounds data

1,4-Bis(5-bromo-2-cyanophenoxy)benzene (43)

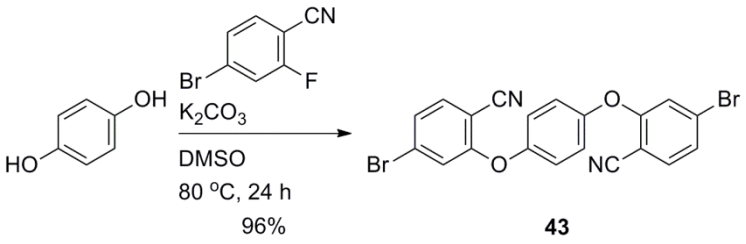

43

Hydroquinone (3.52 g, 32.0 mmol), 4-bromo-2-fluorobenzonitrile (14.1 g, 70.4 mmol), and K_2CO_3 (10.6 g, 76.8 mmol) were placed in a 100 mL two-necked round bottom flask with DMSO (30 mL). The mixture was degassed by an N_2-bubbling for 10 min and heated at 80 °C under stirring for 24 h. After cooling to rt, the reaction mixture was quenched by an addition of large amount of water. The resulting precipitate was collected by filtration, and the residue was washed with water and ethanol to obtain **43** (14.5 g, 96%) as a pale yellow powder.

43: $C_{20}H_{10}Br_2N_2O_2$; MW 470.11; mp 245–246 °C; ^{1}H NMR (400 MHz, $CDCl_3$, δ): 7.53 (d, J = 8.2 Hz, 2H), 7.32 (dd, J = 8.2 and 1.7 Hz, 2H), 7.19 (s, 4H), 7.05 (d, J = 1.7 Hz, 2H); ^{13}C NMR (100 MHz, $CDCl_3$, δ): 159.91, 151.64, 134.71, 128.81, 126.67, 122.12, 120.18, 115.14, 102.66; IR (KBr) ν_{max} (cm^{-1}): 3089, 3034, 2228, 1588, 1565, 1495, 1477, 1401, 1263, 1235, 1187, 1076, 1012, 904, 854, 819, 779, 590, 558, 504; MS (DART-TOF$^+$) m/z: 469.0, 471.0, and 473.0 [M + H$^+$]; Anal Calcd for $C_{20}H_{10}Br_2N_2O_2$: C, 51.10; H, 2.14; N, 5.96. Found: C, 50.94; H, 2.26; N, 5.66.

1,4-Bis(5-bromo-2-carboxyphenoxy)benzene (44)

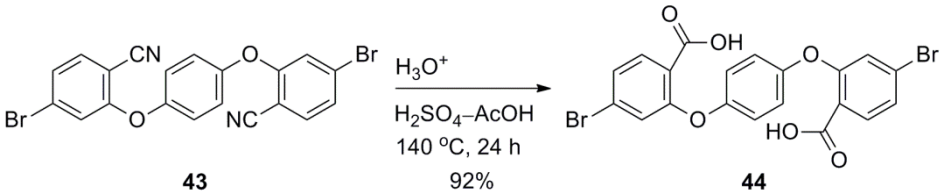

1,4-Bis-(5-bromo-2cyanophenoxy)benzene (**43**) (13.6 g, 29.0 mmol) was placed in a 300 mL round bottom flask with acetic acid (87 mL) and water (24 mL), and then concentrated H_2SO_4 (46 mL) was added. The mixture was heated at 140 °C for 24 h. After cooling to rt, the resulting mixture was added dropwise into ice-cooled water to quench the reaction. The generated precipitate was collected by filtration and rinsed with water and methanol to obtain **44** (13.6 g, 92%) as a white powder.

44: $C_{20}H_{12}Br_2O_6$; MW 505.90; mp > 300 °C; ^{1}H NMR (400 MHz, DMSO-d_6, δ): 13.13 (br, 2H), 7.77 (d, J = 8.3 Hz, 2H), 7.46 (dd, J = 8.3 and 1.8 Hz, 2H), 7.17 (d, J = 1.8 Hz, 2H), 7.04 (s, 4H); ^{13}C NMR (100 MHz, DMSO-d_6, δ): 165.77, 156.34, 152.34, 133.06, 126.67, 125.93, 123.08, 122.59, 120.06; IR (KBr) ν_{max} (cm^{-1}): 3383 (br), 2997 (br), 2661, 2574, 1698, 1590, 1566, 1497, 1476, 1441, 1415, 1390, 1299, 1225, 1188, 1146, 1095, 905, 849, 795, 770; MS (DART-TOF$^-$) m/z: 505.1, 507.1, and 509.1 [M – H$^-$]; Anal Calcd for $C_{20}H_{12}Br_2O_6$: C, 47.28; H, 2.38. Found: C, 47.27; H, 2.49.

3,10-Dibromo-13,14-dihydro-5,8-dioxapentaphene-13,14-dione (45)

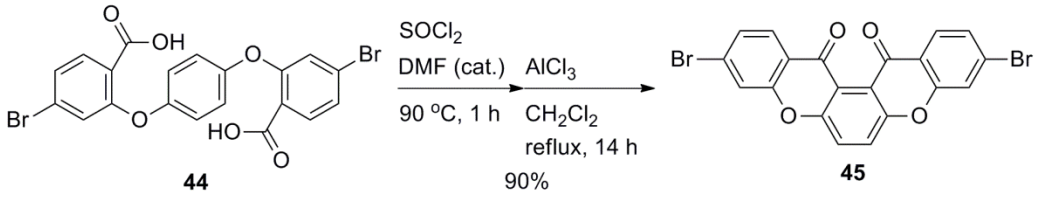

1,4-Bis(5-bromo-2-carboxyphenoxy)benzene (**44**) (3.56 g, 7.00 mmol) and one drop of DMF were placed in a 200 mL two-necked round bottom flask with thionyl chloride (30 mL). The suspension was refluxed at 90 °C for 1 h under an N_2 atmosphere. After cooling to rt, an excess amount of thionyl chloride was removed under reduced pressure to obtain the corresponding acid chloride as a pale-brown crude solid. This crude compound was used in the next step without further purification.

After refilling the reaction equipment with N_2, the obtained crude acid chloride was dissolved in dichloromethane (70 mL), and the mixture was cooled at 0 °C. To this solution was added finely-ground $AlCl_3$ (3.73 g, 28.0 mmol) by a portion. The resulting mixture was stirred at 0 °C for 1 h and then refluxed at 50 °C for additional 14 h. After cooling to rt, the mixture was poured in to an excess amount of 4 M aq HCl cooled at 0 °C. The resulting precipitate was collected by filtration, and the residue was washed with water and methanol. The crude solid was extracted with chloroform by Soxlet extraction method. After cooling to rt, the resulting precipitate was collected by filtration, and the residue was washed with methanol to obtain **45** (2.98 g, 90%) as a yellow powder.

45: $C_{20}H_8Br_2O_4$; MW 469.88; mp > 300 °C; ^{1}H NMR (400 MHz, $CDCl_3$, δ): 8.20 (d, J = 8.2 Hz, 2H), 7.81 (s, 2H), 7.71 (d, J = 1.8 Hz, 2H), 7.56 (dd, J = 8.2 and 1.8 Hz, 2H); ^{1}H NMR (400 MHz, CF_3COOD, δ): 8.63 (d, J = 8.8 Hz, 2H), 8.61 (s, 2H), 8.23 (d, J = 1.6 Hz, 2H), 8.02 (dd, J = 8.8 and 1.6 Hz, 2H); ^{13}C NMR (100 MHz, CF_3COOD, δ): 182.89, 159.84, 157.92, 138.99, 134.25, 133.69, 130.21, 123.27, 118.94, 117.86; IR (KBr) ν_{max} (cm^{-1}): 3089, 1683, 1658, 1604, 1586, 1448, 1417, 1330, 1311, 1249, 1204, 1156, 1065, 1025, 913, 857, 824, 809, 766, 684, 573; MS (DART-TOF$^+$) m/z: 470.9, 472.9, and 474.9 [M + H$^+$]; Anal Calcd for $C_{20}H_8Br_2O_4$: C, 50.88; H, 1.71. Found: C, 50.54; H, 1.81.

2,11-Dibromo-13,14-dimesityl-5,8-dioxapentaphene (14)

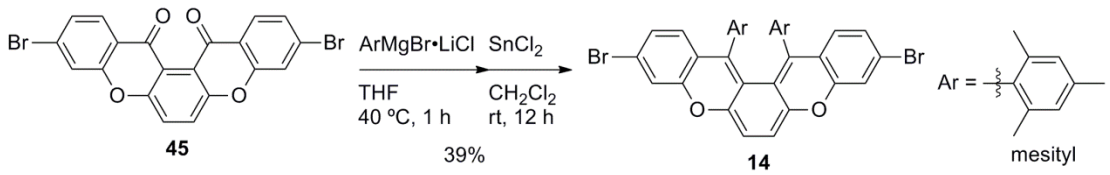

To prepare mesityl Grignard reagent, in a 30 mL two-necked round bottom flask under an N_2 atmosphere, the solution of 2-bromomesitylene (1.27 g, 6.40 mmol) in THF (4 mL) was added slowly to the suspension of anhydrous LiCl (237 mg, 5.60 mmol) and Mg turnings (134 mg, 5.60 mmol) in THF (4 mL) at 40 °C, and the mixture was stirred for 1 h.

In another 50 mL two-necked round bottom flask under an N_2 atmosphere, 3,10-dibromo-13,14-dihydro-5,8-dioxapentaphene-13,14-dione (**45**) (755 mg, 1.60 mmol) was placed with THF (16 mL) at 40 °C. To the suspension of **45** was added dropwise slowly the prepared mesityl Grignard reagent, and then the mixture was stirred for 1 h. After cooling to rt, 4 M aq HCl was added to quench the reaction. The aqueous layer was extracted with dichloromethane, and the combined organic layer was dried over Na_2SO_4. A removal of the solvent under reduced pressure gave the crude mesitylated diol.

The obtained crude diol was dissolved in dichloromethane (30 mL), and the mixture was degassed by an N_2-bubbling for 5 min. After the degassing, a drop of 4 M aq HCl and anhydrous $SnCl_2$ (1.82 g, 9.60 mmol) were added, and then the mixture was stirred at rt for 12 h. The resulting mixture was passed through Celite® to remove the excess amount of $SnCl_2$, and then the filtrate was concentrated under reduced pressure. The residue was passed through a short column on silica gel using *n*-hexane–dichloromethane (1:1 v/v) as eluent. After a removal of the solvent, the crude solid was washed with ethanol to obtain **14** (421 mg, 39%) as a purple solid. Single crystals of **14** suitable for X-ray analysis were obtained by a liquid diffusion of acetonitrile with a solution of **14** in CH_2Cl_2.

14: $C_{38}H_{30}Br_2O_2$; MW 678.45; mp 221–223 °C (decomp); ^{1}H NMR (400 MHz, $CDCl_3$, δ): 7.05 (d, J = 2.0 Hz, 2H), 6.83 (s, 2H), 6.72 (dd, J = 8.4 and 2.0 Hz, 2H), 6.61 (s, 2H), 5.97 (d, J = 2.0 Hz, 2H), 5.61 (s, 2H), 2.27 (s, 6H), 2.25 (s, 6H), 0.83 (s, 6H); ^{13}C NMR (100 MHz, $CDCl_3$, δ): 155.79, 145.37, 140.41, 137.70, 135.71, 135.69, 131.34, 129.37, 128.90, 128.18, 127.24, 124.78, 122.97, 122.70, 118.32, 102.38, 21.01, 20.36, 19.76; IR (KBr) ν_{max} (cm^{-1}): 2916, 1644, 1609, 1582, 1552, 1474, 1403, 1344, 1299, 1224, 1203, 1187, 1073, 1014, 916, 887, 849, 810, 712, 437; MS (DART-TOF$^+$) *m*/*z*: 677.1, 679.1, and 681.1 [M + H$^+$]; HRMS (ESI-TOF$^+$) *m*/*z*: Calcd. For $^{12}C_{38}{}^{1}H_{30}{}^{79}Br^{81}Br^{16}O_2$: 678.0592, Found: 678.0605 [M$^+$]; Anal Calcd for $C_{38}H_{30}Br_2O_2$: C, 67.27; H, 4.46. Found: C, 67.51; H, 4.62.

2,11-Dicyano-13,14-dimesityl-5,8-dioxapentaphene (13)

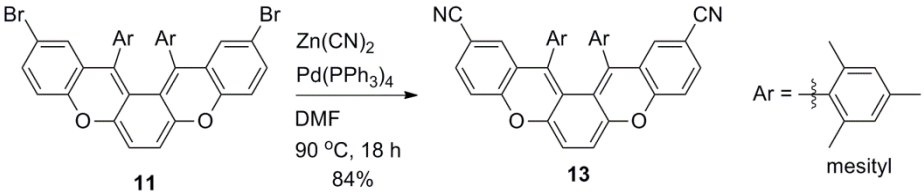

2,11-Dibromo-13,14-dimesityl-5,8-dioxapentaphene (**11**) (135 mg, 0.200 mmol), $Zn(CN)_2$ (70.4 mg, 0.600 mmol), and tetrakis(triphenylphosphine)palladium(0) (23 mg, 0.020 mmol) were placed in a sealed tube with *N*,*N*-dimethylformamide (4 mL), and then the mixture was degassed by an N_2-bubbling for 5 min. After degassing, the mixture was heated at 90°C for 18 h. After cooling to rt, saturated aq $NaHCO_3$ was added. The organic layer was extracted with dichloromethane, and then the extract was washed with water. The organic layer was combined and dried over anhydrous $MgSO_4$. After removal of the solvent under reduced pressure, the residue was purified by column chromatography on silica gel using *n*-hexane–dichloromethane (1:1 to 1:2 v/v) as an eluent to obtain **13** (96.8 mg, 84%) as a purple solid.

13: $C_{40}H_{30}N_2O_2$; MW 570.68; mp 290–295 °C (decomp); ^{1}H NMR (400 MHz, $CDCl_3$, δ): 7.34 (dd, J = 8.4 and 2.0 Hz, 2H), 6.93 (d, J = 8.4 Hz, 2H), 6.86 (s, 2H), 6.66 (s, 2H), 6.38 (d, J = 2.0 Hz, 2H), 5.69 (s, 2H), 2.30 (s, 6H), 2.25 (s, 6H), 0.82 (s, 6H); ^{13}C NMR (100 MHz, $CDCl_3$, δ): 158.49, 144.82, 139.97, 138.56, 135.63, 135.38, 133.42, 130.30, 130.19, 129.96, 129.24, 129.10, 124.77, 118.72, 116.32, 105.45, 103.36, 21.04, 20.35, 19.69; IR (KBr) ν_{max} (cm^{-1}): 2918, 2224, 1647, 1610, 1590, 1561, 1477, 1403, 1345, 1307, 0273, 1249, 1208, 1122, 1023, 822, 770, 727, 584, 420; MS (DART-TOF$^+$) *m*/*z*: 571.2 [M + H$^+$]; HRMS (DART-TOF$^+$) *m*/*z*: Calcd. For $^{12}C_{40}{}^{1}H_{31}{}^{14}N_2{}^{16}O_2$: 571.2386, Found: 571.2384 [M + H$^+$].

3,10-Dicyano-13,14-dimesityl-5,8-dioxapentaphene (15)

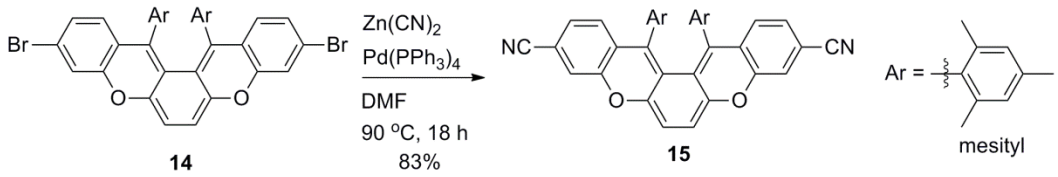

3,10-Dibromo-13,14-dimesityl-5,8-dioxapentaphene (**14**) (339 mg, 0.500 mmol), $Zn(CN)_2$ (176 mg, 1.50 mmol), and tetrakis(triphenylphosphine)palladium(0) (57.8 mg, 0.050 mmol) were placed in a sealed tube with *N*,*N*-dimethylformamide (10 mL), and then the mixture was degassed by an N_2-bubbling for 5 min. After degassing, the mixture was heated at 90°C for 18 h. After cooling to rt, saturated aq $NaHCO_3$ was added. The organic layer was extracted with dichloromethane, and then the extract was washed with water. The organic layer was combined and dried over anhydrous $MgSO_4$. After removal of the solvent under reduced pressure, the residue was purified by column chromatography on silica gel using *n*-hexane–dichloromethane (1:1 to 1:2 v/v) as an eluent to obtain **15** (236 mg, 83%) as a deep blue solid.

15: $C_{40}H_{30}N_2O_2$; MW 570.68; mp 249–251 °C (decomp); ^{1}H NMR (400 MHz, $CDCl_3$, δ): 7.12 (d, J = 1.6 Hz, 2H), 6.88 (dd, J = 8.2 and 1.6 Hz, 2H), 6.86 (s, 2H), 6.64 (s, 2H), 6.17 (d, J = 8.2 Hz, 2H), 5.71 (s, 2H), 2.28 (s, 6H), 2.25 (s, 6H), 0.82 (s, 6H); ^{13}C NMR (100 MHz, $CDCl_3$, δ): 155.35, 144.80, 140.24, 138.36, 136.13, 135.62, 130.70, 130.59, 129.58, 129.18, 127.89, 126.83, 125.50, 1118.37, 118.21, 112.32, 103.59, 21.03, 20.39, 19.77; IR (KBr) ν_{max} (cm^{-1}): 2918, 2227, 1648, 1609, 1547, 1446, 1408, 1379, 1345, 1311, 1247, 1213, 1016, 968, 849, 807, 750, 725, 618, 439; MS (DART-TOF$^+$) *m*/*z*: 571.2 [M + H$^+$]; HRMS (DART-TOF$^+$) *m*/*z*: Calcd. For $^{12}C_{38}{}^{1}H_{31}{}^{14}N_2{}^{16}O_2$: 571.2386, Found: 571.2386 [M + H$^+$].

6,7-Dibromo-3,10-dicyano-13,14-dimesityl-5,8-dioxapentaphene (46)

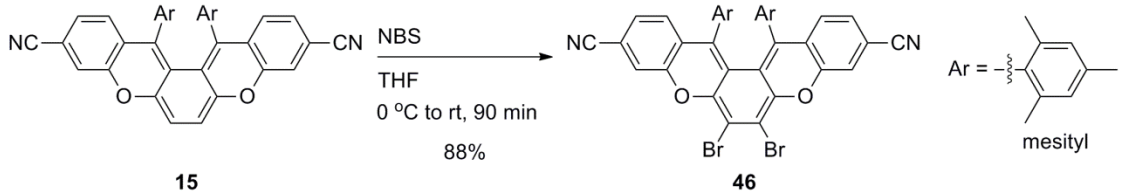

3,10-Dicyano-13,14-dimesityl-5,8-dioxapentaphene (**15**) (520 mg, 0.911 mmol) was placed in a 50 mL round bottom flask with THF (10 mL, without purification), and then the solution was cooled at 0 °C. To this solution was added dropwise a solution of *N*-bromosuccinimide (328 mg, 0.184 mmol) in THF (10 mL). After the addition, the mixture was allowed to warm up to rt, and stirred for 90 min. To quench the reaction, saturated aq $NaHCO_3$ was added. The aqueous layer was extracted with dichloromethane, and the combined organic layer was dried over anhydrous $MgSO_4$. After removal of the solvent under reduced pressure, the residue was purified by column chromatography on silica gel using *n*-hexane–dichloromethane (1:2 v/v) as eluent to obtain **46** (581 mg, 88%) as a bluish purple solid.

46: $C_{40}H_{28}Br_2N_2O_2$; MW 728.47; mp 260–265 °C (decomp); ^{1}H NMR (400 MHz, $CDCl_3$, δ): 7.33 (d, J = 1.8 Hz, 2H), 6.96 (dd, J = 8.2, 1.8 Hz, 2H), 6.86 (s, 2H), 6.65(s, 2H), 6.25 (d, J = 8.2 Hz, 2H), 2.28 (s, 6H), 2.23 (s, 6H), 0.79 (s, 6H); ^{13}C NMR (100 MHz, $CDCl_3$, δ): 154.45, 142.27, 140.09, 138.86, 136.89, 135.52, 129.76, 129.74, 129.27, 128.15, 127.53, 127.21, 126.19, 118.99, 117.82, 113.08, 99.54, 21.02, 20.53, 19.90; IR (KBr) ν_{max} (cm^{-1}): 2915, 2228, 1624, 1610, 1583, 1546, 1408, 1378, 1309, 1244, 1118, 972, 920, 870, 849, 829, 799, 617, 473, 420; MS (ESI-TOF$^+$) m/z: 726.1, 728.1, and 730.1 [M^+]; Anal Calcd for $C_{40}H_{28}Br_2N_2O_2$: C, 65.95; H, 3.87; N, 3.85. Found: C, 65.85; H, 3.95; N, 3.90.

2',3',6',7'-Tetramethylphenanthreno[9',10'-*d*]-3,10-dicyano-13,14-dimesityl-5,8-dioxapentaphene (16)

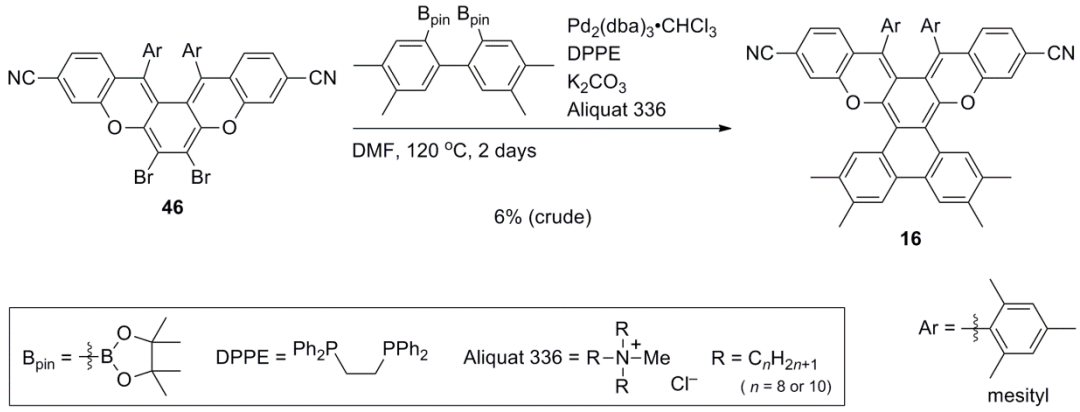

6,7-Dibromo-3,10-dicyano-13,14-dimesityl-5,8-dioxapentaphene (**46**) (72.8 mg, 0.100 mmol), 2,2'-bis(4,4,5,5-tetramethyl-1,3,2-dioxaborolane-2-yl)-4,4',5,5'-tetramethylbiphenyl (45.4 mg, 0.0950 mmol), tris(dibenzylideneacetone)dipalladium(0) chloroform adduct (10.4 mg, 0.010 mmol), 1,2-bis(diphenylphosphino)ethane (8.00 mg, 0.020 mmol), K_2CO_3 (124 mg, 0.900 mmol), and one drop of Aliquat® 336 were placed in a sealed tube with *N*,*N*-dimethylformamide (5 mL), and then the mixture was degassed by an N_2-bubbling for 5 min. After degassing, the mixture was heated at 120 °C for 2 days. After cooling to rt, water was added. The organic layer was extracted with dichloromethane, and then the extract was washed with water. The organic layer was combined and dried over anhydrous $MgSO_4$. After removal of the solvent under reduced pressure, the residue was purified by column chromatography on silica gel using *n*-hexane–toluene (1:2 v/v) as an eluent to obtain crude **16** (crude 5 mg, 6%) as a bluish-green solid.

16: $C_{56}H_{44}N_2O_2$; MW 776.96; ^{1}H NMR (400 MHz, $CDCl_3$, δ): 8.37 (s, 2H), 7.75 (s, 2H), 7.25 (d, J = 1.6 Hz, 2H), 6.91 (dd, J = 8.2 and 1.6 Hz, 2H), 6.88 (s, 2H), 6.67 (s, 2H), 6.26 (d, J = 8.2 Hz, 2H), 2.42 (s, 6H), 2.29 (s, 6H), 2.31 (s, 6H), 2.30 (s, 6H), 0.83 (s, 6H); MS (ESI-TOF$^+$) m/z : 776.3 [M^+]; HRMS (ESI-TOF$^+$) m/z: Calcd. For $^{12}C_{56}{}^1H_{44}{}^{14}N_2{}^{16}O_2$: 776.3403, Found: 776.3403 [M^+].

2,11-Dibromo-13,14-bis(4-*tert*-butyl-2,6-dimethylphenyl)-5,8-dioxapentaphene (17)

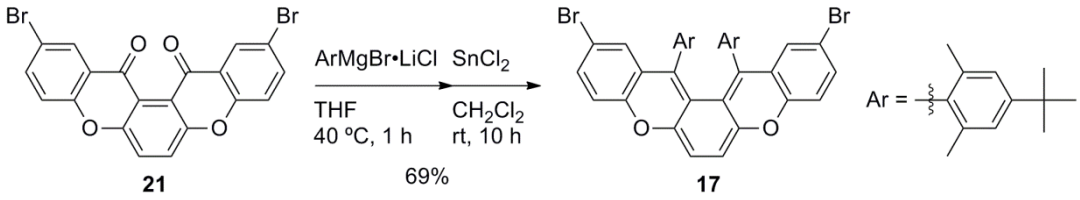

To prepare the Grignard reagent, in a 10 mL two-necked round bottom flask under an N_2 atmosphere, the solution of 4-*tert*-butyl-2,6-dimethylphenyl bromide (386 mg, 1.60 mmol) in THF (1 mL) was added slowly to the suspension of anhydrous LiCl (59.4 mg, 1.40 mmol) and Mg turnings (33.6 mg, 1.40 mmol) in THF (1 mL) at 40 °C, and the mixture was stirred for 1 h.

In another 30 mL two-necked round bottom flask under an N_2 atmosphere, 2,11-dibromo-13,14-dihydro-5,8-dioxapentaphene-13,14-dione (**21**) (189 mg, 0.400 mmol) was placed with THF (4 mL) at 40 °C. To the suspension of **21** was added dropwise slowly the prepared Grignard reagent, and then the mixture was stirred for 1 h. After cooling to rt, 4 M aq HCl was added to quench the reaction. The aqueous layer was extracted with dichloromethane, and the combined organic layer was dried over Na_2SO_4. A removal of the solvent under reduced pressure gave the crude arylated diol.

The obtained crude diol was dissolved in dichloromethane (8 mL), and the mixture was degassed by an N_2-bubbling for 5 min. After the degassing, a drop of 4 M aq HCl and anhydrous $SnCl_2$ (455 mg, 2.40 mmol) were added, and then the mixture was stirred at rt for 10 h. The resulting mixture was passed through Celite® to remove the excess amount of $SnCl_2$, and then the filtrate was concentrated under reduced pressure. The residue was passed through a short column on silica gel using dichloromethane as eluent. After a removal of the solvent, the crude solid was washed with ethanol to obtain **17** (210 mg, 69%) as a bluish-purple solid. Single crystals of **17** suitable for X-ray analysis were obtained by a liquid diffusion of acetonitrile with a solution of **17** in CH_2Cl_2.

17: $C_{44}H_{42}Br_2O_2$; MW 762.61; mp 286–288 °C (decomp); ^{1}H NMR (400 MHz, $CDCl_3$, δ): 7.16 (dd, J = 8.6 and 2.3 Hz, 2H), 7.02 (d, J =1.8 Hz, 2H), 6.80 (d, J = 1.8 Hz, 2H), 6.77 (d, J = 8.6 Hz, 2H), 6.19 (d, J = 2.3 Hz, 2H), 5.63 (s, 2H), 2.30 (s, 6H), 1.33 (s, 18H), 0.87 (s, 6H); ^{13}C NMR (100 MHz, $CDCl_3$, δ): 154.52, 15078, 145.26, 139.74, 135.73, 135.13, 132.05, 130.91, 128.73, 128.67, 125.82, 125.69, 125.29, 116.77, 114.20, 102.35, 34.34, 31.33, 20.77, 20.55; IR (KBr) ν_{max} (cm^{-1}): 2965, 2911, 2867, 1641, 1605, 1588, 1469, 1393, 11337, 1284, 1262, 1235, 1303, 1078, 1018, 869, 815, 719, 550, 420; MS (DART-TOF$^+$) m/z: 761.3, 763.3, and 765.3 [M + H$^+$]; HRMS (ESI-TOF$^+$) m/z: Calcd. For $^{12}C_{44}{}^{1}H_{42}{}^{79}Br^{81}Br^{16}O_2$: 762.1531, Found: 762.1534 [M$^+$]; Anal Calcd for $C_{44}H_{42}Br_2O_2$: C, 69.30; H, 5.55. Found: C, 68.96; H, 5.60.

2,11-Dibromo-13,14-bis(4-trimethylsilyl-2,6-dimethylphenyl)-5,8-dioxapentaphene (18)

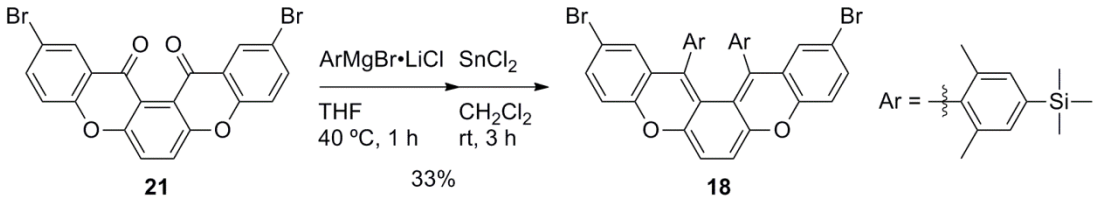

To prepare the Grignard reagent, in a 10 mL two-necked round bottom flask under an N_2 atmosphere, the solution of 4-trimethylsilyl-2,6-dimethylphenyl bromide (206 mg, 0.800 mmol) in THF (0.5 mL) was added slowly to the suspension of anhydrous LiCl (29.7 mg, 0.700 mmol) and Mg turnings (16.8 mg, 0.700 mmol) in THF (0.5 mL) at 40 °C, and the mixture was stirred for 1 h.

In another 10 mL two-necked round bottom flask under an N_2 atmosphere, 2,11-dibromo-13,14-dihydro-5,8-dioxapentaphene-13,14-dione (**21**) (94.4 mg, 0.200 mmol) was placed with THF (2 mL) at 40 °C. To the suspension of **21** was added dropwise slowly the prepared Grignard reagent, and then the mixture was stirred for 1 h. After cooling to rt, 4 M aq HCl was added to quench the reaction. The aqueous layer was extracted with dichloromethane, and the combined organic layer was dried over Na_2SO_4. A removal of the solvent under reduced pressure gave the crude arylated diol.

The obtained crude diol was dissolved in dichloromethane (4 mL), and the mixture was degassed by an N_2-bubbling for 5 min. After the degassing, a drop of 4 M aq HCl and anhydrous $SnCl_2$ (228 mg, 1.2 mmol) were added, and then the mixture was stirred at rt for 3 h. The resulting mixture was passed through Celite® to remove the excess amount of $SnCl_2$, and then the filtrate was concentrated under reduced pressure. The residue was passed through a short column on silica gel using *n*-hexane–dichloromethane (1:1 v/v) as eluent. After a removal of the solvent, the crude solid was recrystallized from dichloromethane–acetonitrile to obtain **18** (53.2 mg, 33%) as a bluish-purple solid. Single crystals of **18** suitable for X-ray analysis were obtained by a liquid diffusion of acetonitrile with a solution of **18** in CH_2Cl_2.

18: $C_{42}H_{42}Br_2O_2Si_2$; MW 794.76; mp 213–215 °C (decomp); ^{1}H NMR (400 MHz, $CDCl_3$, δ): 7.16 (dd, J = 8.7 and 2.3 Hz, 2H), 7.14 (s, 2H), 6.89 (s, 2H), 6.78 (d, J = 8.7 Hz, 2H), 6.19 (d, J = 2.3 Hz, 2H), 5.64 (s, 2H), 2.30 (s, 6H), 0.85 (s, 6H), 0.28 (s, 18H); ^{13}C NMR (100 MHz, $CDCl_3$, δ): 154.53, 145.12, 140.46, 139.29, 135.62, 134.68, 134.23, 133.82, 133.27, 132.22, 128.58, 125.45, 116.84, 114.27, 102.60, 20.50, 20.42, –1.12; IR (KBr) ν_{max} (cm^{-1}): 2954, 1645, 1588, 1469, 1441, 1394, 1338, 1285, 1261, 1248, 1233, 1018, 897, 862, 834, 752, 740, 717, 630, 547; MS (DART-TOF$^+$) *m*/*z*: 793.2, 795.2, and 797.2 [M + H$^+$]; HRMS (ESI-TOF$^+$) *m*/*z*: Calcd. For $^{12}C_{42}{}^{1}H_{42}{}^{79}Br^{81}Br^{16}O_2{}^{28}Si_2$: 794.1070, Found: 794.1081 [M$^+$]; Anal Calcd for $C_{42}H_{42}Br_2O_2Si_2$: C, 63.47; H, 5.33. Found: C, 63.58; H, 5.38.

4-13. References

(1) (a) Nakai, Y.; Mori, T.; Inoue, Y. *J. Phys. Chem. A* **2012**, *116*, 7372−7385.
(b) Sánchez-Carnerero, E. M.; Agarrabeitia, A. R.; Moreno, F.; Maroto, B. L.; Muller, G.; Ortiz, M. J.; de la Moya, S. *Chem. - Eur. J.* **2015**, *21*, 13488−13500.

(2) (a) Shen, Y.; Chen, C. -F. *Chem. Rev.* **2012**, *112*, 1463−1535.
(b) Gingras, M. *Chem. Soc. Rev.* **2013**, *42*, 1051−1095.

(3) Kiran, V.; Mathew, S. P.; Cohen, S. R.; Delgado, I. H.; Lacour, J.; Naaman1, R. *Adv. Mater.* **2016**, *28*, 1957−1962.

(4) (a) Sandströ m, J. *Dynamic NMR Spectroscopy*; Academic Press: London, 1982.
(b) Bakhmutov, V. I. *NMR Spectroscopy in Liquids and Solids*; CRC press: Boca Raton, 2015.

(5) (a) Gingras, M.; Félix, G.; Peresutti, R. *Chem. Soc. Rev.* **2013**, *42*, 1007−1050.
(b) Rickhaus, M.; Mayor, M.; Juríček. M. *Chem. Soc. Rev.* **2016**, *45*, 1542−1556.

List of publications

1. “2,11-Dibromo-13,14-dimesityl-5,8-dioxapentaphene: A Stable and Twisted Polycyclic System Containing the *o*-Quinodimethane Skeleton”
   Org. Lett. **2016**, *18*, 1052–1055.
   Sato, C.; Suzuki, S.; Kozaki, M.; Okada, K.

Supplementary publications

1. “Synthesis, Properties, and n-Type Transistor Characteristics of π-Conjugated Compounds Having Carbonyl-bridged Thiazole-fused Polycyclic System”
   Chem. - Eur. J. **2014**, *20*, 16509–16515.
   Ie, Y.; Sato, C.; Nitani, M.; Tada, H.; Aso, Y.

2. “Solution-processable n-Type Semiconducting Materials Containing a Carbonyl-bridged Thiazole-fused π System”
   Chem. Lett. **2014**, *43*, 1640–1642.
   Ie, Y.; Sato, C.; Nitani, M.; Tada, H.; Aso, Y.

Acknowledgement

I would like to express my gratitude to Professor Dr. Keiji Okada for his various hearty leading and encouragement throughout the course of this work. I gratefully acknowledge to Professor Dr. Masatoshi Kozaki for his valuable advice and suggestions based on his deep and wide knowledge. I express my special thanks to Dr. Shuichi Suzuki (Lecturer at Osaka City University until Sept. 2015, Associate Professor at Osaka University from Oct. 2015) for his helpful advice and suggestions.

I am deeply grateful to Professor Dr. Yoshio Aso (Osaka University), Associate Professor Dr. Yutaka Ie (Osaka University), Assistant Professor Dr. Masashi Nitani (Osaka University), and Dr. Makoto Karakawa (Assistant Professor at Osaka University until Apr. 2016, Associate Professor at Kanazawa University from May 2016) for their various leading, advice, and suggestions throughout my master's degree program, which founded an important research background of this work.

I thank all members of the Analytical Center in Osaka City University for NMR measurements, MS measurements, elemental analyses, and single crystal X-ray analyses and also all member of the Laboratory for Physical Organic Chemistry for their helpful discussions and kind friendships. I would like to thank all researchers who gave valuable lectures, knowledge, discussions, suggestions, and encouragement for me in my research life.

I also acknowledge the financial support by the Sasakawa Scientific Research Grant (No. 27–313) from The Japan Science Society.

January 2017

Chihiro Sato